

ALMA MATER STUDIORUM · UNIVERSITÀ DI BOLOGNA

---

SCUOLA DI SCIENZE  
Dipartimento di Fisica e Astronomia  
Corso di Laurea in Astrofisica e Cosmologia

# Variability of quasars at the dawn of Universe

Relatore:  
Chiar.ma Prof.ssa  
Marcella Brusa

Presentata da:  
Denise Trupia

Correlatore:  
Chiar.mo Dott.  
Roberto Decarli

---

Sessione III  
Anno Accademico 2019/20



*Remember to look up at the stars and not down at your feet. Try to make sense of what you see and wonder about what makes the universe exist. Be curious. And however difficult life may seem, there is always something you can do and succeed at. It matters that you don't just give up.*

*Stephen Hawking*

*As you know, madness is like gravity...all it takes is a little push.*

*Joker*



# Contents

<b>1</b>	<b>Active Galactic Nuclei</b>	<b>1</b>
1.1	Introducing AGN . . . . .	1
1.2	Classification of AGN . . . . .	3
1.3	The AGN paradigm . . . . .	4
1.4	AGN broad-band emission . . . . .	6
1.4.1	Radio emission . . . . .	6
1.4.2	Infrared emission . . . . .	6
1.4.3	Optical/Ultraviolet emission . . . . .	8
1.4.4	X-ray emission . . . . .	8
1.4.5	$\gamma$ -ray emission . . . . .	9
1.5	AGN luminosity . . . . .	9
1.6	AGN flux variability . . . . .	11
1.7	Dependence of flux variability on AGN properties . . . . .	13
1.8	High redshift AGN . . . . .	16
1.9	How Supermassive Black Holes form . . . . .	16
1.10	Early SMBH growth . . . . .	18
1.11	The quasar population at $z > 5.5$ . . . . .	20
1.12	AGN evolution . . . . .	24
<b>2</b>	<b>Variability of high redshift quasars</b>	<b>29</b>
2.1	The sample of this study . . . . .	29
2.2	Photometric information from wide area surveys . . . . .	29
2.2.1	Sloan Digital Sky Survey . . . . .	30
2.2.2	Panoramic Survey Telescope and Rapid Response System . . . . .	31
2.2.3	The Dark Energy Camera Legacy Survey . . . . .	33
<b>3</b>	<b>The photometric follow-up from Loiano</b>	<b>37</b>
3.1	Cassini Telescope . . . . .	37
3.2	Our observational campaign . . . . .	39

---

3.3	Data reduction . . . . .	40
3.4	Data analysis . . . . .	44
3.5	Results . . . . .	46
4	Discussion and conclusions	55
A	Scientific images	59
B	Zero point	65
	Bibliography	65

# List of Figures

1.1	A schematic diagram of the AGN unified model . . . . .	4
1.2	A schematic representation of an AGN spectral energy distribution (SED)	7
1.3	Examples of light curve in the UV and optical band of F9 over 14 years, NGC 4151 over 17 years and NGC 5548 over 8 months . . . . .	12
1.4	Dependence of flux variability on time interval, redshift, and luminosity .	14
1.5	Scheme of the three described scenarios for SMBH seed . . . . .	17
1.6	Masses of the black hole seeds required to obtain the observed black hole masses in a quasar sample . . . . .	19
1.7	Growth of a SMBH mass under different assumption for the accretion rate and efficiency. . . . .	20
1.8	Distribution of quasar bolometric luminosities vs SMBH masses estimated from Mg II emission . . . . .	21
1.9	Photometry and combined NIR spectrum of the quasar J1342+0928 at $z$ $= 7.54$ . . . . .	22
1.10	Compilation of optical spectra of known $z > 5.7$ quasars with Lyman break at different redshift . . . . .	23
1.11	The $z$ -J versus $i$ - $z$ color-color diagram for quasar candidate selection. . .	24
1.12	The evolution of quasar comoving spatial density at $M_{1450} < -26.8$ . . .	25
1.13	Infographic with the sequence of evolution of a typical galaxy passing through AGN phase . . . . .	27
2.1	SDSS filters response in ugriz band . . . . .	31
2.2	An image of SDSS telescope . . . . .	31
2.3	The PS1 capture cross-section in $\text{m}^2/\text{e}/\text{photon}$ to produce a detected $e^-$ for an incident photon for the six Pan-STARRS1 bandpasses, grizy and w for a standard airmass of 1.2 . . . . .	32
2.4	A photography of PanSTARRS1 telescope . . . . .	33
2.5	Comparison between PS1 filters griz and SDSS filters ugriz and other survey filters . . . . .	34
2.6	DES DR1 Standard Bandpasses for the DECam g, r, i, z and Y filters . .	34

2.7	A photography of DECaLS telescopes . . . . .	35
3.1	Gunn filters of Loiano Telescope . . . . .	38
3.2	A photography of Loiano telescope taken on 23 February 2020 . . . . .	38
3.3	Data reduction process: master bias, master flat, original frame, bias subtracted image . . . . .	42
3.4	Data reduction process: division by sky flat, sky subtraction, aligning and final output . . . . .	43
3.5	Astrometry calibration: Astrometry.net output and Lukas Wenzl's code output . . . . .	44
3.6	Light curves in the observer's frame of variable sources: J0836+0054, J1016+2541, J1335-0328, J2310+1855 . . . . .	49
3.7	Light curves in the observer's frame of non variable sources: P108+08, J1148+5251, J0100+2802, J0439+1634, J0818+1722, J044-0125 . . . . .	50
3.8	Light curves in the observer's frame of variable sources in PS1 but not in SDSS: P071-02, J1137+3549, P323+12 . . . . .	51
3.9	Histogram showing the number of variable sources in function of variability amplitude . . . . .	53
4.1	Dependence of flux variability from BH mass, redshift, luminosity and rest frame interval, extended with data from Chan et., 2020 . . . . .	57
A.1	Images of the sample quasars: J1335-0328, J2310+1855 . . . . .	59
A.2	Images of the sample quasars: J0100+2802, J0439+1634 . . . . .	60
A.3	Images of the sample quasar: J0818+1722, P108+08 . . . . .	61
A.4	Images of the sample quasars: J1148+5251, J1044-0125, J1137+3549 . . . . .	62
A.5	Images of the sample quasars: P071-02, P323+12, J0836+0054, J1016+2541 . . . . .	63
B.1	Zero points of the sample quasars: J1335-0328, J2310+1855 . . . . .	65
B.2	Zero points of the sample quasar: J0100+2802, J0439+1634, J0818+1722, P108+08 . . . . .	66
B.3	Zero points of the sample quasars: J1148+5251, J1044-0125, P071-02, J1137+3549, P323+12, J0836+0054, J1016+2541 . . . . .	67

# List of Tables

2.1	PS1, SDSS and DECaLS filters, their central wavelenght and FWHM . . .	35
3.1	The sample of present study and their proprieties . . . . .	40
3.2	Final result: variability amplitude, significance and time intervals. . . . .	47
3.3	DECaLS variability amplitude and significance . . . . .	48
3.4	(1) Target. (2), (3) and (4) Magnitude-to-time interval ratio in unity of mag/year for PS1 (P), SDSS (S) and DECaLS (D) . . . . .	52



## Abstract

Supermassive black holes (SMBH) with masses of  $\approx 10^6 - 10^9 M_\odot$  are ubiquitous at the center of most galaxies. If accretion events occur, the material falling into the SMBH heats up and becomes very luminous: these objects are called active galactic nuclei (AGN). Because of their high luminosity, AGN could be studied also at high distances. A major puzzle of modern astrophysics comes from the mere presence of fully matured supermassive black holes of  $\approx 10^8 - 10^9 M_\odot$  at high redshift ( $z > 6 - 7$ ). This fact implies that some of these objects were already in place when the Universe was less than 1 Gyr old. How were they formed and what kind of mechanism has acted on their growth in a such short time?

According to state-of-the-art theoretical models, in the early Universe the most massive dark matter halos had suitable physical conditions to hosts the seeds of these objects. Different scenarios have been proposed to explain the formation of the BH seeds: a light seed in which SMBH are remnants of popIII stars ( $M_{BH} \approx$  few hundred of  $M_\odot$ ); an intermediate seed due to stellar dynamical instabilities with  $\approx 10^3 M_\odot$ ; an heavy seed from a direct black hole collapse of  $\approx 10^6 M_\odot$ . To grow the accretion of gas must have proceed almost continuously close to the Eddington limit. Breaking the equilibrium condition between the gravity force and the radiation pressure, a more pronounced variability could be expected in the accretion of the highest redshift quasars, thus in their luminosity.

Most of the quasars currently known at  $z \approx 6$  have been discovered thanks to large scale and deep surveys, such as the Sloan Digital Sky Suvey (SDSS), the Panoramic Survey Telescope and Rapid Response System (Pan-STARRS), the Canada-France High- $z$  Quasar Survey (CFHZQS), the United Kingdom Infrared Deep Sky Survey (UKIDSS) Large Area Survey (ULAS), the Dark Energy Camera Legacy Survey (DECaLS) and the VISTA Survey (ATLAS and VIKING). Nowadays, after 20 years from the first surveys, we are able to search for any indication of variability also for high redshift quasars.

In this thesis work, using the 152cm Cassini Telescope of Loiano, I observed a small sample of luminous quasars with magnitude of  $\approx 18 - 20$  in the  $z$  band at redshift from  $z > 5.5$ . Only with the  $z$  band we are able to observe these objects in the optical band, considering that their spectrum is completely shifted in the NIR part of the electromagnetic spectrum. After data reduction and analysis, I obtained the magnitude of the observed sources in order to compare them with SDSS, Pan-STARRS and DECaLS results. The analysis revealed a diversity in the variability properties of high-redshift quasars: some objects do not show evidence of variability, while for others it seems to be a consistent trend in the increasing or decreasing of the observed flux in comparison with SDSS16, Pan-STARRS and DECaLS data.

I buchi neri supermassicci (SMBH) con masse di  $10^6 - 10^9 M_\odot$  sono onnipresenti al centro della maggior parte delle galassie. Se si verificano eventi di accrescimento, il materiale che cade nell'SMBH si riscalda e diventa molto luminoso: questi oggetti sono chiamati nuclei galattici attivi (AGN). A causa della loro elevata luminosità, gli AGN possono essere studiati anche se molto distanti.

Un grande enigma dell'astrofisica moderna deriva dalla presenza di buchi neri supermassicci completamente formati di  $\approx 10^8 - 10^9 M_\odot$  ad altissimo redshift ( $z > 6 - 7$ ). Questo fatto implica che alcuni di questi oggetti erano simili a quelli che osserviamo al giorno d'oggi quando l'Universo aveva meno di 1 miliardo di anni. Come si sono formati e che tipo di meccanismo ha agito sulla loro crescita in così poco tempo?

Secondo i modelli teorici più avanzati, nell'Universo primordiale gli aloni di materia oscura più massicci avevano condizioni fisiche adeguate per ospitare i "semi" di questi oggetti. Sono stati proposti diversi scenari per spiegare la formazione di questi semi: uno leggero in cui SMBH sono resti di stelle di popolazione III ( $M_{BH} \approx$  poche centinaia di  $M_\odot$ ); un seme intermedio dovuto a instabilità dinamiche stellari con  $\approx 10^3 M_\odot$ ; un seme pesante da un collasso diretto di un buco nero di  $\approx 10^6 M_\odot$ . Per aumentare la sua massa, l'accrescimento di gas deve aver proceduto quasi continuamente vicino al limite di Eddington. Rompendo la condizione di equilibrio tra la forza di gravità e la pressione di radiazione, ci si potrebbe aspettare una variabilità più pronunciata nell'accrescimento dei quasar con il redshift più alto, quindi nella loro luminosità.

La maggior parte dei quasar attualmente noti a  $z \approx 6$  sono stati scoperti grazie a survey profonde e su larga scala, come la Sloan Digital Sky Survey (SDSS), la Panoramic Survey Telescope Rapid Response System (Pan-STARRS), la Canada-Francia High- $z$  Quasar Survey (CFHZQS), la United Kingdom Infrared Deep Sky Survey (UKIDSS) Large Area Survey (ULAS), la Dark Energy Camera Legacy Survey (DECaLS) e la VISTA Survey (ATLAS e VIKING). Ad oggi, a distanza di 20 anni dalle prime rilevazioni, siamo in grado di ricercare qualsiasi indicazione di variabilità anche per quasar ad alto redshift.

In questo lavoro di tesi, utilizzando il Telescopio Cassini da 152 cm di Loiano, ho osservato un piccolo campione di quasar luminosi con magnitudine  $\approx 18 - 20$  nella banda  $z$  a redshift  $z > 5.5$ . Solo attraverso la banda  $z$  siamo in grado di osservare questi oggetti nella banda ottica, considerando che il loro spettro è completamente spostato nella parte del vicino infrarosso dello spettro elettromagnetico. Dopo la riduzione e l'analisi dei dati, ho ottenuto la magnitudine delle sorgenti osservate per confrontarle con i risultati di SDSS, Pan-STARRS e DECaLS. Come risultato, ho riscontrato una diversità nel comportamento di queste sorgenti: alcuni oggetti non mostrano evidenza di variabilità, mentre per altri sembra esserci un andamento consistente nell'aumento o diminuzione del flusso osservato rispetto alle osservazioni SDSS16, Pan-STARRS e DECaLS.

# Chapter 1

## Active Galactic Nuclei

### 1.1 Introducing AGN

Active Galactic Nuclei (AGN) are galaxies in which the energetic emission is so powerful that it could not be from stellar processes, but from the accretion onto compact a source, called supermassive black hole (SMBH) (e.g. Rees 1984). It is widely accepted that SMBHs are located at the center of every galaxy (Magorrian et al., 1998; Kormendy, 2004). AGN are about the 1%-10% of galaxies in the whole Universe (Ho, 2008), they have high luminosities ( $L \approx 10^{40} - 10^{48}$  erg/s) and large masses ( $M \approx 10^6 - 10^9 M_{\odot}$ ). AGN become visible when they accrete gas directly from their surroundings, then the gravitational potential energy of the infalling mass is converted to radiation, making the black hole luminous. The most powerful among them are known as quasars.

The quasar phase constitute a relatively short stage of galaxy evolution (Salpeter, 1964; Lynden-Bell, 1969; Rees, 1978) that last for  $10^7 - 10^8$  years (Martini & Weinberg, 2001; Kelly et al., 2010), after which the accretion rate drops dramatically and the active nucleus transitions to a low-luminosity AGN or quiescent galaxy state (Churazov et al., 2005).

The first astronomer who observed six spiral galaxies with the presence of broad and strong emission lines in their nuclei was Seyfert, in 1943. His work remained largely ignored until Baade & Minkowski (1954) pointed out the similarities between the spectra of the galaxies studied by Seyfert and that of the galaxy they had associated with the Cygnus A radio source.

Then, in 1959, Woltjer suggested that an high stellar density in that nuclei could be the source of this emission and they had to have high masses. Hazard et al. (1963) was able to identify an accurate position of the strong radio source 3C 273 using the method of lunar occultations. This measurement allowed Schmidt (1963) to identify an optical counterpart to 3C 273: a 13th magnitude star that had a peculiar spectrum with very

broad emission lines. Schmidt realized that the Hydrogen Balmer emission lines in the spectrum of this *radio-star* are the same known lines of other spectra but redshifted ( $z = 0.16$ ). Because of their star-like appearance in visible light, astronomer referred to them as *quasi-stellar radio object*, quasar.

In 1965, Alan Sandage found that several other point-sources had similar characteristics to these quasars but without the radio emission at  $z \approx 2$ . Sandage called these objects quasi-stellar galaxies. However it was rapidly found that most quasars do not emit in radio or are weak radio emitters.

After their discoveries, a huge amount of AGN were found; in particular, identifying quasar at high redshift allowed astronomers to study objects at distances further and further away.

A well known characteristic of quasars is their strong flux variability across a broad range of wavelengths, timescales, and accretion states (Mushotzky et al., 1993; Ulrich et al., 1997; Peterson, 2001). The variability in the optical continuum of quasars has been recognized since their first optical identification in 1963 by Matthews and Sandage.

In the early 2000s, the rise of optical large scale imaging surveys has been exploited for investigate on variability phenomena for several purposes such as to estimate Eddington ratios and black hole masses (Bauer et al., 2009; Wilhite et al., 2008), or simply to identify them (Geha et al., 2003).

Reverberation mapping (RM) studies (Peterson et al. 2005) show that the broad emission lines respond to continuum fluctuations, therefore providing strong evidence that the variability is intrinsic to the quasars.

RM uses the time delays between the variability of emission from different regions within the AGN. In details, optical continuum variations are followed by emission lines from the broad-line region (BLR), but with a delay corresponding to the time it employed by the light to travel to the BLR from the continuum-emitting region. This information provides a characteristic radius of the BLR gas, which can be combined with an orbital velocity estimate from the width of the broad emission lines allow a virial estimate of mass, that most fundamental of all black hole parameters. RM is used to estimate the BH mass:

$$M_{BH} = \frac{R_{BLR}v_{BLR}^2}{G} \quad (1.1)$$

Where  $R_{BLR}$  is the characteristic radius of the broad line emission,  $v_{BLR}$  is the velocity of the emitting clouds at  $R_{BLR}$  and can be estimated from the width of the emission line:

$$v_{BLR} = f \cdot FWHM \quad (1.2)$$

and  $f$  is a geometrical factor.

In this sense, variability is one of the most powerful tools available to explore the physical processes in these objects and to determine the physics of the central engine, the nuclear environment, the properties of the material along the line of sight, and, ultimately, their

role in the evolution of galaxies (Kelly et al., 2009; Kozłowski et al., 2010; MacLeod et al., 2010; Schmidt et al., 2010; Butler & Bloom, 2011; Kim et al., 2011; MacLeod et al., 2011; Ruan et al., 2012; Andrae et al., 2013; Zu et al., 2013).

## 1.2 Classification of AGN

Different classifications of AGN exist, based on various historical properties related to the first discovery of vary class at one determined wavelength. But, the most used ones are based on proprieties of the optical spectrum or of their radio emission (Padovani et al., 2017). Looking at the optical spectrum there are *type 1* or *unobscured*, AGN that present broad emission lines ( $\approx 10^4$  km/s) in their optical spectra, and *type 2* or *obscured* AGN, that do not show broad lines.

Depending on the radio-loudness parameter (Kellermann, 1989), an optical-to-radio ratio, we call *Radio Quiet* the galaxies in which  $R = \frac{F(5GHz)}{F(4400A)} < 10$  and *Radio Loud* with  $R > 10$ . Radio Loud are the 1-10 % of AGN and present a relativistic jet (Falcke et al., 1996).

Among the *Radio Loud AGN* there are:

- **Radiogalaxies:** giant elliptical galaxies that represent the most numerous population. In the radio band they could be divided in two types: *Fanaroff-Riley I* (FRI), jet dominated with  $P_{1.4GHz} < 10^{24}$  W/Hz and *FRII*, lobe dominated with  $P_{1.4GHz} > 10^{24}$  W/Hz;
- **Radio Loud Quasars:** Quasi-stellar Radio Source, because the optical counterpart appears like a point source, as a star. They are the most luminous with  $M_B < -23$ ;
- **Blazars:** they are seen close to the jet and have a flat optical spectrum. They are highly variable and could be divided in *BL Lac* and *Optical Violent Variable* (OVV).

Among the *Radio Quiet AGN* there are:

- **Seyfert Galaxies:** low luminosity spiral galaxies with  $M_B > -23$ ;
- **Radio quiet quasar:** like other quasars but without a strong radio emission. For each radio-loud quasar there are about 10 radio quiet, but the term quasar has remained associated with the whole class, regardless of radio emission.;
- **Low Ionization Nuclear Emission line Region galaxies (LINERs):** with a weak continuum spectrum and narrow and low ionization emission lines.

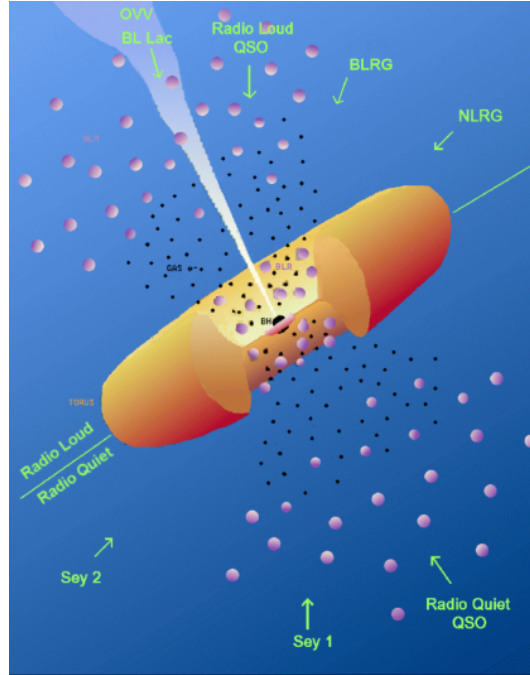


Figure 1.1: A schematic diagram of the current paradigm for AGN, showing all the component described in section 1.3 and the nomenclature from 1.2 . Adapted from Urry & Padovani, 1995

### 1.3 The AGN paradigm

The diversity of properties that resulted in the complex classification scheme described before can be mostly ascribed to a single picture, the AGN unification model. This is based on the assumption that they are the same object but seen with different orientation (Antonucci, 1993; Urry & Padovani, 1995; Netzer, 2015), with different accretion rate (Heckman & Best, 2014), with the presence or absence of strong jets (Padovani, 2016), and also with different stage of their evolution (Hopkins et al., 2008).

According to this model, the most accredited structure of AGN consists of: a central supermassive black hole (SMBH), an accretion disk, a hot corona, a broad-line region, an obscuring torus, a narrow-line region and, in some cases, a relativistic jet. An graphic representation can be seen in fig.1.1.

**Black hole** ( $10^{-7} - 10^{-3}$  pc) - is the fundamental element at the center of all AGN, it is characterized by mass ( $M$ ) and spin ( $a$ ). The event horizon of a black hole, in which gravity can be strong enough that even light cannot escape, has a characteristics radius,

the gravitational radius:

$$R_g = \frac{GM}{c^2} \quad (1.3)$$

Where  $c = 3 \cdot 10^{10}$  cm/s is the light speed and  $G = 6.67 \cdot 10^8$  cm<sup>3</sup>/g/s<sup>2</sup> is the universal gravitational constant. The event horizon directly depends on the spin of the BH:

$$a = \frac{J}{GM^2} \quad (1.4)$$

Where  $J$  is the angular momentum. Its radius, in units of  $R_g$ , is equal to  $R_{\pm} = 1 \pm (1 - a^2)^{1/2}$ . For a non-rotating BH ( $a = 0$ ) is equal to the Schwarzschild radius,  $R_s = 2R_g$ . For a maximally rotating BH ( $a^2 = 1$ ), it corresponds to the gravitational radius.

**Accretion disk** ( $10^{-7} - 1$  pc) - is composed by high temperature gas that orbits around the SMBH, forming a rotating accretion disk. One of the first and most utilized disk models is the Shakura & Sunyaev (Shakura et al., 1973), with a geometrically thin and optically thick disk and high accretion efficiency. The disk temperature decreases with the distance from the SMBH, reaching a maximum of  $T \approx 10^5 - 10^6$  K. The viscosity and the differential rotation of the layer of the disk slow the gas in the inner orbit, allowing it to fall into the SMBH. Another popular model is the Advection Dominated Accretion Flow (ADAF) (Ichimaru, 1977), characterized by a geometrically thick but optically thin disk and a low accretion efficiency.

**Hot corona** ( $10^{-3}$ pc) - is formed by high ionized gas at  $T \approx 10^8 - 10^9$  K. It is optically thin and its geometry and distribution are yet unknown (Chartas et al., 2016, 2017).

**Broad Line Region** ( $10^{-3} - 10^{-4}$  pc) - is a cloudy distribution of gas, responsible for the broad-line emission. The high velocities ( $10^3 - 10^4$  km/s) reached in the BH vicinity cause the line broadening via the Doppler effect. These clouds have temperatures around  $T \approx 10^4$  K and densities  $n \approx 10^{10} - 10^{11}$  cm<sup>-3</sup>, high enough to suppress several forbidden lines.

**Torus** ( $1 - 10$  pc) - is composed by gas and dust, it is optically thick and has low temperature  $T \approx 10^3$  K. There are different models to describe its structure: a smooth distribution (Pier & Krolic, 1992), in which the temperature depends from the distance from the radiative field, or a clumpy distribution where clouds have different temperatures and densities and the obscuration comes from their superposition to the line of sight (Jaffe et al., 2004; Burtscher et al., 2013).

**Narrow Line Region** ( $10 - 100$  pc) - are clouds less dense than BLR ( $n \approx 10^3 - 10^4$  cm<sup>-3</sup>). At these densities, forbidden line emission is no longer suppressed. Because of

the larger distance from the central black hole, the gas clouds in the narrow line region have typical velocities of  $> 10^3$  km/s and so the emission line profiles are narrow. These regions are also external to the torus, hence NLR can not be obscured by it.

**Jets** ( $10^{-3} - 10^7$  pc) - consisting of a plasma of relativistic particles accelerated by the magnetic field in the innermost regions of the AGN, and ejected in polar directions up to Mpc scales, where they can interact with the external medium (Blandford et al., 2018). In some AGN the jet-medium interactions produces large radio-lobes and hot spots, that are regions where the jets collide and interact with the external medium, producing shocks and strong synchrotron emission. Some of the gas is driven out into jets, focused by magnetic fields. They dominate the emission from the  $\gamma$ -rays to the radio band. The physical nature of AGN jets remain uncertain.

## 1.4 AGN broad-band emission

AGN emission cover the full electromagnetic spectrum over more than twenty orders of magnitude in frequency: from radio band to high energies (Padovani, 2017). A schematic representation of an AGN Spectral Energy Distribution (SED) is showed in Fig.1.2.

### 1.4.1 Radio emission

At low frequencies, in the **radio band**, the non-thermal emission dominates with the synchrotron mechanism (Risaliti & Elvis, 2004). Ultra relativistic electrons, with a mass of  $m_e$  and a Lorentz factor  $\gamma$  are accelerated by a magnetic field  $B$  and they emits a photon of frequency:

$$\nu = BE^2 \quad (1.5)$$

where  $E = \gamma m_e c^2$ . The entire population of electrons have a power law energy distribution:

$$N(E)dE \propto E^{-\delta}dE \quad (1.6)$$

It generate a power law spectrum:

$$F_\nu \propto \nu^{-\alpha} \quad (1.7)$$

Where  $\alpha = (\delta - 1)/2$  is the spectral index.

### 1.4.2 Infrared emission

In the **infrared** there is thermal emission coming from the dusty torus surrounding the central region: UV and optical photons are absorbed by dust of the torus and re-emitted in the mid-IR band. Also, the host galaxy emits in this band because of star formation

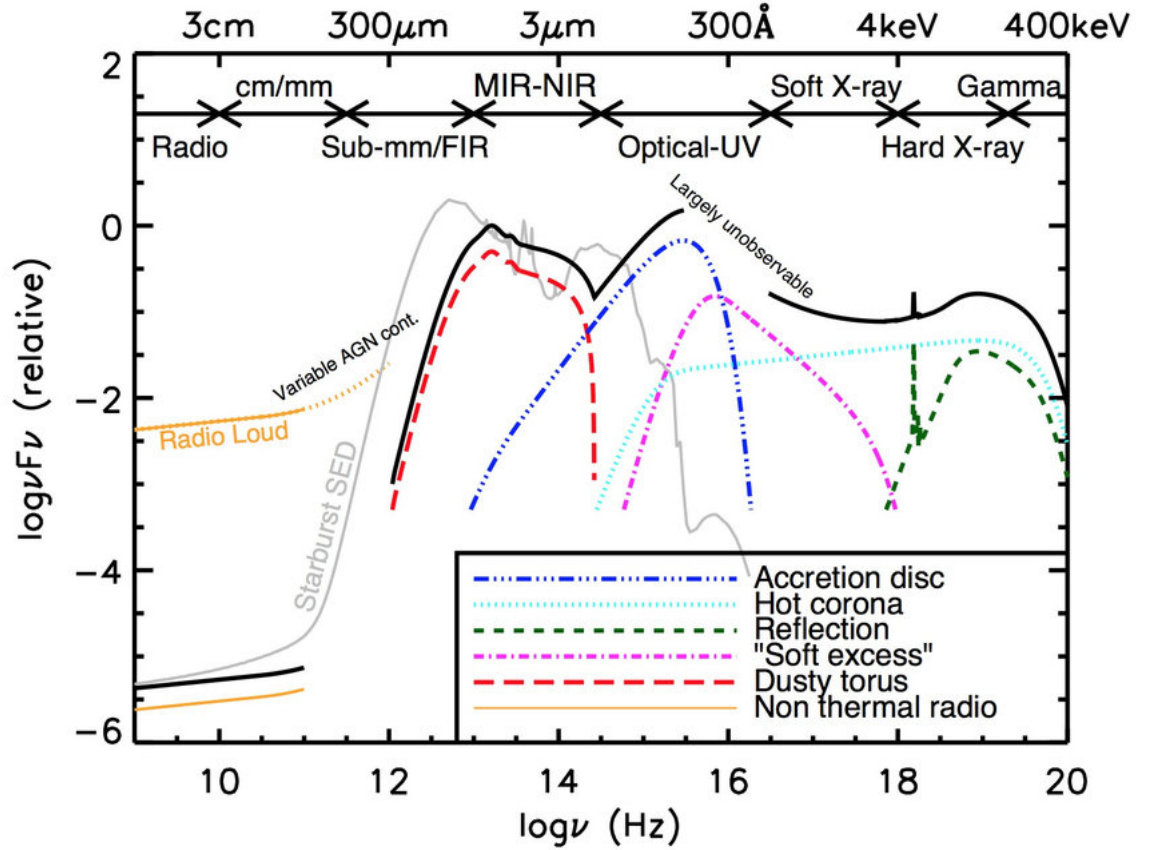


Figure 1.2: A schematic representation of an AGN spectral energy distribution (SED), loosely based on the observed SEDs of non-jetted quasars (e.g. Elvis et al., 1994; Richards et al., 2006a). The black solid curve represents the total SED and the various coloured curves (with an arbitrary offset) represent the individual components. The SED of an AGN in the millimeter/FIR (Far Infrared) regime is uncertain; however, it is widely believed to have a minimal contribution (to an overall galaxy SED) compared to star formation, except in the most intrinsically luminous quasars and powerful radio-loud AGN. The primary emission from the AGN's accretion disk peaks in the UV region. Radio-loud AGN have radio emission that can be several orders of magnitude higher than radio-quiet ones (shown with the labelled orange line). Also shown is an example radio-UV SED of a starburst galaxy (grey curve; the SED is of M82 taken from the GRASIL library; (Silva et al., 1998). From Harrison, 2014.

processes and O-B stars emission. There is a peak, the *IR bump* at  $\lambda \approx 10 - 20\mu m$  corresponding to temperatures about 50-1000 K due to the reprocessing of photons by the disk.

### 1.4.3 Optical/Ultraviolet emission

In the **optical/UV band** there is the *Big Blue Bump*, an energy excess corresponding to a superposition of different black bodies between  $300 - 3000\text{\AA}$  (multi-color black body). It is a thermal emission from the accretion disk that creates a power law emission with  $F_\nu \propto \nu^{1/3}$ .

### 1.4.4 X-ray emission

The primary power law emission in the **X-ray band** is due to the Inverse Compton Process. This emission comes from the inner region of the AGN. This mechanism is generated from ultra relativistic electrons from the *Hot Corona* with temperature  $T \approx 10^9 K$  that interact with seed photons from the accretion disk: electrons lost part of their energy and photons are up-scattered several time until they reach energy of about hundreds of keV.

The resulting spectrum is a power law obtained from several black body spectra modified by different scattering processes.

$$F_E \propto E^{-\Gamma} \quad (1.8)$$

In which  $\Gamma$ , the photon index is:

$$\Gamma = \alpha + 1 \quad (1.9)$$

And  $\alpha$  is the spectral index

$$\alpha = \frac{-\ln\tau}{-\ln A} \quad (1.10)$$

$\tau$  is the opacity and  $A$  is the mean energy obtained by photons in each scattering:

$$A = e^{\frac{4kT}{m_e c^2} \tau} \quad (1.11)$$

The exponent term is called *Comptonization parameter*.

At about 100-300 keV there is an exponential cut-off in the spectrum: this process is not efficient anymore, because electrons with a certain temperature can give anymore to photons an energy bigger than their transported energy. Under the energy of 1 keV there is a *soft excess* probably from thermal emission from the inner regions of disk. In addition, Compton scattering causes a reflection of the primary power law on the optically thick disk or the dusty torus towards the observer, generating another component called *Compton Reflection Hump*. Under 20 keV there is the photoelectrical effect and absorption lines.

### 1.4.5 $\gamma$ -ray emission

For the  $\gamma$ -ray band, the emission is still debated as two alternative (or complementary) interpretations are being considered. In leptonic models (e.g. Maraschi, Ghisellini Celotti, 1992) the emission is explained as inverse Compton scattering between the electrons in the jet and their own synchrotron emission (synchrotron self-Compton) or an external photon field (external inverse Compton). In hadronic scenarios (e.g. Böttcher et al., 2013)  $\gamma$ -rays are instead assumed to originate from high-energy protons either losing energy through synchrotron emission (Aharonian, 2000) or through photo-meson interactions. In this case blazars would also be neutrino emitters (from the decay of charged pions) extending their SEDs outside the electromagnetic spectrum into newly explored multi-messenger scenarios, which might even include cosmic rays.

## 1.5 AGN luminosity

The central supermassive black hole is a compact object that emits extreme luminosities. This mechanism can be explained only through radiatively efficient accretion of matter from a disk that is falling on the SMBH because of gravitational attraction and it heats up due to dynamical friction. Converting potential energy into thermal and radiation, it can be obtained that:

$$L = \epsilon \frac{dM}{dt} c^2 = \epsilon \dot{M} c^2 \quad (1.12)$$

Where  $\epsilon$  is the mass-to-energy conversion efficiency. Inverting the formula and knowing the source luminosity, the accretion rate can be found:

$$\dot{M} = \frac{L}{\epsilon c^2} \approx 1.8 \cdot 10^{-3} \frac{L_{44}}{\epsilon} \quad (1.13)$$

In which  $L_{44}$  is the luminosity in unity of  $10^{44}$  erg/s. Considering the potential gravitational energy of a particle of mass  $m$  and at the distance  $r$  from the SMBH with a mass  $M$ , as:

$$U = \frac{GMm}{r} \quad (1.14)$$

The rate of energy converted in radiation is:

$$L \approx \frac{dU}{dt} = \frac{GM\dot{M}}{r} \quad (1.15)$$

To estimate the efficiency  $\epsilon$ , from equation 1.5, considering the case of a particle of mass  $m$ :

$$U = 0.1mc^2 \quad (1.16)$$

The two canonical values for  $R$  correspond to the Schwarzschild black hole, which has  $\epsilon \approx 0.06$ , and the Kerr black hole, which has  $\epsilon = 0.42$ . Given our lack of knowledge about the physical parameters of the supermassive black holes that power quasars, the general practice is to adopt a value that lies between these two extremes, that is,  $\epsilon \approx 0.1$  (among the most efficient processes in the Universe).

The **Eddington luminosity** is the maximum luminosity admitted for which the radiative pressure exerted by the photons emitted in the accretion process is smaller than the gravitational binding energy of the accreting material. It is defined as the hydrostatic equilibrium condition between radiative pressure and gravity. Overtaking this value means that the pressure is so high that blows away the gas, suppressing the accretion process. Assuming a spherical accretion (Bondi accretion) of ionized hydrogen, the radiative force is:

$$F_{rad} = \frac{L\sigma_T}{4\pi R^2 c} \quad (1.17)$$

$\sigma_T = 6.65 \cdot 10^{-25} \text{cm}^2$  is the Thomson cross section, because the radiation pressure acts on electrons through the Thomson scattering. The gravitational force that acts on the protons is:

$$F_{grav} = \frac{G(m_p + m_e)M}{R^2} \approx \frac{Gm_p M}{R^2} \quad (1.18)$$

because  $m_p \gg m_e$  where  $m_p = 1.67 \cdot 10^{24} \text{g}$  is the proton mass. Equalling these forces, one can obtain the Eddington Luminosity:

$$L_{Edd} = \frac{4\pi G c m_p M}{\sigma_T} = 1.26 \cdot 10^{38} \frac{M}{M_\odot} \quad (1.19)$$

The accretion rate can be also expressed as:

$$\dot{M}_{Edd} = \frac{L_{Edd}}{\epsilon c^2} = \frac{2.2 M_8}{\frac{\epsilon}{0.1}} \quad (1.20)$$

In which  $M_8$  is the mass in the mass unity of  $10^8 M_\odot$ .

Another important definition is the *Eddington ratio*, that is the ratio between the bolometric luminosity and the Eddington luminosity:

$$\lambda = \frac{L_{bol}}{L_{Edd}} \quad (1.21)$$

The Eddington ratio is commonly considered a proxy of how rapidly the black hole is growing.

During particular stages of their activity, AGN can emit at Super-Eddington regime ( $L > L_{Edd}$ ), although for short period of time (Pezzulli et al., 2017). This happens

because one or more of the assumptions are wrong or temporarily violated, particularly the spherical geometry.

Changes in the accretion flow are also the source of the bulk of observed variability in AGN.

## 1.6 AGN flux variability

A key feature of active galactic nuclei consists in their stochastic, non-periodic continuum variability (see light curves in fig.1.3).

Large luminosity variations on timescale from years to hours, from the optical to the X-rays, are common (York et al., 2000; Chambers et al., 2016; Flaugher, 2005; de Vries et al., 2003; Vanden Berk et al., 2004).

The most studied sample of quasars is the SDSS *Stripe 82* (S82): the catalog covers the equatorial sky region defined by  $22 \text{ hr } 24 \text{ minutes} < \text{R.A.} < 4 \text{ hr } 8 \text{ minutes}$  and  $-1.27^\circ < \text{decl.} < 1.27^\circ$  (an area of 290 squared degrees), contains 34 million photometric observations in the SDSS ugriz system for 748084 unresolved sources at high Galactic latitudes that was imaged multiple times (up to 60) by the Sloan Digital Sky Survey from 2000 to 2008 (Ivezic et al., 2007).

The mechanisms which drive AGN variability are still not completely understood. It is a common thought that different components of AGN contribute to flux variations in different electromagnetic bands.

In the recent years several scenarios to explain this phenomena have been proposed:

- a superposition of flares/spots due to accretion disk instabilities (Trèvese & Vagnetti, 2002; Pereyra et al., 2006);
- gravitational microlensing by compact foreground objects (Zackrisson et al., 2003).
- tidal disruption event and subsequent digestion of a star (Merloni et al., 2015; Trakhtenbrot et al., 2019; Ricci et al., 2020);
- multiple supernovae explosions (e.g., Terlevich et al., 1992).

Observational evidences (Vanden Berk et al., 2004) seem to disadvantage gravitational microlensing and generic stochastic processes as the primary source of quasar variability, in favor of accretion disk instability models. It is also possible that a combination of sources produce variations in quasar light curves, and none of the models can be excluded at all. Numerous analysis use standard accretion disk models to demonstrate that the optical/UV variability of quasars could be driven by a variable accretion rate (Pereyra et al., 2006; Li & Cao, 2008; Liu et al., 2008), while Blackburne & Kochanek (2010) have found evidence in the light curves of microlensed quasars that the optical variability is

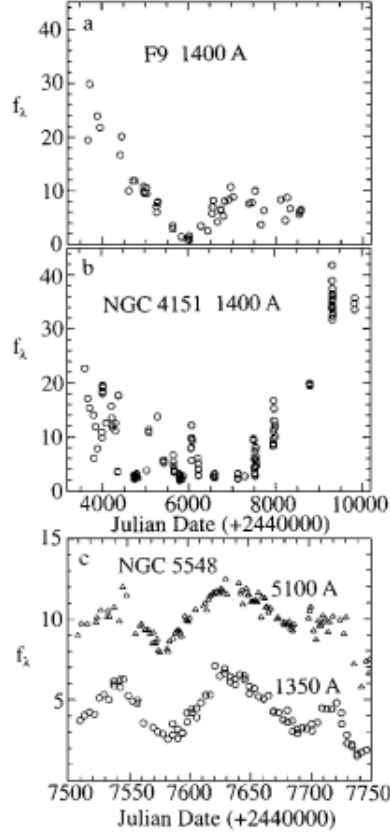


Figure 1.3: Examples of light curve from Ulrich et al., 1997. Long- and short-term continuum variations in three low-luminosity AGN: (a) UV light curve of F9 over 14 years (Recondo-González et al., 1997). (b) UV light curve of NGC 4151 over 17 years. The passage through the deep minimum was interrupted by short excursions to medium bright level. The vertical groups of points, unresolved on this scale, are IUE campaigns with an adequate sampling interval of typically three days. (c) Optical and UV light curves of NGC 5548 over 8 months (December 1988–July 1989; Clavel et al., 1991; Peterson et al., 1994) ordinates in  $10^{-14} \text{ergs}^{-1} \text{cm}^{-2} \text{Å}^{-1}$ .

caused by a change in the effective area of the accretion disk. The typical variations of  $\approx 10 - 20\%$  level in flux on timescales of years are originated from the standard thin disk model (Vanden Berk et al., 2004a; MacLeod et al., 2010, 2012; Schmidt et al., 2010; Simm et al., 2016), while the short-term variability (hours to days) is determined by other mechanisms, for example: the X-ray reprocessing (Krolik et al., 1991), local temperature fluctuation in disk (Dexter & Agol, 2011; Cai et al., 2016) and corona-heated

accretion-disk reprocessing (Sun et al., 2020).

Reprocessing of variable X-ray photons in the UV/optical emitting regions of the disk explains why, on timescales of hours-to-days, AGN are more variable in the X-rays than in the UV/optical (Markowitz & Edelson, 2004; Shemmer et al., 2014). On the other hand, the availability of long X-ray observations and simultaneous optical monitoring allows the extension of these studies to longer timescales, revealing that on month-to-year timescales variations in the optical are more intense than in the X-rays (Arévalo et al., 2008, 2009; Breedt et al., 2009, 2010; Uttley et al., 2003).

Variability studies are fundamental, since they probe the structure of the accretion disk and constrains the physical mechanisms of accretion processes, where the emitting region is too compact to be spatially resolvable.

In the last two decades, a new approach to the analysis of AGN variability has recently become available via multi-epoch observations in wide-area surveys (Pan-STARRS, Catalina Real-time Transient Survey, Zwicky Transient Facility). In fact, they provide a statistically consistent amount of data related to the repeated monitoring of several objects, which are necessary to perform a meaningful individual variability analysis only for low redshift sources. This kind of work has never been done before on quasars at  $z > 5.5$  because of are very faint, rare and the time dilution due to redshift makes timescales longer to trace variability, thus more time is needed in order to highlight significant changes. It was not possible to extend at this redshift variability studies until nowadays, after 20 years from their first detection (corresponding to a couple of years in the rest-frame system). The first case of variability in a quasar at very high redshift, J1030+0524, was discovered in the X-ray band in Nanni et al., 2018. Repeating, for the first time, photometrical observations in the optical/UV band of such high redshift quasars from surveys dataset, providing a long-duration study of these object in order to find any indication of variability, is the main aim of this thesis.

## 1.7 Dependence of flux variability on AGN properties

A deeper knowledge about mechanism acting in AGN and responsible for AGN variability can be achieved by studying the relation between the amplitude of the variability with AGN properties (e.g. luminosity, BH mass, time lag) and their evolution with redshift. Figure 1.4 shows the results from the work of Vanden Berk et al. (2004) that studied the amplitude of variability in a sample of  $\approx 25000$  QSO from Stripe 82, selected from 0.5 up to  $z \approx 4.5$ , and reported them as a function of rest frame time delay, redshift and absolute magnitude.

According to several studies, variability appears to be anti-correlated with **luminosity**:

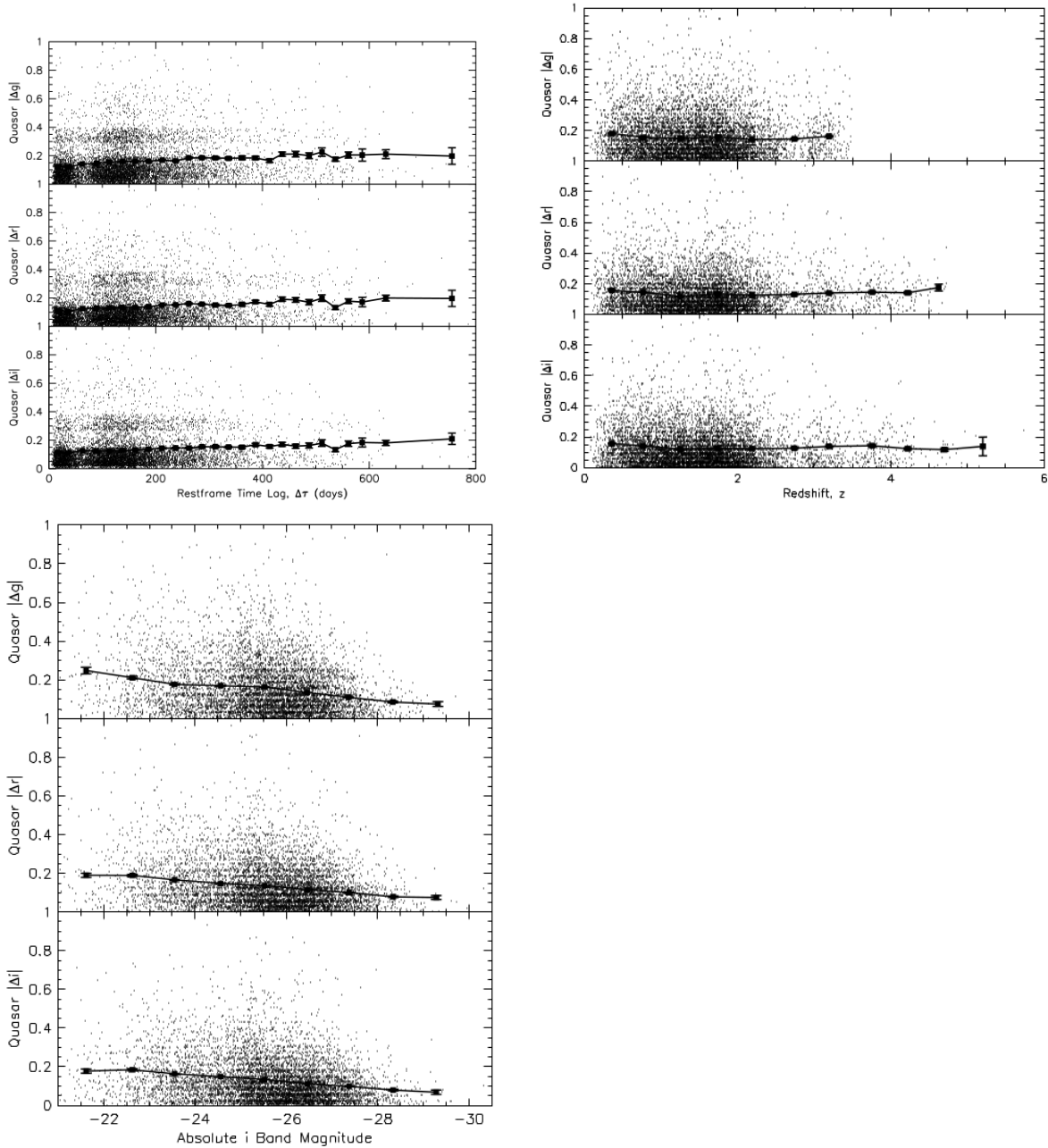


Figure 1.4: From Vanden Berk et al., 2004. Dependence of flux variability on time interval (top left panel), redshift (top right), and luminosity (bottom left panel). The binned points show the mean values, while the error bars show the rms deviations divided by the square root of the number of objects in a bin.

more luminous quasars are less variable (Vanden Berk et al., 2004). In fact, higher luminosity quasars tend to be more massive and larger. So whatever physical process drives variability, the expectation is that brighter quasars to vary more slowly (Morganson et al., 2014). This evidence is confirmed in the optical as well as in the X-ray band (e.g. Lawrence & Papadakis, 1993; Netzer et al., 1996; Manners et al., 2002; Zuo et al., 2012; Paolillo et al., 2017).

AGN variability also appears to depend on **black hole mass**, with more massive black holes showing a more pronounced variability (Wold et al., 2007; Wilhite et al., 2008; MacLeod et al., 2010), suggesting that more massive black holes vary on longer timescales. This led to the suggestion that the amplitude of variability may be driven by the Eddington ratio ( $\lambda$ ), implying differences in accretion rate. Another concept from Wold et al. (2007) to explain why the variability amplitude is correlated with black hole mass is that more massive black holes are starving and have a large flux variability because they do not have a steady inflow of gaseous fuel. Nevertheless, Simm et al. (2016) did not observe any correlation with the black hole mass and other works report an anti-correlation with  $M_{BH}$  (Kelly et al., 2009, 2013). It was proposed by Li et al., 2018 that the greater black hole mass is, the less the quasar is influenced by perturbation, no matter what causes the variability.

The variability amplitude is correlated with the **timescale of variability**  $\Delta T$ , which may indicate that the AGN variability is caused by stochastic processes, like thermal fluctuations of the accretion disk (Hawkins, 2002; de Vries, Becker & White, 2003; Kelly et al., 2009; Dexter & Agol, 2011; Kimura et al., 2020).

The dependence on **redshift** is still source of controversial results. Some authors (Li et al., 2018) recover a positive correlation, while others find a negative correlation (Cristiani et al., 1990, 1996). In some other works, variability is not correlated with  $z$  at all (Cimatti, Zamorani, & Marano, 1993; Paltani & Courvoisier, 1994; Netzer et al., 1996; Cristiani, Trentini, La Franca, & Andreani 1997; Helfand et al., 2001; Macleod et al., 2010). The increase of variability with redshift is consistent with the idea that galaxies were generally more active and dynamic in the early universe (Morganson et al., 2014), for Vanden Berk et al., (2004) quasars appear to be more variable at higher redshifts. If the effect is intrinsic, the quasar population or the variability mechanism is changing over time. External causes are also possible, such as gravitational microlensing which may increase with redshift since more potential lenses would be available (Vanden Berk et al., 2004).

The different results regarding the dependence on redshift suggest selection effects, it is probable that at different redshifts quasars of different luminosity are observed, therefore depending on how the sample is selected, different results can be found.

A consensus on the observational trends with variability is emerging, but disagreements remain, and even the most fundamental relationships need better characterization (Collier & Peterson, 2001; Kelly et al., 2009; MacLeod et al., 2012).

## 1.8 High redshift AGN

In this thesis work, the definition of high redshift quasar means  $z > 5.5$ , when the Universe was less than a billion years old. The first high redshift quasar, J1044-0125 at  $z = 5.80$ , was discovered by Fan et al. (2000b). These quasars are among the most luminous quasars at any redshift: they are likely powered by supermassive black holes with masses several billion solar masses, and reside in dark matter halos of  $10^{13} - 10^{14} M_{\odot}$  (Fan, 2006). At present, this epoch of the primordial universe represents the observational limit beyond which modern instruments struggle to reach.

Look at high redshift SMBHs, it could be noted that they have similar properties than lower ones: similar SED (Barnett et al., 2015), similar spectrum (Mortlock et al., 2011), similar metallicity (Banados et al., 2017). Also X-ray spectral properties of high-redshift QSOs do not differ significantly from those of AGN at lower redshift (Nanni et al., 2017). The fact that these early quasars appear as mature and evolved as the quasars observed billions of years later is an unsolved puzzle, and a challenge to our understanding of the formation and early growth of SMBHs and their host galaxies.

How can be explained that only 1 Gyr after the Big Bang, completely formed SMBHs could be seen?

## 1.9 How Supermassive Black Holes form

According to the standard cosmological model, dark matter perturbations grow in time, to the point that they separate from the expansion of the Universe, collapse, virialize and form self-gravitating halos. Inside these halos proto-galaxies and SMBH set up. There are three main theories about SMBH seeds (see also fig.1.5):

- light seed ( $100-600 M_{\odot}$ ): remnants of population III stars (Madau & Rees 2001; Volonteri & Rees 2006);
- heavy seed ( $10^4 - 10^6 M_{\odot}$ ): direct collapse of gas clouds (Volonteri et al., 2008; Agarwal et al., 2014; Valiante et al., 2016);
- intermediate seed ( $10^3 M_{\odot}$ ): stellar mergers in dense cluster (Volonteri & Rees 2006; Madau et al., 2014; Volonteri et al., 2016; Pezzulli et al., 2017).

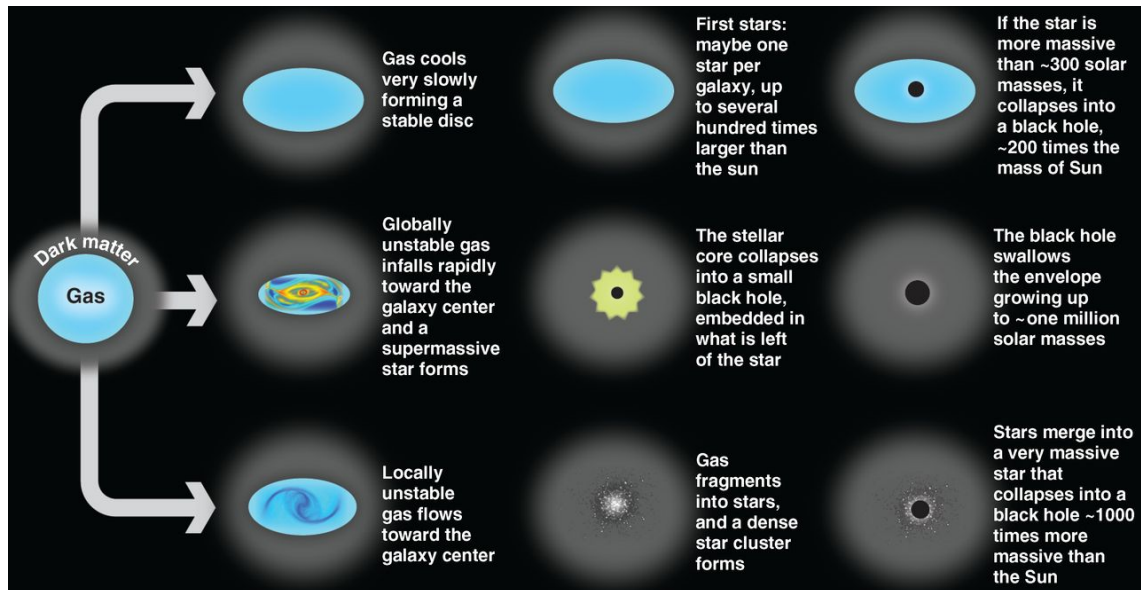


Figure 1.5: Scheme of the three described scenarios from Volonteri, 2012. The starting point is a primeval galaxy, composed of a dark matter halo and a central condensation of gas. Most of this gas will eventually form stars and contribute to making galaxies as we know them. However, part of this gas has also gone into making a MBH, probably following one of these routes. Light seed is the upper scenario, the heavy seed stays in the middle, at the bottom there is the intermediate seed.

**Population III** stars are the first generation of stars, poor of heavy elements, but they have not been observed yet. They are more massive than popI and popII stars, they can reach a few hundred of solar masses and they have to evolve faster. After recombination, a small amount of hydrogen combines in  $H_2$  molecules. In absence of any primordial soft UV background,  $H_2$  is not photodissociated and acts as an effective coolant in  $\approx 10^6 M_\odot$  halos. A  $\approx 300 M_\odot$  popIII stars can collapse directly into a SMBH of  $\approx 200 M_\odot$  after only about 2 Myr at  $z \approx 20 - 50$ , leaving behind a few hundred solar mass remnant that can possibly play the role of a seed SMBH.

Another seed formation path way is the **gas dynamical collapse**: the core of a  $10^4 - 10^5 M_\odot$  cloud collapses at the center directly into a SMBH or disk of gas at  $z \approx 5 - 10$ . Such a massive seed can grow more easily than lighter masses. Globally unstable gas falls in the center of galaxy and create a supermassive star. To avoid the star explosion as a supernova, gas accumulation must occur rapidly. At the end of its life, the core of this

star contracts and forms a SMBH, which is still embed by the infalling gas of the remnant. The resulting system is a quasi-star in which the black holes eats its surroundings, growing up, ready to begin its life as a SMBH seed.

The third option is **stellar dynamical collapse** in which stars merge in high density cluster, form a very massive star and then collapse into a  $\approx 10^3 M_\odot$  black hole at  $z \approx 10 - 15$ . Dense stellar clusters have negative heat capacity, implying that stars start to form in the central region, creating a dense stellar cluster. Clusters formed in this way are crowded places. Star-star collisions in their core can produce a very massive star of up to a few thousand  $M_\odot$ , leaving behind a seed BH remnant of  $\approx 1000 - 2000 M_\odot$ .

These alternatives are not mutually exclusive, and currently there is not direct observation that can probe specific SMBH formation scenarios, even because the first SMBHs in the early universe have modest masses and luminosities.

## 1.10 Early SMBH growth

Once they formed, SMBHs seed need to accrete an enormous amount of mass in short time (they have to reach  $10^9 M_\odot$  in less than 1 Gyr) to the point that is challenging for structure-formation and evolution models of massive black holes and galaxies.

Beginning from seeds, these masses reached in a given time are:

$$M(t)_{QSO} = M_{seed} e^{\frac{1-\epsilon}{\epsilon} \frac{t}{t_S}} \quad (1.22)$$

If  $\epsilon$  do not evolve, the BH mass increases on a characteristic timescale, the Salpeter time  $t_S$ , the timescale for black hole growth under the hypothesis is that the black hole grows at Eddington limit.

$$\frac{t}{Gyr} = 0.45 \frac{\epsilon}{1-\epsilon} \frac{L_{Edd}}{L_{bol}} \ln\left(\frac{M_{QSO}}{M_{seed}}\right) \quad (1.23)$$

The more the BH radiate efficiently, the more time needs to reach that mass. As the age of the universe at  $z \approx 6.5$  is only  $\approx 0.83$  Gyr, equation 1.23 implies that only very massive seeds ( $\approx 10^6 M_\odot$ ) would be able to form the observed supermassive black holes at Eddington limit.

A way to mitigate this tension is to assume that these early black holes go through phases of super-Eddington accretion. Also a radiatively inefficient accretion scenario with  $\epsilon = 0.01 - 0.001$  (Volonteri et al., 2015; Trakhtenbrot et al., 2017; Davies et al., 2019), could decrease the quasar lifetime required to grow the SMBHs.

Plots in fig. 1.6 and 1.7 consider different values for parameters from equation (1.23). State-of-art model assuming that the accretion history of SMBHs may be episodic but with an extremely rapid accretion (e.g, Madau et al., 2014; Volonteri & Silk, 2014; Pezzulli et al., 2017; Begelman & Volonteri, 2016; Dubois et al., 2014). These phenomena

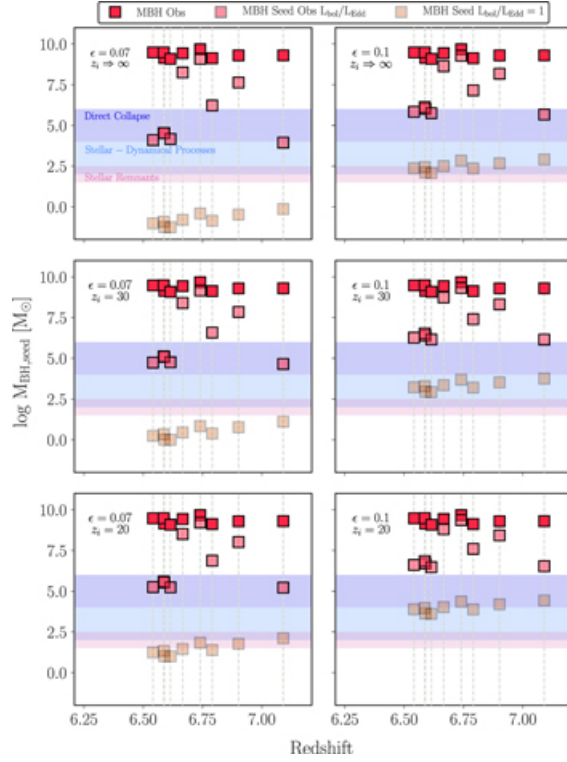


Figure 1.6: Masses of the black hole seeds required to obtain the observed black hole masses in the quasar sample from Mazzucchelli et al., (2017) (dark red squares). Authors here vary the efficiency ( $\epsilon = 0.07/0.1$ , left and right columns) and the redshift of the seed formation ( $z_i \Rightarrow \infty/30/20$ , from top to bottom). For each case, they assume that the sources accrete constantly with the observed Eddington ratio (light red squares), and at Eddington rate (yellow squares). The range of black hole seeds predicted by current theoretical models are shown in orange, light blue and deep blue shaded areas. Black hole seeds with masses  $\geq 10^2 M_\odot$  can produce the observed highredshift quasars in all cases with  $\epsilon = 0.07$  and  $\lambda = 1$ , and in case of  $[\epsilon = 0.1, \lambda = 1$  and  $z \Rightarrow \infty]$ . If the efficiency is higher (10%), and the seeds form at  $z_i \approx 30 - 20$ , their predicted masses are correspondingly larger ( $\approx 10^3 - 10^4 M_\odot$ , at Eddington accretion). From Mazzucchelli et al., 2017

cause a flaring activity of the quasar, and blow the accreting material off the center of the host galaxy. So luminous quasar phases are regulated by quasar feedback processes in which accretion immediately stops and the most of outflow material falls back again

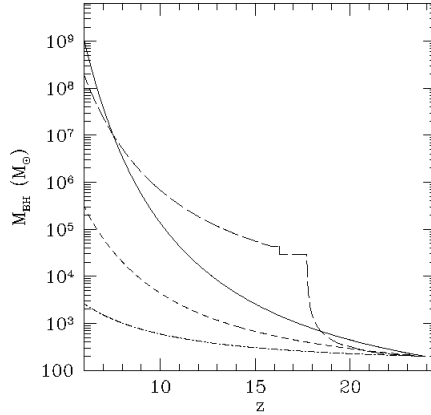


Figure 1.7: Assuming different accretion rates, or the same accretion rate with different radiative efficiencies the mass of a MBH starting accreting at  $z = 24$  can be dramatically modified. Eddington limited accretion:  $\epsilon = 0.1$  (solid line),  $\epsilon = 0.2$  (short dashed line),  $\epsilon = 0.4$  (dot-dashed line). Super-critical accretion, as in Volonteri & Rees 2005 (long dashed line). From Volonteri & Rees, 2006

towards the black hole (Costa et al., 2014). The emergent luminosity is approximately the Eddington value, but the growth rate is much higher.

The accretion flow onto the SMBH is the ultimate energy source in AGN and the most important component in determining their observational characteristics. Turning a normal galaxy into an AGN requires a relatively high accretion rate of the SMBH. Changes in the accretion flow are also the source of the bulk of observed variability in AGN (Padovani et al., 2017).

## 1.11 The quasar population at $z > 5.5$

To date, about **300** quasars were discovered at very high redshift, the most with optical/NIR survey (Fan et al., 2000, 2001, 2002, 2003, 2004, 2006; Jiang et al., 2008, 2009; Willott et al., 2007, 2009, 2010; Banados et al., 2014, 2016; Mortlock et al., 2011; Venemans et al., 2013, 2015; Matsuoka et al., 2016, 2018; Yang et al., 2017, 2018). They have masses in a range of  $10^8 - 10^{10} M_{\odot}$ , and luminosities  $L > 10^{45}$  erg/s, fig. 1.8 illustrates the distribution of quasar luminosities versus SMBH masses.

An efficient and successful methods to identify high-redshift quasars is through the Lyman-break technique (Fan et al., 2000): absorption by neutral hydrogen causes a break in the observed galactic spectrum. In fig.1.9 the quasar shows a blue continuum

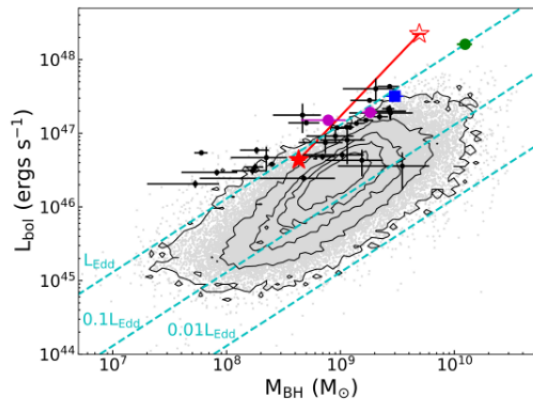


Figure 1.8: Distribution of quasar bolometric luminosities and SMBH masses estimated from Mg II emission. The open red star represents J0439+1634 without lensing correction; the filled red star represents the same object after applying a lensing magnification correction factor of 51x (from the fiducial lensing model in Table 1). The green circle represents SDSS J0100+2922 at  $z = 6.30$  (Wu et al., 2015), the blue square SDSS J1148+5251 at  $z = 6.42$  (Fan et al., 2003), and the magenta circles ULAS J1120+0641 at  $z = 7.09$  (Mortlock et al., 2011) and ULAS J1342+0928 at  $z = 7.54$  (Banados et al. 2018). Black dots denote other  $z > 6$  quasars (Wu et al., 2015; Mazzucchelli et al., 2017). The black contours and grey dots show SDSS low redshift quasars (Shen et al., 2011) (with broad absorption line quasars excluded). The error bars represent the  $1\sigma$  measurement errors. For comparison, the dashed lines illustrate fractions of the Eddington luminosity. From Fan et al., 2019

with a sharp cut-off, associated with the onset of Ly- $\alpha$  absorption.

Because of this, quasars at redshift  $z > 5.5$  are characterized by very red color (corresponding at a large magnitude difference between the  $i$  and  $z$  bands,  $i - z > 2.2$ ) despite having a blue intrinsic continuum (Banados et al., 2016). At  $z > 5.5$  the optically thick Ly $\alpha$  forest absorbs most of the light coming from wavelengths  $\lambda_{rest} < 1216\text{\AA}$ , hence they are very faint or completely undetected in the  $i$ -band showing a drop in their spectra. This implies that objects at  $z \approx 6$  are undetected or very faint in the  $i$ -band. This drop can be measured by their red  $i$ - $z$  colors, called  $i$ -dropouts. The impact of the Lyman break at different redshifts on a sample of quasars in fig. 1.10 is clearly visible: at  $z > 6.5$ , nearly all of the quasar detectable spectrum is shifted outside the optical bands.

There are some contaminants for quasars at this redshifts. In fact, they can be confused

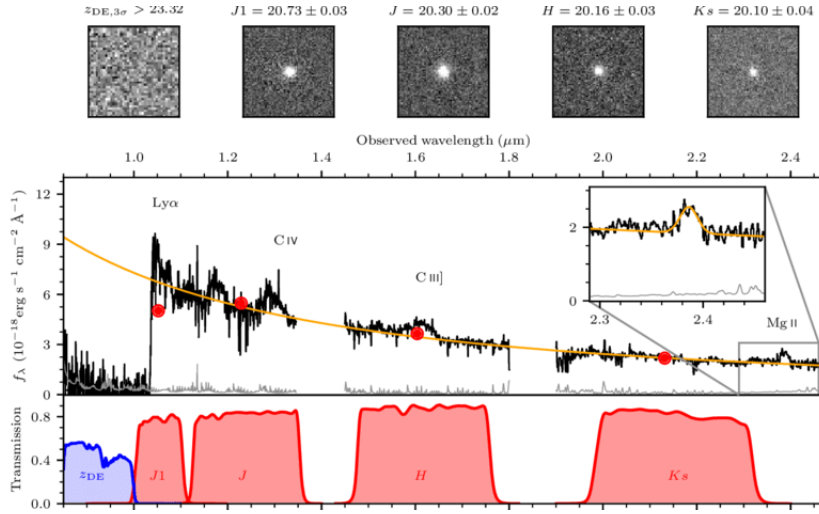


Figure 1.9: Photometry and combined Magellan/FIRE and Gemini/GNIRS near-infrared spectrum of the quasar J1342+0928 at  $z = 7.54$ . The  $1\sigma$  error is shown in gray and the orange line represents the best-fit power-law continuum emission. The red circles show the follow-up photometry taken with the Magellan/Fourstar infrared camera. The inset shows a Gaussian fit to the Mg II line. The bottom panel shows the transmission of the Fourstar J1, J, H, Ks (red), and the DECam z (blue) filters, while the top panel shows  $10 \times 10$  postage stamps of the quasar in the same filters with their respective AB magnitudes. From Banados et al., 2018

with cosmic rays and brown dwarfs, especially late-type M, L, and T dwarfs, which can have optical colors similar to quasars, but are much more abundant. The surface density of cool dwarfs is about 15 times higher than that of  $z > 5.5$  quasars; thus, J-band (near infrared) photometry ( $z - J < 1.5$ ) is used to separate these two classes of objects (Fan et al., 2000b), a color-color diagram is shown in figure 1.11.

To estimate the **SMBH mass** is used the single-epoch estimator, under the assumptions of virialized motion in the broad-line region (BLR) clouds (Shen, 2013) and that relation 1.1 holds also at high redshift. With the continuum luminosity as a proxy for the BLR radius and the broad emission line width, characterized by the FWHM, as an indicator of the virial velocity, the virial mass estimate can be expressed as:

$$\log \frac{M_{BH}}{M_{\odot}} = a + b \log \frac{L_{\lambda}}{10^{44} \text{ erg/s}^{-1}} + 2 \log \frac{FWHM}{\text{km s}^{-1}} \quad (1.24)$$

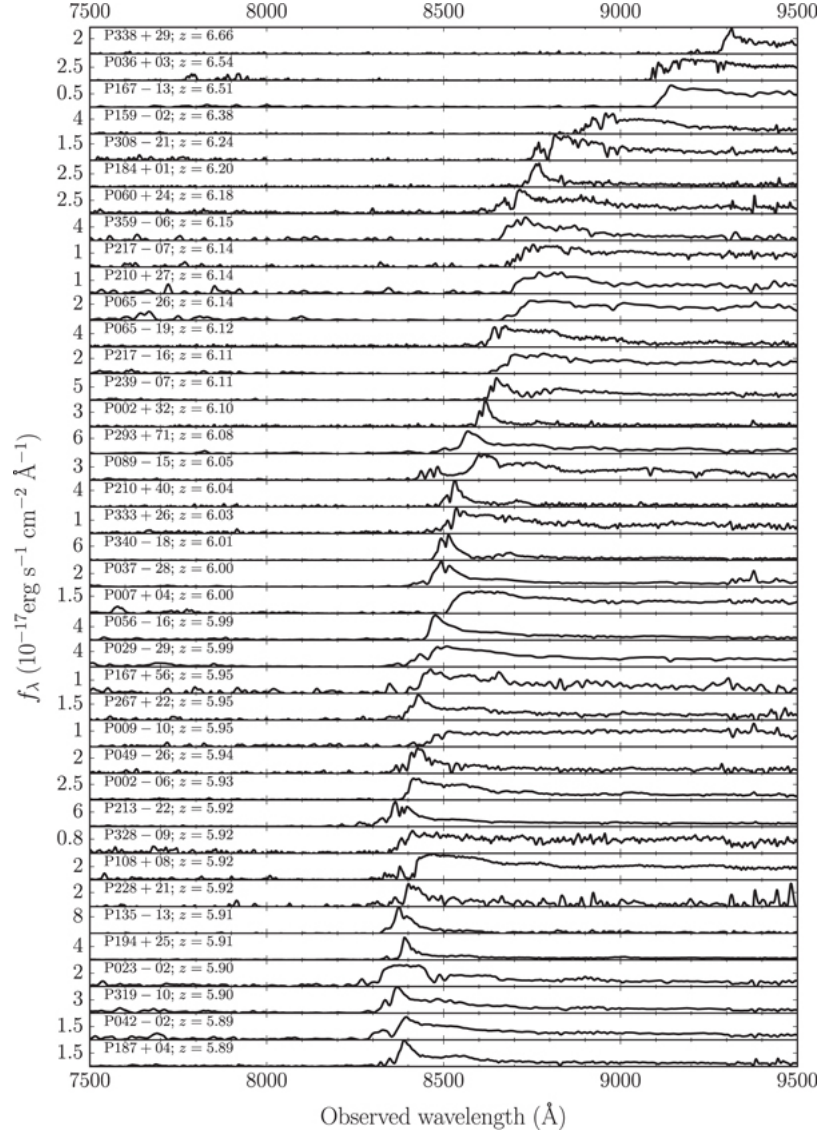


Figure 1.10: Compilation of optical spectra of known  $z > 5.7$  quasars. The impact of the Lyman break at different redshifts is clearly visible. At  $z > 6.5$ , nearly all of the quasar detectable spectrum is shifted outside the optical bands. From Fan et al., 2012

where  $L_\lambda$  is the monochromatic continuum luminosity at the wavelength  $\lambda$ . FWHM is the full width at half maximum of the broad emission line, and the coefficients  $a$  and  $b$  are empirically calibrated against local AGN with Reverberation Mapping (RM) masses and internally with other lines and scaling relations between UV and optical lines. Typically,

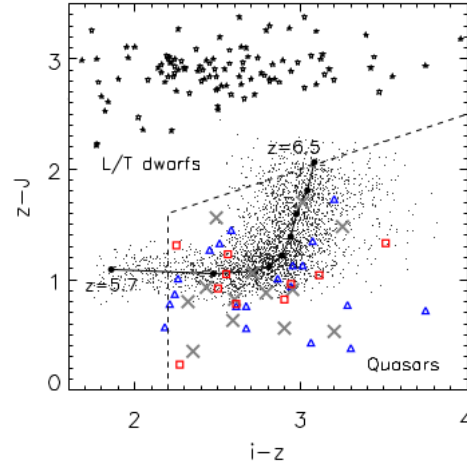


Figure 1.11: The  $z$ - $J$  versus  $i$ - $z$  color-color diagram for quasar candidate selection. The open stars represent a sample of known L/T dwarfs drawn from DwarfArchives.org. The black dots represent simulated quasars with a luminosity of  $M_{1450} \approx -26$  mag at  $5.5 < z < 6.5$ . No photometric errors are added. The black circles show the median track of quasar colors. The dashed lines indicate our selection criteria. The blue triangles, gray crosses, and red squares represent the SDSS quasars that have  $J$ -band photometry in the main survey, Stripe 82, and overlap regions, respectively. From Jiang et al., 2016

the most used lines are Mg II and C IV and the most common calibration is the one from Vestergaard & Peterson (2006).

## 1.12 AGN evolution

The space density of quasars has a peak at  $z \approx 2$  and then exponentially decreases up to  $z \approx 6$ , while the space density of low-luminosity AGN peaks at  $z \approx 0.5$  and decreases up to  $z \approx 4$  (Schmidt et al., 1995, Boyle et al., 2000), as shown in figure 1.12. This effect is called *downsizing* and appears to be in contrast with the hierarchical scenario (Cowie et al., 1996).

The two most popular models to explain this behavior are:

- the Luminosity Dependent Density Evolution model (Miyaji et al., 2000; Ueda et al., 2003; La Franca et al., 2005; Hasinger et al., 2005; Silverman et al., 2008; Ueda et al., 2014), which assumes that the space density of AGN evolves differently for different luminosities and there is no actual evolution in luminosity;

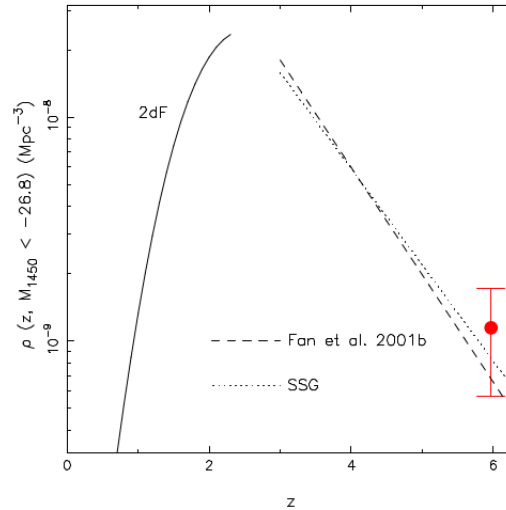


Figure 1.12: From Fan et al., 2001. The evolution of quasar comoving spatial density at  $M_{1450} < -26.8$ . The large dot represents the result from the survey. The dashed and dotted lines are the best-fit models from Fan et al. (2001b) and Schmidt et al. (1995), respectively. The solid line is the best-fit model from the 2dF survey (Boyle et al., 2000) at  $z < 2.5$

- the Luminosity And Density Evolution model (Aird et al., 2010), in which the AGN population evolves independently in luminosity and density with cosmic time.

A possible evolutionary scenario (Hopkins et al., 2008; Hickox et al., 2009) suggests that SMBHs hosted in low mass halos grow in isolation, while SMBHs harboured in massive halos have a much higher probability of experiencing a merger. Dark matter halos and their associated galaxies undergo many mergers as mass is assembled from high redshift to the present (Volonteri et al., 2017).

Following galaxy mergers, two SMBHs are segregated to the center of the remnant due to dynamical friction. During the merger, the cold gas content of the interacting system is highly unstable, leading to an inflow in the nuclear region that provide a large reservoir of fuel for the active phase of the SMBHs (Di Matteo et al., 2005; Hopkins et al., 2005; Springel et al., 2005).

At the same time, the dense nuclear cold gas trigger efficiently star formation episodes, that compete with the gas supply in SMBHs and deplete the reservoir of available gas. These feedback episode set the SMBHs growth, giving shape to the SMBH-host relations observed in the local Universe (Magorrian et al., 1998; Ferrarese & Merritt, 2000; Marconi & Hunt, 2003; Kormendy & Ho, 2013). This large amount of accreting gas can also trigger the star formation in the host galaxy until the AGN is powerful enough to produce a

negative radiative/kinetic feedback that halts the star formation and blows away the accreted gas, turning off the quasar phase.

Consequently, the most massive SMBHs seem to accumulate their mass before the lighter ones in a downsizing scenario. But observations put on evidence that the merger driven accretion paradigm is not the whole story. Seyfert galaxies are in general characterized by clumpy structures rich of cold gas, and most of them show dense nuclear stellar clusters with densities of  $\approx 10^6 M_{\odot} \text{ pc}^{-3}$ . In such a rich environment, the principal SMBHs growth channel is thought to be the random accretion of small packets of material (molecular clouds) reaching the galactic nucleus because of dynamical relaxation and secular evolution processes (Hopkins et al., 2006) and fueling the dormant SMBH.

This feeding way is likely unimportant in giant ellipticals, where the nuclear densities are much lower and the content of cold gas very small as a consequence of AGN feedback and stellar winds loss related to the last accretion episode, resulting in a pronounced lack of molecular clouds (Sesana, 2011). Such scenario is also displayed in fig.1.13.

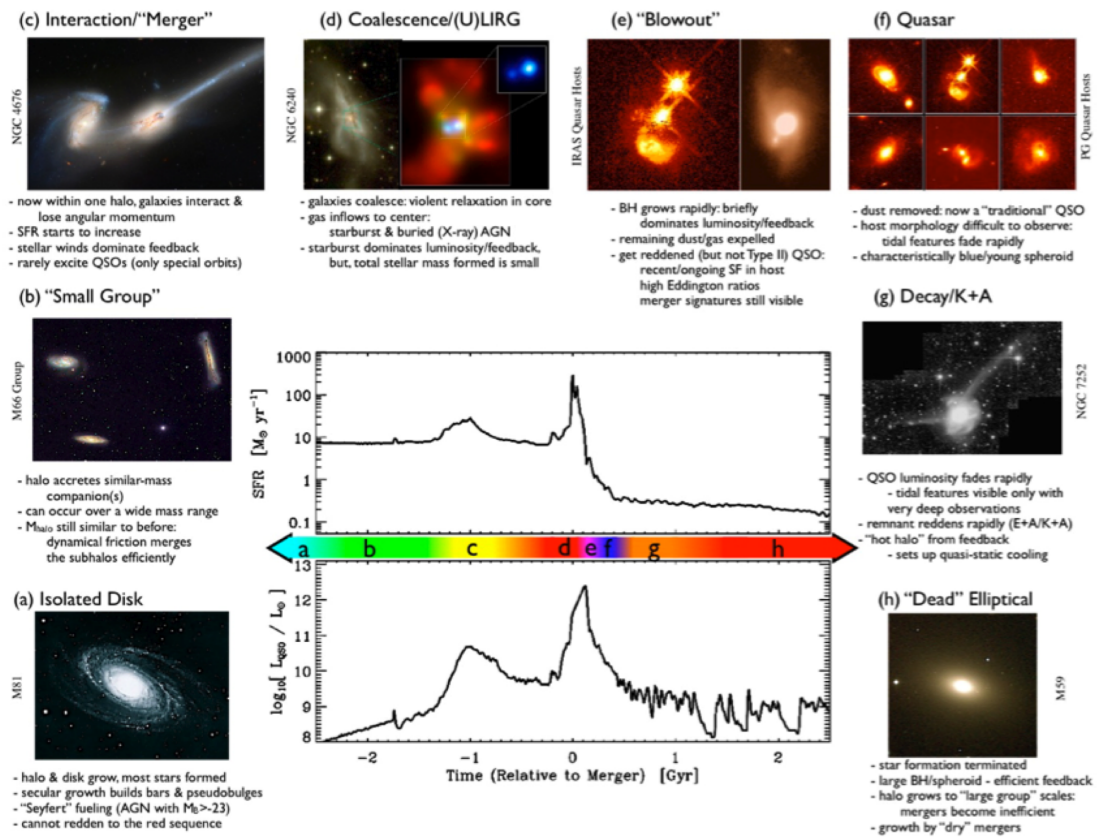


Figure 1.13: Infographic showing the sequence of events that model a typical galaxy becoming a so-called "red and dead" elliptical. The scheme should be read clockwise from (a) to (h). The big central panel shows the temporal evolution of the star formation rate (upper part), and luminosity of the quasar (lower part). During the supply of gas in the central part of the galaxy (d-e phases) there are both the peaks of star formation and quasar emission. On later stages, the QSO quenches the SFR and expels the gas from the central region. Then, also the QSO luminosity fades away and the host galaxy turns into a passive one. From Hopkins, et al., 2008



# Chapter 2

## Variability of high redshift quasars

### 2.1 The sample of this study

The main aim of this work is to study, for the first time, the variability in the rest-frame optical/UV continuum of a small sample of  $z > 5.5$  sources, when the Universe was less than 1 Gyr. This redshift corresponds to the wavelength range sampled with the z-band photometry, a filter mounted in Pan-STARRS, Sloan Digital Sky Survey, DECaLS and also in the BFOSC of Cassini Telescope, near Bologna. Comparing the magnitudes measured from new observations taken by Cassini telescope with catalogs of surveys such as SDSS and Pan-STARRS, it is possible to search for significant variation of the most distant quasars on timescales that span over more than a decade. The relative photometry allow for an higher and more stable photometric calibration than observing standard fields, that is fundamental to the results. These studies could be a chance to test the flaring scenario, despite the redshift dilution of the time intervals. If the variability of these high redshift quasars is associated with the interplay of accretion and feedback, it is expected that the hottest component of the AGN Big Blue Bump (the continuum emission from the accretion disk that is observed at rest-frame optical/UV wavelengths) is the most sensitive to rapid fluctuations. This implies that the largest variations are expected in the rest-frame optical/UV in a couple of years.

### 2.2 Photometric information from wide area surveys

As distant ( $z > 5.5$ ) luminous quasars are rare, with an estimated source density of  $\approx 1 \text{ Gpc}^{-3}$  (Fan et al., 2004; Willott et al., 2010b). In order to understand the properties of these objects, large area and deep surveys are key to progress in quasar research, hence numerous surveys have been carried out over the years, such as:

- the Sloan Digital Sky Survey (SDSS);
- the Canada-France High-Redshift Quasar Survey (CFHQS);
- Panoramic Survey Telescope and Rapid Response System (Pan-STARRS);
- the UKIDSS Large Area Survey (ULAS);
- the Dark Energy Camera Legacy Survey (DECaLS);
- the VISTA Survey (ATLAS and VIKING).

Useful surveys for this thesis work are SDSS, Pan-STARRS and DECaLS, because they provide a faster and easily access to test the variability in the optical band.

### 2.2.1 Sloan Digital Sky Survey

Sloan Digital Sky Survey saw first light in 1998 and entered routine operations in 2000. During this time it has progressed through several phases: SDSS-I (2000-2005), SDSS-II (2005-2008), SDSS-III (2008-2014), SDSS-IV (2014-2020) and SDSS-V (2020-2025).

SDSS uses a dedicated 2.5 m f/5 modified Ritchey-Chrétien altitude-azimuth telescope located at Apache Point Observatory, in south east New Mexico, USA (in fig.2.2); a 1.08 m secondary mirror and two corrector lenses result in a  $3^\circ$  distortion-free field of view; the Irénée du Pont Telescope at Las Campanas Observatory in northern Chile, a Ritchey-Chrétien 2.5 m f/7.5 telescope with a Gascoigne corrector lens; the NMSU 1-Meter Telescope at Apache Point Observatory.

This program has produced some of the most detailed three-dimensional maps of the Universe ever made, with deep multi-color images of more than 1/3 of the sky and spectra for more than three million astronomical objects, it took a total of around 35000 square degrees of images, covering 14055 square degrees of sky.

SDSS discoveries from its earliest campaigns, provided extensive studies of quasar, giving the most detailed description of the growth of black holes since the first billion year of the Universe, hundred of times more than existing samples. In addition, SDSS spectra show that the properties of quasars have changed very little from the early cosmic epoch to the present. Studies from SDSS survey probed the dark matter environments of quasars through clustering measurements, revealed populations of dusty obscured quasars, unveiled clouds moving under gravitational effect of the central black hole, and made a comprehensive census of the much fainter accreting AGN in present-day galaxies.

Five filters operate on SDSS telescope (u, g, r, i, z), their characteristics are shown in table 2.1 and fig.2.1). In this work was used z-Gunn PSF magnitudes from the Data Release 16, the fourth data release of the fourth phase of the Sloan Digital Sky Survey.

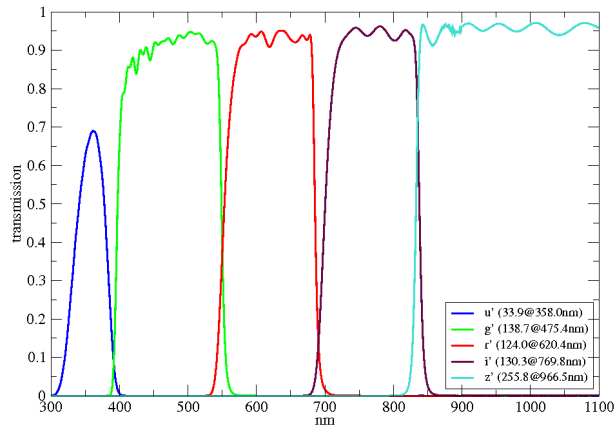


Figure 2.1: Filter response in SDSS: blue line is u, green line is g, red line is r, purple line is i, cyan is z .From Gunn et al., 1998

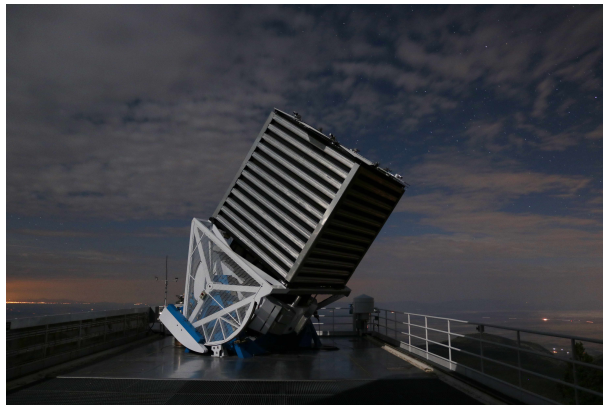


Figure 2.2: The SDSS telescope at night. Image Credit: Patrick Gaulme

### 2.2.2 Panoramic Survey Telescope and Rapid Response System

Pan-STARRS (Panoramic Survey Telescope And Rapid Response System) is a system for wide-field astronomical imaging developed and operated by the Institute for Astronomy at the University of Hawaii (Chambers et al., 2016, T.J. Tonry et al., 2012, C. Stubbs et al., 2010, D. Scolnic et al., 2015). The first telescope, Pan-STARRS1 (PS1) has a diameter of 1.8 m and is located near the summit of Haleakala on the Island of Maui (fig.2.4). It is equipped with the world's largest digital camera, with almost 1.4 Gigapixel camera (GPC1) to image the sky in five broadband filters ( $g$ ,  $r$ ,  $i$ ,  $z$ ,  $y$ ) with a field of view (FoV) of 7 square degrees. A similar telescope but with a slightly larger digital camera,

Pan-STARRS2 (PS2), with almost 1.5 billion pixels, has been constructed adjacent to PS1. PS1 first data release (DR1) occurred on December 2016 while PS1 DR2 occurred on January 2019.

The entire available sky can be observed several times each month: each night, PS1 observes about 1000 square degrees, using a sequence of four exposure on a period of about an hour, thanks to the combination of small mirrors and large cameras. PS1 offers an excellent opportunity to hunt for high-redshift quasar searches for several reasons, the main are:

- it provides a larger covering area than previous high-redshift quasar surveys, especially in the southern hemisphere;
- it goes deeper in magnitude than SDSS in the red part of the optical spectrum where  $z \approx 6$  quasars are visible;
- the additional y-band ( $\lambda_{eff} = 9620\text{\AA}$ ;  $FWHM = 890\text{\AA}$ ) allows the search for luminous quasars beyond the SDSS limit ( $z > 6.5$ ) over more than 20000 square degrees of extragalactic sky.

The characteristics of filters are listed in table 2.1 and shown in fig.2.3. Under certain circumstances PS1 observations are obtained with a sixth, a filter designated as  $w_{P1}$  that essentially spans the gri bands.

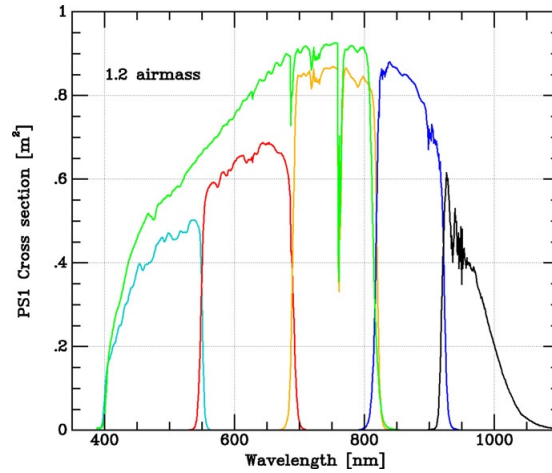


Figure 2.3: From Tonry et al., 2012: The PS1 capture cross-section in  $\text{m}^2/\text{e}/\text{photon}$  to produce a detected  $e^-$  for an incident photon for the six Pan-STARRS1 bandpasses, g (cyan line) r (red line) i (yellow line) z (blue line) y (black line) and w (green line) for a standard airmass of 1.2



Figure 2.4: PanSTARRS1 Observatory on Haleakala, Maui just before sunrise. Rob Ratkowski, copyrighted by PS1SC. All rights reserved.

There are significant differences between the filter system of Pan-STARRS1 and other surveys. In particular, an important difference, fundamental in this thesis work, is that the  $z_{P1}$  filter has a sharply defined cut-off at  $9222\text{\AA}$ , which is contrast to the SDSS-z band which is has no red cut off and the response is defined by the detector response, as could be seen in the right side of figure 2.5.

### 2.2.3 The Dark Energy Camera Legacy Survey

The Dark Energy Camera (DECam) on the Victor M. Blanco 4 m telescope (fig.2.7), is located at the Cerro Tololo Inter-American Observatory, in Chile (Flaugher et al., 2015). It provides the optical imaging for targeting for 2/3 of the Dark Energy Spectroscopic Instrument (DESI) footprint, covering both the North Galactic Cap region at  $\text{Dec} \leq 32$  and the South Galactic Cap region at  $\text{Dec} \leq 34$  (Dey et al., 2019). The Dark Energy Survey (DES) observed 5000 squared degrees of the sky in five filters (g,r,i,z,Y), in fig. 2.6 and table 2.1.

The program was completed in March, 2019. In this work was used photometry from DR8 in the z-band.

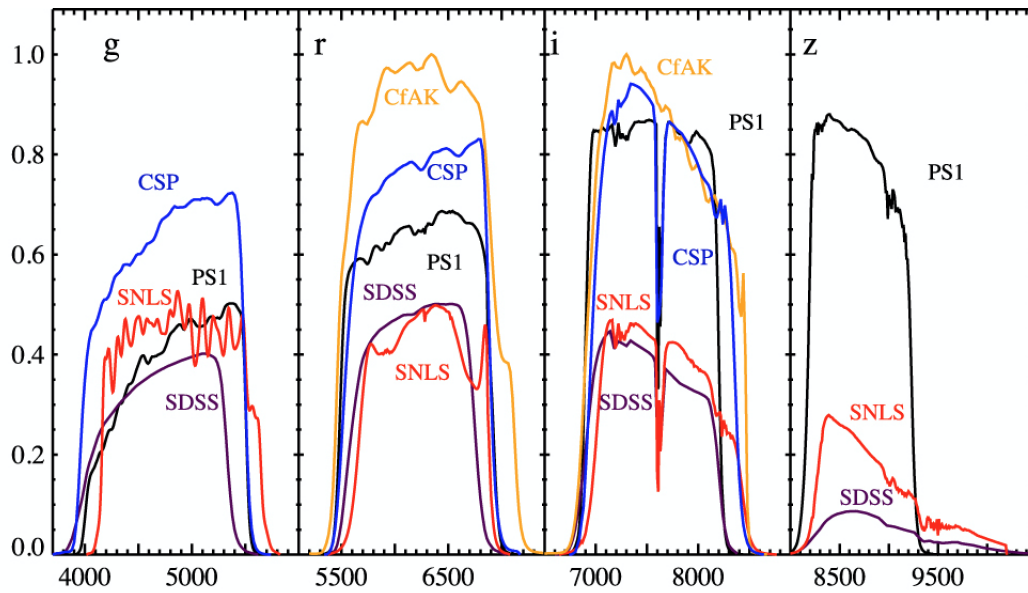


Figure 2.5: From Scolnic et al., 2015: comparisons between the  $griz_{P1}$  and other survey filters (CSP = Carnegie Supernova Project and CfAK = CfA-Keplercam, SNLS = Supernova Legacy Survey).

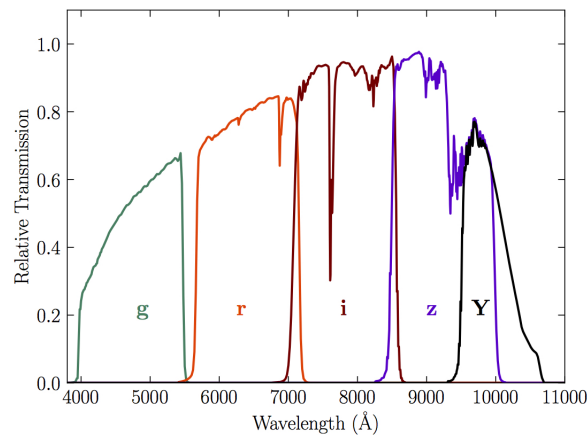


Figure 2.6: DES DR1 Standard Bandpasses for the DECam  $g$ ,  $r$ ,  $i$ ,  $z$  and  $Y$  filters. The bandpasses represent the total system throughput, including atmospheric transmission (airmass = 1.2) and the average instrumental response across the science CCDs. From Abbott et al., 2018

Filter <sub>PS1</sub>	$\lambda_{PS1}$	FWHM <sub>PS1</sub>	$\lambda_{SDSS}$	FWHM <sub>SDSS</sub>	$\lambda_{DECaLS}$	FWHM <sub>DECaLS</sub>
u	-	-	3551	6000	-	-
g	4866	1256	4886	1400	4720	1520
r	6215	1404	6165	1400	6415	1480
i	7545	1296	7481	1500	7835	1470
z	8679	1034	8931	1200	9260	1520
y	9633	628	-	-	10095	1130

Table 2.1: PS1, SDSS and DECaLS filters. (1) Filter; (2), (4) and (6) central wavelength in [ $\text{\AA}$ ]; (3), (5) and (7) FWHM in [ $\text{\AA}$ ].



Figure 2.7: DECaLS telescopes. Credit: H. Stockebrand



# Chapter 3

## The photometric follow-up from Loiano

### 3.1 Cassini Telescope

Inaugurated in 1976 and dedicated to the astronomer Cassini, the Telescope of Loiano is property of the University of Bologna (in fig.3.2). The primary mirror has a diameter of 152 cm while the second mirror, located 4 m of distance from the main, has a diameter of 60 cm. It is the second telescope in Italy for size. The main instrument is BFOSC (Bologna Faint Object Spectrograph and Camera), a focal reducer with multi-functional optics, built to allow, with a simple configuration change, the acquisition of both images and spectra.

The research areas cover most of the fields of modern astrophysics and technology for astronomy, such as:

- studies on stellar populations and galactic evolution;
- studies of the structure, evolution and distribution of galaxies, clusters and active galactic nuclei (AGN), and their contribution to the cosmological structure;
- numerical studies in the field of gas hydrodynamics and numerical simulations of turbulent phenomena;

The instrument consists of a rigid support hosting the collimator, the camera and the detector. Mounted on it there are the shutter and three moving wheels that carry slits, filters and grism respectively. BFOSC is equipped with five slits (1.5", 2", 2.5", 5", 12") normally oriented in E-W direction, nine filters ( $u$ ,  $b$ ,  $v$ ,  $r$ ,  $i$  Johnson-Kron-Cousin and  $g$ ,  $r$ ,  $z$ ,  $i$  Thuan-Gunn) and eleven grisms. As is showed in picture 3.1, these last filters

are the same mounted on SDSS telescope and their characteristics are visible in table 2.1.

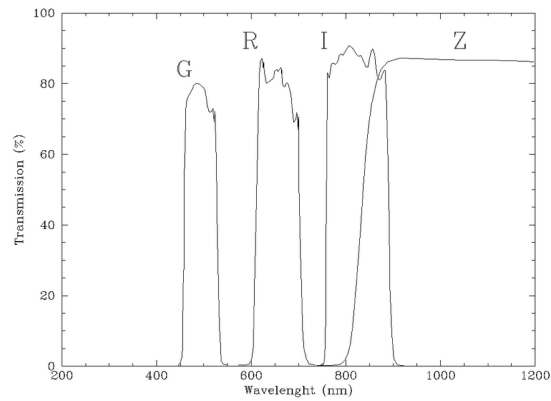


Figure 3.1: Gunn filter transmission curves of Loiano Telescope



Figure 3.2: Loiano Telescope, picture taken on 23 February 2020

## 3.2 Our observational campaign

Among the 300 discovered high redshift quasars, described in section 1.11, was performed a selection based on the following characteristics, in order to permit to conduct the observations from Loiano:

- $5.5 < z < 6.5$ , that corresponds to the wavelength range sampled with the z-Gunn photometry;
- $m_{1450} < 19.5$ , mag to have high S/N ratio required to measure flux variations;
- $\text{Dec} > -10$ , to have a good visibility from Loiano.

A sample of 22 quasars matched these criteria in redshift, magnitude and declination. All these objects are listed in table 1.9.

Data were taken from the 152 cm Loiano Telescope with z-Gunn filter on 27 February 2019, 03 July 2019 and from 15 February 2020 to 23 February 2020. During this period, not all of targets were observed, mostly because they were not visible during the period of observations and because bad weather conditions during the run; while some target were observed more than one time.

Therefore, the final sample was composed by 13 sources, taking 4 observation for target with a 15 minutes exposure (1 hour for source) and 10 bias and 10 flats per night. For data reduction and analysis two software were used: *IRAF* (Image Reduction and Analysis Facility), a collection of software written at the National Optical Astronomy Observatory (NOAO), and *SAOImageDS9*, an image display and visualization tool for astronomical data. In addition, Supermongo and Python libraries *numpy*, *matplotlib*, *pandas* and *astropy* were used for astrometry calibration and plots.

Target	RA	Dec	Redshift	$m_{1450}$	Observed	Seeing
J0002+2550	00:02:39.390	+25:50:34.80	5.82	19.44	No	-
F003+36	00:12:32.88	+36:32:16.1	5.55	19.27	No	-
J0100+2802	01:00:13.027	+28:02:25.84	6.326	17.68	Yes	1.61
J0148+0600	01:48:37.634	+06:00:20.09	5.98	19.43	No	-
F029+30	01:57:45.45	+30:01:10.7	5.74	19.22	No	-
P036+03	02:26:01.876	+03:02:59.39	6.541	19.3	No	-
J0439+1634	04:39:47.10	+16:34:15.8	6.5	17.65	Yes (3 times)	1.67/2.09/2.27
P071-02	04:45:48.182	-02:19:59.84	5.69	19.18	Yes	2.44
P108+08	07:13:46.306	+08:55:32.65	5.92	19.25	Yes (2 times)	1.59/2.13
J0818+1722	08:18:27.398	+17:22:51.79	6.02	19.29	Yes (2 times)	2.14/1.81
J0836+0054	08:36:43.851	+00:54:53.30	5.81	19.01	Yes	2.45
J1016+2541	10:16:37.71	+25:41:32.0	5.64	18.88	Yes	1.62
J1044-0125	10:44:33.042	-01:25:02.20	5.785	19.37	Yes	2.06
J1137+3549	11:37:17.733	+35:49:56.89	6.03	19.44	Yes (2 times)	2.04/2.34
J1148+5251	11:48:16.652	+52:51:50.44	6.419	19.04	Yes	2.17
J1335-0328	13:35:56.24	-03:28:38.2	5.67	18.79	Yes	3.03
F225+28	15:00:36.84	+28:16:03.0	5.62	19.36	No	-
J1545+6028	15:45:52.082	+60:28:24.01	5.78	19.06	No	-
P323+12	21:32:33.191	+12:17:55.26	6.588	19.28	Yes	2.92
J2207-0416	22:07:10.122	-04:16:56.28	5.53	19.01	No	-
J2310+1855	23:10:38.882	+18:55:19.70	6.003	19.15	Yes	1.54
F349+22	23:17:38.25	+22:44:09.6	5.59	19.31	No	-

Table 3.1: The sample of present study. (1) Target name. (2) Right Ascension (RA). (3) Declination. (4) Redshift. (5) Apparent magnitude at rest-frame 1450Å. (6) Observation flag. (7) Seeing during observations.

### 3.3 Data reduction

Standard data reduction was performed. Some noises on the image had to be fixed.

**Bias Effect:** is an instrumental noise due to electronics, it generates a plateau of about hundred counts added to the the image (readout noise). Bias frames are obtained with the shutter closed with an exposure time equal to zero.

Because of the response of the detector is not uniform (each pixel can react differently to the light), it is necessary to take **flat field**. There are two types of flats: sky flat (that are taken at dusk and dawn far from the Sun) or dome flat (in case of bad weather with the inside of the telescope dome illuminated).

**Sky subtraction** can be done into two different ways:

- *Dithering*: different observations of the sky are made, each image is obtained by moving the telescope on pixel scales; in this way a star will be in a region in one image and in the next image it will occupy a different region, so making the median, the image of the sky without stars could be obtained.
- *Nodding on Sky*: consists of making observations in succession of the object-sky, that is the observations of the object in question alternate with observations of the sky, in this way it is possible to subtract the sky from each image. It is important to respect the alternation of observations in such a way to have a sky to be subtracted for each relative image. Doing 20 images of the object and 20 of the sky, the variability of the sky would not be taken into account of dithering. The sky thus obtained was subtracted from the images already corrected for bias and flat.

For this work was used the dithering method.

IRAF commands (known as tasks) are organized into package structures. For the first part of this work, useful tasks were: `imcombine`, `imarithmic`, `imalign` and `imstatistics` that respectively for combining, doing arithmetical operations, aligning frames and doing statistics on images.

First of all, I needed to combine all bias images with median in order to create the *master bias* frame (see fig. 3.3a). Then, I subtracted it to the other frames (fig.3.3d).

In the same way, I combined the flat images and I created the *master sky flat* (fig.3.4a). Using `imstatistics` I obtained the mean counts from each frame for scaling it to the master sky flat and, after that, renormalizing it.

At this point, all frames were divided by the master sky flat (fig.3.3b).

After that, I produced the *sky image* doing a median of each target images, scaling it by the real sky value and subtracted it to each frame of the target (fig.3.4b). To align (with `imalign`) the sky-subtracted images (fig.3.4c), I took the position of reference stars and at the end, I combined the images. The sum of the bias, flat and background effect corrections provided the scientific images (fig.3.5b). In Appendix A all scientific images are shown.

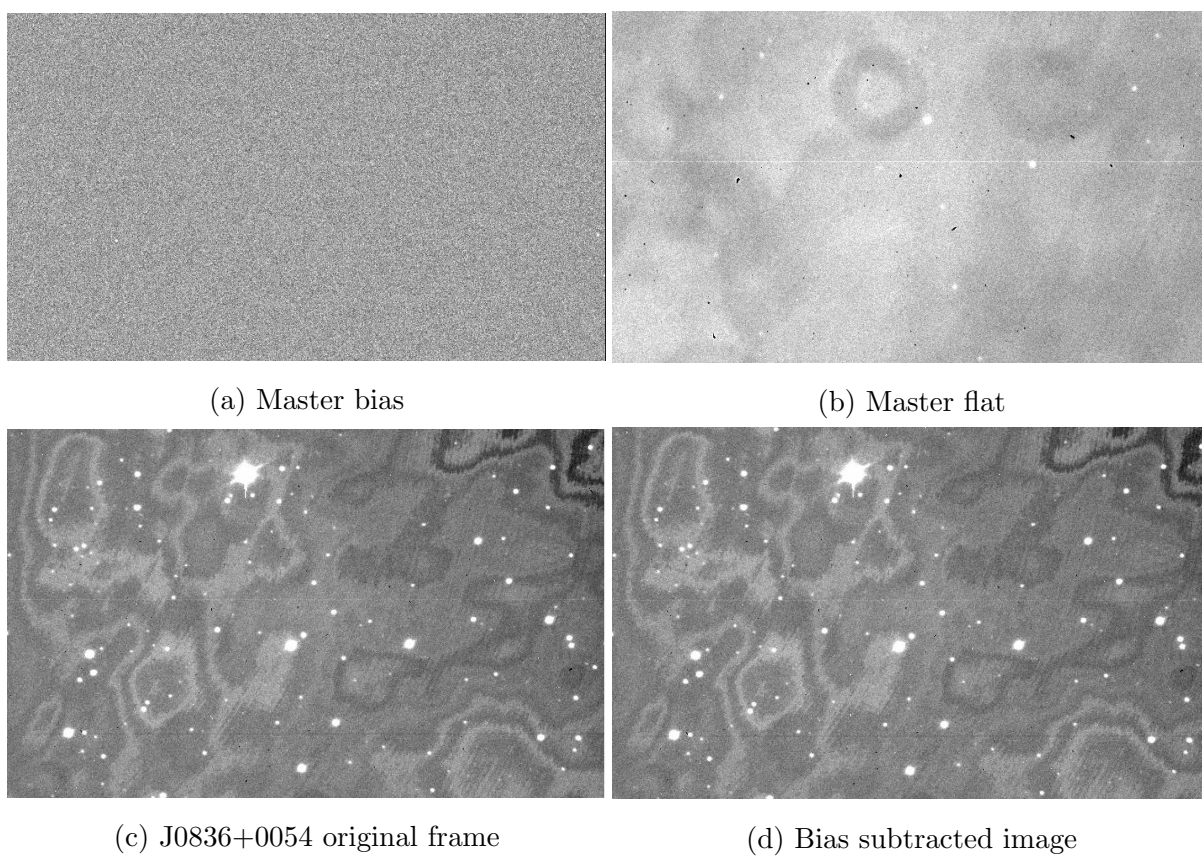


Figure 3.3: Data reduction process: master bias (3.3a), master flat (3.3b), original frame(3.3c), bias subtracted image(3.3d)

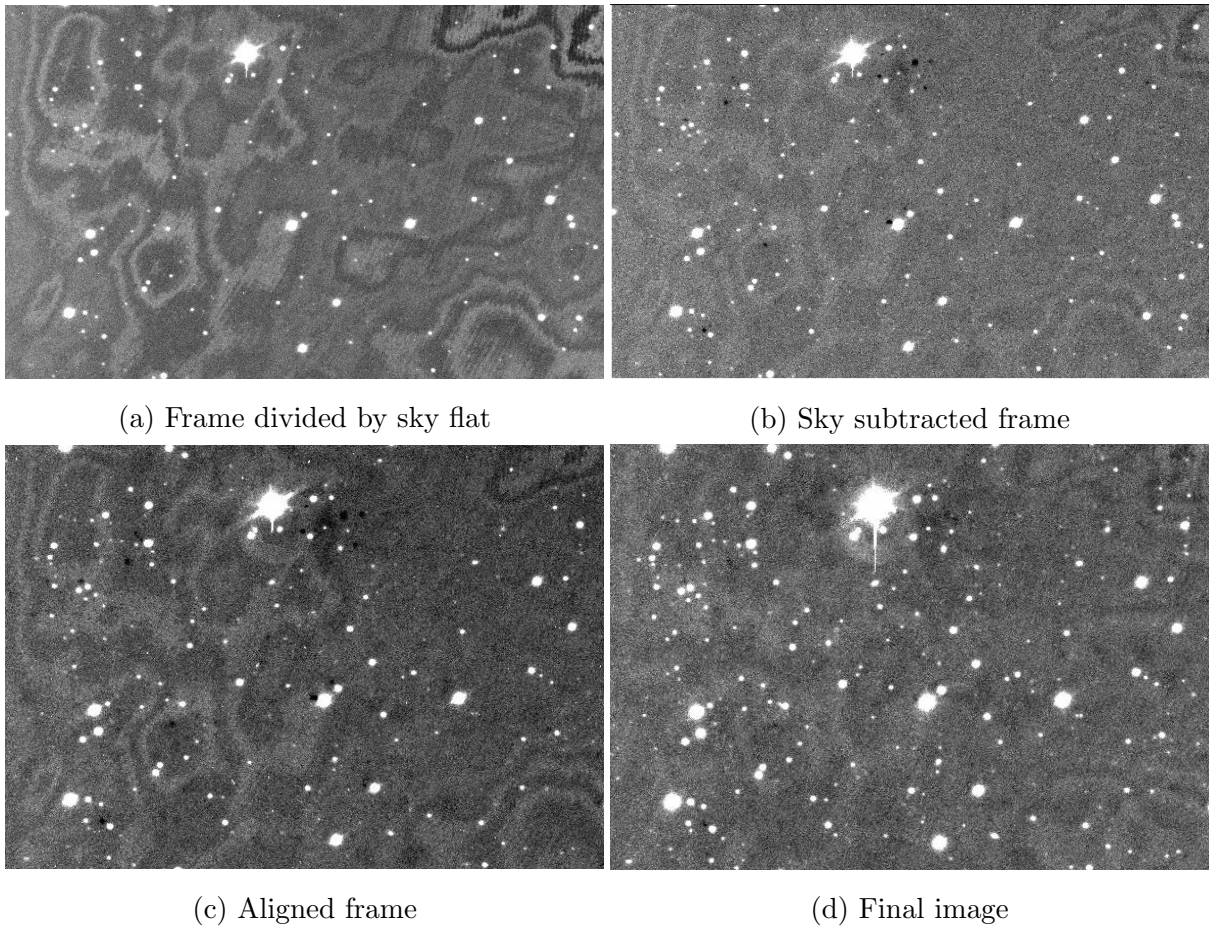


Figure 3.4: Data reduction process: division by sky flat (3.4a), sky subtraction (3.4b), aligning (3.4c) and final output (3.5b).

### 3.4 Data analysis

For the astrometrical calibration it was used the online tool `astrometry.net` (Lang et al., 2009) and a python-based code developed by *Lukas Wenzl* for a double check, in fig. 3.5 are shown the two output images. In both cases, the result was that in the file header some keywords were written: the reference pixel on axes x and y (`CRPIX1`, `CRPIX2`); the coordinate value in that pixel (`CRVAL1`, `CRVAL2`) and the values of the rotation and scale matrix it puts in relation the input and the output (`CD11`, `CD21`, `CD12`, `CD22`).

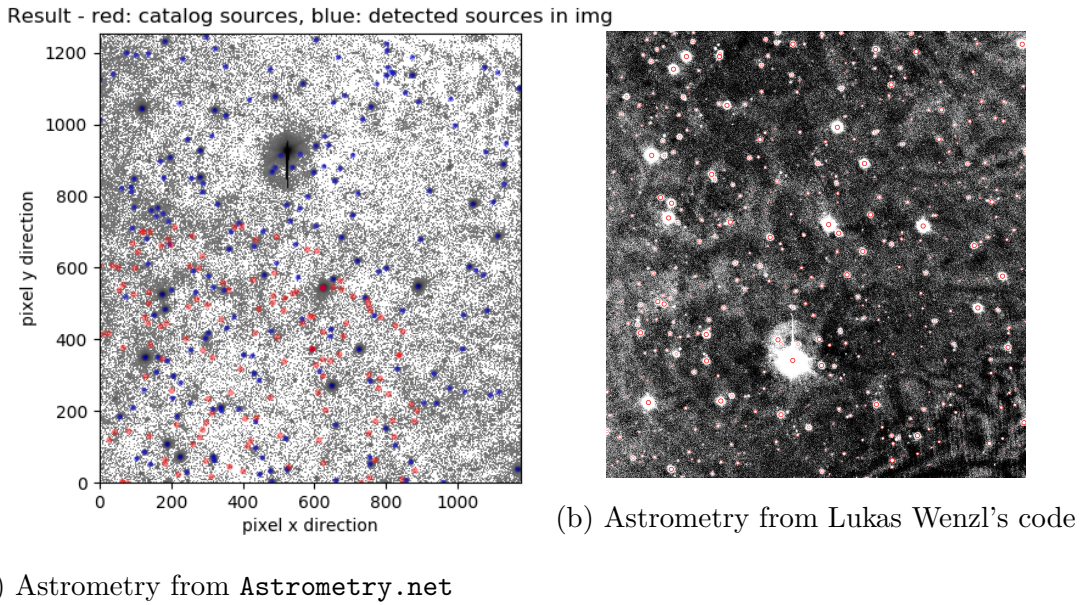


Figure 3.5: Astrometry calibration: `Astrometry.net` output (left) and Lukas Wenzl's code output (right)

Then, I downloaded `.csv` files of all targets from the Pan-STARRS catalog with 4 arcmin radius, . I took from it useful information named as `objID`, `raMean`, `decMean`, `epochMean`, `zMeanPSFMag`, `zMeanPSFMagErr`, `zMeanKronMag`, `zMeanKronMagErr`. In order to consider only point sources, I selected objects in which the difference of the z mean PSF and z mean Kron photometry was less than 0.2 magnitude. Taking the right ascension and declination from these selection, I created the input coordinate file and finally executed the task obtaining `.mag` files.

The IRAF task `qphot` was used for photometry, with a aperture of 3 times the seeing radius (that in the case of a perfectly Gaussian seeing, it should correspond to about 99% of the total flux) and of 6 times the seeing radius for annulus (the inner radius of

the sky annulus in pixels) and  $dannulus$  (the width of the sky annulus in pixels) and a zero point of 0. Choosing about 15 sources for each image, the task `imexamine` gave out the FWHM of them: the seeing radius was the half of the median FWHM value. The magnitude was then calculated considering the counts within the aperture radius from which those of the sky are subtracted (multiplied by the area of the aperture, in order to correctly rescaling the sky counts, provided per pixel, to those of the source area):

$$mag = -2.5 \cdot \log(sum - area \cdot msky) + zp \quad (3.1)$$

where  $msky$  are sky counts per unit of area,  $sum$  are the counts of the source in the opening radius, the area is calculated in pixels and  $zp$  is the zero point.

After that, from each sources I subtracted Pan-STARSS magnitude to the output magnitude of IRAF and I got the median value, that is the zero point of the magnitude scale. This passage is treated more extensively in Appendix B.

Finally, the quasar magnitude was measured by running again `qphot`, this time only at the coordinates of the target and adopting the newly measured zero point.

As already seen in 2.5, the PS1 z-filter cover a different range of wavelength compared to SDSS and Cassini z-filter, thus Dr. Decarli provided a correction. To do that, he took the quasar template from Selsing et al., (2015), shifted in redshift, corrected for the Gunn-Peterson effect following Meiksin (2006) convolved with the  $z_{gunn}$  filters of SDSS and  $z_{ps1}$  for Pan-STARRS, hence he obtained the expected magnitude in the two filters. The correction comes from the difference between these two magnitudes. I interpolated this correction with the redshift of each target of my sample and added the correction to the Pan-STARRS magnitude in order to obtain the corresponding magnitude in the SDSS filter.

Once obtained the final magnitude values, it was possible to compare them with PS1, SDSS and DECaLS dataset. The variability amplitude was found as:

$$\Delta m = m_{survey} - m_{Loiano} \quad (3.2)$$

And the associated error was:

$$err_{|\Delta m|} = \sqrt{err_{survey}^2 + err_{Loiano}^2} \quad (3.3)$$

The significance (in  $\sigma$ ) was derived from:

$$S = \frac{|\Delta m|}{err_{|\Delta m|}} \quad (3.4)$$

The rest frame time lag was computed as:

$$\Delta T_{RF} = \frac{MJD_{Loiano} - MJD_{survey}}{(1 + z)} \quad (3.5)$$

## 3.5 Results

All the results of the analysis are summarised in table 3.2, where are reported the properties of quasars (magnitude, variability amplitude, significance and time intervals) relevant to the comparison of Loiano magnitudes with PS1 and SDSS ones.

Target	redshift	$z_{M_L}$	$z_{M_S}$	$z_{M_P}$	$ \Delta M_{S-L} $	$\sigma$	$\Delta T_{RF(L-S)}$	$ \Delta M_{P-L} $	$\sigma$	$\Delta T_{RF(L-P)}$
J0100+2802	6.326	$18.486 \pm 0.018$	$18.44 \pm 0.03$	$18.46 \pm 0.01$	$0.04 \pm 0.03$	1.31	502	$0.02 \pm 0.01$	1.16	344
J0439+1634	6.5	$18.708 \pm 0.021$	-	$18.77 \pm 0.05$	-	-	-	$0.06 \pm 0.05$	1.22	390
J0439+1634	6.5	$18.837 \pm 0.037$	-	$18.77 \pm 0.05$	-	-	-	$0.07 \pm 0.06$	1.12	390
J0439+1634	6.5	$18.884 \pm 0.019$	-	$18.77 \pm 0.05$	-	-	-	$0.11 \pm 0.05$	2.27	389
P071-02	5.69	$19.219 \pm 0.048$	-	$19.30 \pm 0.02$	-	-	-	$0.08 \pm 0.05$	1.49	430
P108+08	5.92	$19.523 \pm 0.04$	-	$19.39 \pm 0.02$	-	-	-	$0.13 \pm 0.04$	2.94	390
P108+08	5.92	$19.548 \pm 0.051$	-	$19.39 \pm 0.02$	-	-	-	$0.15 \pm 0.05$	2.85	390
J0818+1722	6.02	$19.420 \pm 0.04$	$19.66 \pm 0.09$	$19.50 \pm 0.02$	$0.24 \pm 0.09$	2.43	790	$0.09 \pm 0.05$	1.92	395
J0818+1722	6.02	$19.647 \pm 0.046$	$19.66 \pm 0.09$	$19.50 \pm 0.02$	$0.013 \pm 0.1$	0.12	790	$0.13 \pm 0.05$	2.67	395
J0836+0054	5.81	$19.100 \pm 0.041$	$18.71 \pm 0.04$	$18.82 \pm 0.01$	$0.39 \pm 0.05$	6.8	1070	$0.28 \pm 0.04$	6.4	420
J1016+2541	5.64	$18.798 \pm 0.017$	$19.02 \pm 0.05$	$18.95 \pm 0.01$	$0.222 \pm 0.05$	4.20	834	$0.15 \pm 0.02$	8.18	407
J1044-0125	5.785	$19.252 \pm 0.082$	$19.08 \pm 0.07$	$19.36 \pm 0.01$	$0.172 \pm 0.11$	1.59	1075	$0.10 \pm 0.08$	1.29	429
J1137+3549	6.03	$19.523 \pm 0.031$	$19.53 \pm 0.08$	$19.32 \pm 0.02$	$0.007 \pm 0.08$	0.08	833	$0.20 \pm 0.03$	5.06	404
J1137+3549	6.03	$19.518 \pm 0.026$	$19.53 \pm 0.08$	$19.32 \pm 0.02$	$0.012 \pm 0.08$	0.14	783	$0.19 \pm 0.03$	5.47	353
J1148+5251	6.419	$20.269 \pm 0.059$	$19.98 \pm 0.1$	$20.10 \pm 0.04$	$0.289 \pm 0.11$	2.52	893	$0.17 \pm 0.06$	2.52	366
J1335-0328	5.67	$18.734 \pm 0.059$	$18.97 \pm 0.04$	$18.87 \pm 0.02$	$0.235 \pm 0.05$	4.33	1026	$0.13 \pm 0.04$	3.23	430
P323+12	6.588	$20.249 \pm 0.206$	$20.59 \pm 0.24$	$19.09 \pm 0.19$	$0.979 \pm 0.31$	0.3	859	$1.39 \pm 0.28$	5.03	358
J2310+1855	6.003	$19.639 \pm 0.052$	$19.49 \pm 0.1$	$19.46 \pm 0.03$	$0.179 \pm 0.11$	1.58	560	$0.18 \pm 0.05$	3.02	252

Table 3.2: Results table, (1) Target name. (2) Redshift. (3) Magnitude obtained with Loiano telescope. (4) Magnitude obtained with SDSS. (5) Magnitude obtained with PS1. (6) Variability value computed from the difference between SDSS magnitude and Loiano. (7) Significance in  $\sigma$ . (8) Time intervals between observations in rest-frame days. (9) Variability value computed from the difference between PS1 and Loiano. (10) Significance in  $\sigma$ . (11) Time intervals between observations in rest-frame days.

The same quantities are reported in table 3.3 for the comparison between DECaLS and Loiano. This second analysis confirms the results reported for the majority of the cases, except for 3 sources that appear in contrast with their counterparts in table 3.2.

Source	$z_{decam}$	$z_{e_{decam}}$	$ \Delta m $	Significance	$\Delta T$
J0100+2802	18.023	0.002	$0.462 \pm 0.018$	25.502	54.98
P071-02	19.173	0.005	$0.045 \pm 0.048$	0.933	84.08
J0818+1722	19.343	0.007	$0.077 \pm 0.04$	1.901	58.44
J0818+1722	19.343	0.007	$0.304 \pm 0.046$	6.541	58.61
J0836+0054	18.993	0.005	$0.107 \pm 0.041$	2.586	124.91
J1016+2541	18.980	0.005	$0.182 \pm 0.0178$	10.251	191.27
J1044-0125	19.324	0.006	$0.072 \pm 0.082$	0.875	125.63
J1137+3549	19.255	0.005	$0.267 \pm 0.031$	8.483	163.46
J1137+3549	19.255	0.005	$0.262 \pm 0.026$	9.859	104.93
J1148+5251	19.560	0.006	$0.708 \pm 0.056$	12.560	116.78
J1335-0328	18.868	0.004	$0.134 \pm 0.037$	3.609	227.51
P323+12	20.040	0.012	$0.451 \pm 0.206$	2.187	6.87
J2310+1855	19.231	0.004	$0.407 \pm 0.052$	7.807	57.58

Table 3.3: (1) Target name. (2) Magnitude. (3) Error on mperformed betweenagnitude. (4) Variability. (5) Error on variability. (6) Significance. (7) Time interval between observations in days

Figures 3.6-3.7-3.8 show the light curve of the 13 sources, with all the photometrical points available and reported at the dates of the observation, in the observer's frame. In particular: figure 3.6 reports that for 4 sources seem to be a consistent trend in the increasing or decreasing of the observed flux in comparison with SDSS, Pan-STARRS and DECaLS data with a significance greater than  $3\sigma$ ; while in fig.3.7 6 objects do not show evidence of variability, with  $\sigma < 3$ ; as figure 3.8 shows, the 3 remaining quasars have an uncertain behavior as they vary significantly in PS1 and DECaLS but not in SDSS.

Another interesting quantity, supporting that these work could be done only after enough time from PS1, SDSS and DECaLS surveys, is the  $\Delta M / \Delta T_{Rest-frame}$  ratio, shown in table 3.4.

The histogram in fig.3.9 shows the variability amplitude trend of the sample of observed quasars from the other three surveys. Its peak correspond to a 0.1-0.2 range.

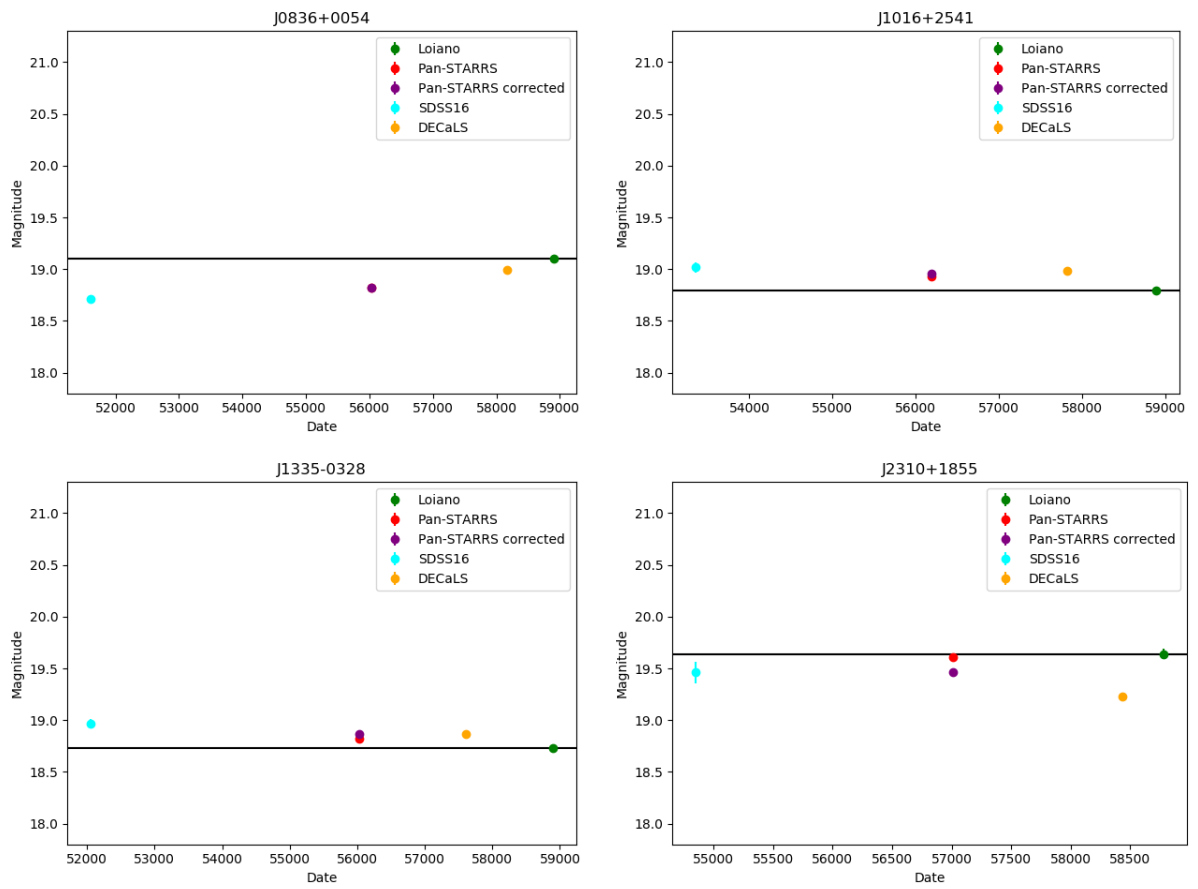


Figure 3.6: Light curves in the observer's frame of variable sources: J0836+0054 (top left), J1016+2541 (top right), J1335-0328 (bottom left), J2310+1855 (bottom right)

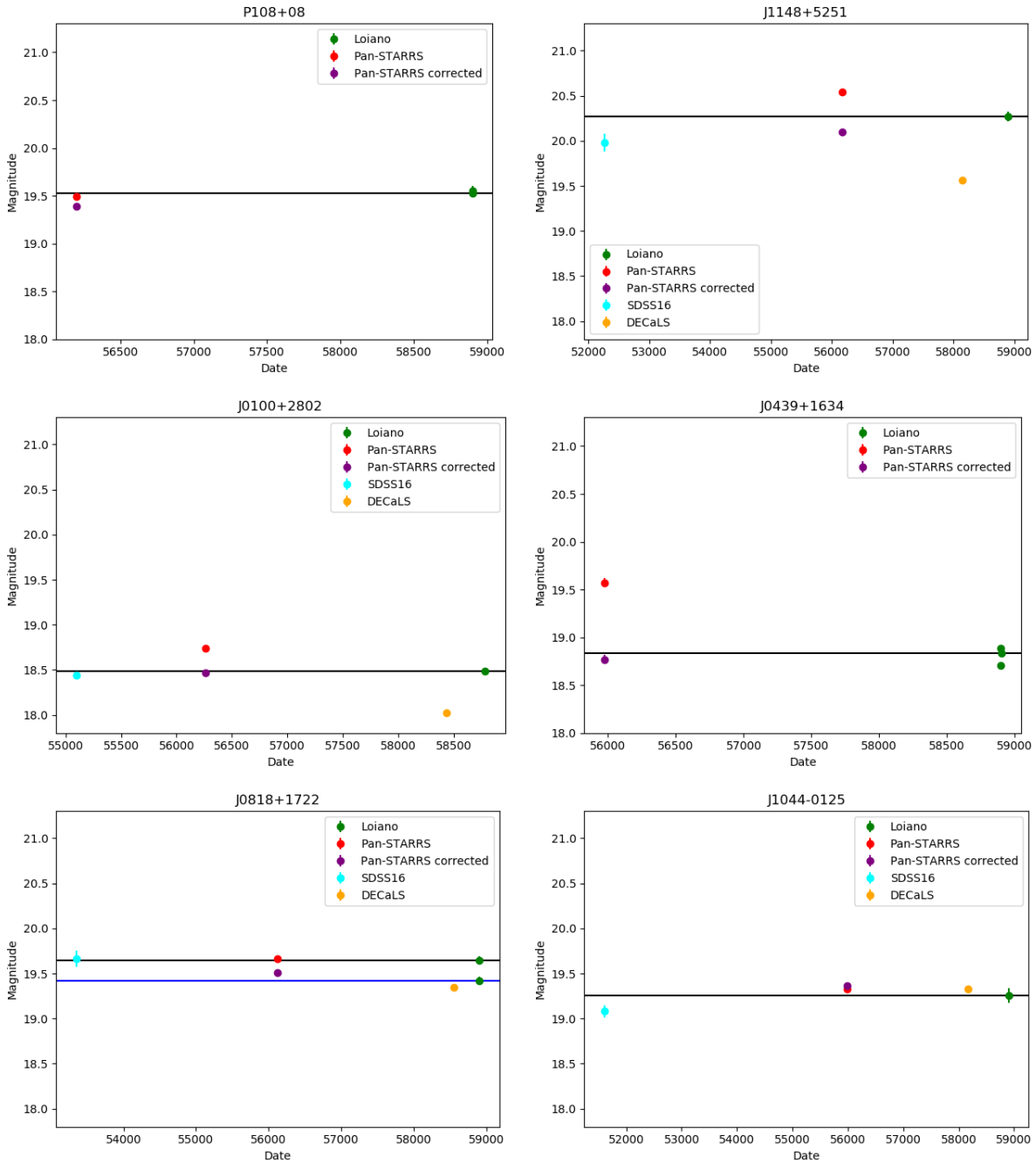


Figure 3.7: Light curves in the observer's frame of non variable sources: P108+08 (top left), J1148+5251 (top right), J0100+2802 (central left), J0439+1634 (central right), J0818+1722 (bottom left), J044-0125 (bottom right).

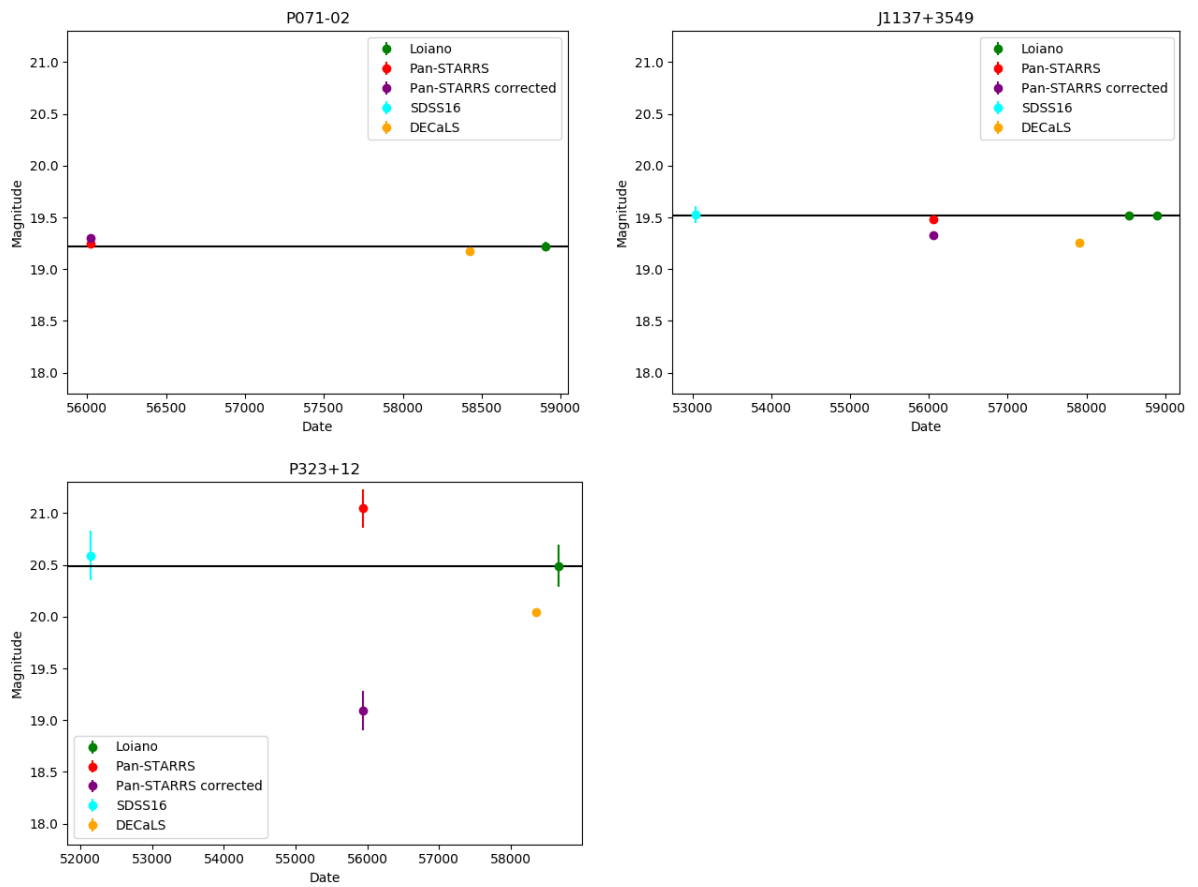


Figure 3.8: Light curves in the observer's frame of variable sources in PS1 but not in SDSS: P071-02 (top left), J1137+3549 (top right), P323+12 (bottom)

Target	$\Delta M_{L-P}/\Delta T_{L-P}$	$\Delta M_{L-S}/\Delta T_{L-S}$	$\Delta M_{L-D}/\Delta T_{L-D}$
J0100+2808	0.02	0.03	3.07
J0439+1634	0.06	-	-
J0439+1634	0.06	-	-
J0439+1634	0.11	-	-
P071-02	0.07	-	0.19
P108+08	0.12	-	-
P108+08	0.14	-	-
J0818+1722	0.08	0.11	0.48
J0818+1722	0.13	0.01	1.89
J0836+0054	0.24	0.13	0.31
J1016+2541	0.14	0.09	0.34
J1044-0125	0.09	0.06	0.21
J1137+3549	0.17	0.01	0.59
J1137+3549	0.19	0.01	0.91
J1148+5251	0.17	0.11	2.21
J1335-0328	0.11	0.08	0.21
P323+12	1.42	0.04	3.51
J2310+1855	0.25	0.12	2.58

Table 3.4: (1) Target. (2), (3) and (4) Magnitude-to-time interval ratio in unity of mag/year for PS1 (P), SDSS (S) and DECaLS (D)

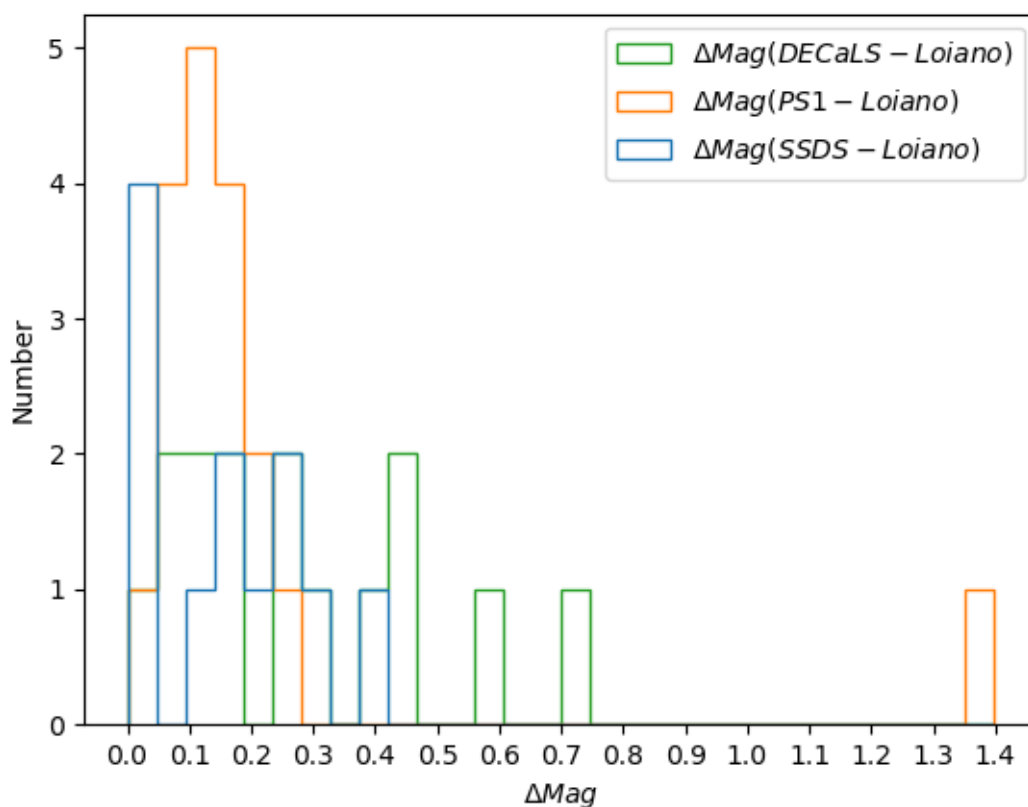


Figure 3.9: Variability distribution Histogram showing the number of variable sources in function of variability amplitude, from 3 different surveys: DECaLS (green), PS1 (orange), SDSS (blue).



# Chapter 4

## Discussion and conclusions

The active galactic nuclei produce enormous luminosities in extremely compact volumes. Quasars are the most powerful type of AGN and, because of their high luminosities they can be detected at wide distances.

While matter from the accretion disk falls onto the black hole, the conversion of the gravitational potential energy of the mass in radiation make them visible (Lynden-Bell, 1969).

Programs of monitoring AGN variability are fundamental to understand the nature of inner region of quasars in various scales and also provide a better knowledge of their role in the evolution of AGN and galaxies.

Variability in the order of 10-20% of flux is an hallmark of accreting supermassive black holes across a broad range of wavelengths, timescales, and accretion states (Mushotzky et al., 1993; Ulrich et al., 1997; Peterson, 2001). The physical cause of quasar variability is still unclear, but since the optical continuum seems to be dominated by emission from the accretion disk, some studies have suggested that changes in the global accretion rate in the disk may be able to produce such effects.

The presence of already formed SMBHs at the dawn of cosmic times, that have also several analogies with local AGN, challenges models of their formation and growth.

Has variability similar behavior both in high and low redshift quasars?

In this work I led a variability study of high redshift quasars in the optical/UV band. I based this analysis on a sample observed in a dedicated follow-up campaign at the Cassini Telescope in Loiano.

After data reduction and analysis of a sample of 13 quasars, I carried out a comparison between my data and those obtained from the SDSS, PS1 and DECaLS catalogs, resulting in a baseline up to 15 years in the observer's frame. The time lag between my observations and the survey detection correspond to a rest frame interval of about 1-2 years, suggesting that this effects comes from the accretion disk. Once I estimated the variability value and its relative error from each target, I derive the significance. The main aim of this

work is to search for significant flux variations in at least a sub-sample of the targeted sources, if founded, they would be the first time in the optical/UV band at such high redshift.

Quasars in this sample average vary of 0.1-0.2 magnitudes in a timescale rest-frame of several years, in agreement with the value that can be found for lower redshift sample (Kelly et al., 2009; Kozłowski et al., 2010; MacLeod et al., 2010; Schmidt et al., 2010; Butler & Bloom, 2011; Kim et al., 2011; MacLeod et al., 2011; Ruan et al., 2012; Andrae et al., 2013; Zu et al., 2013).

It can be inferred that, like other proprieties, variability does not show an evolution from early ages to the present. Leading to the conclusion that the mechanism responsible of the variation is already in place even less than one billion years after the big bang.

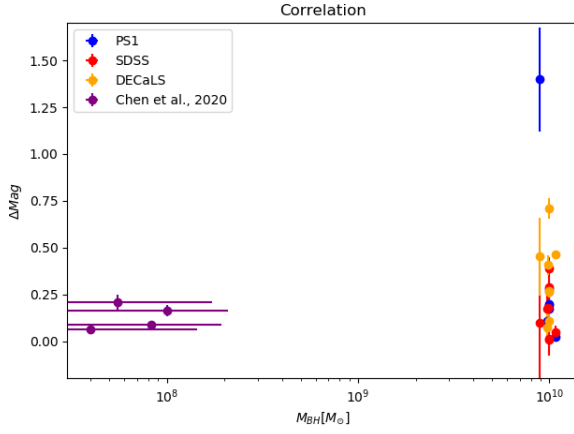
Putting  $3\sigma$  as threshold, the result (showed also in tab.3.2 and figg.3.6, 3.7 and 3.8) is that:

- 4 quasars are variable (J0836+0054, J1016+2541, J1335-0328, J2310+1855). These are the first variable quasars in the optical band at redshift  $z > 5.5$ ;
- 6 quasars are not variable (J0100+2802, J0439+1634, J0818+1722, J044-0125, P108+08 and J1148+5251).;
- 3 quasar shows an uncertain behaviour between observations (P071-02, J1137+3549 and P323+12) because they seems to vary from PS1 and DECaLS catalog but not from SDSS. These are doubtful cases as it could be true variability, in which the object has been decreasing but is now brighter or suspected cases for which the apparent variability is due to an erroneous correction for the difference of filters.
- there is an there is an apparent inconsistency between the variabilities in J1148+5251, J0100+2808 and J0818+1722, which could be real (a short-term variability) or linked to calibrations and systematics errors, and that needs further investigations.

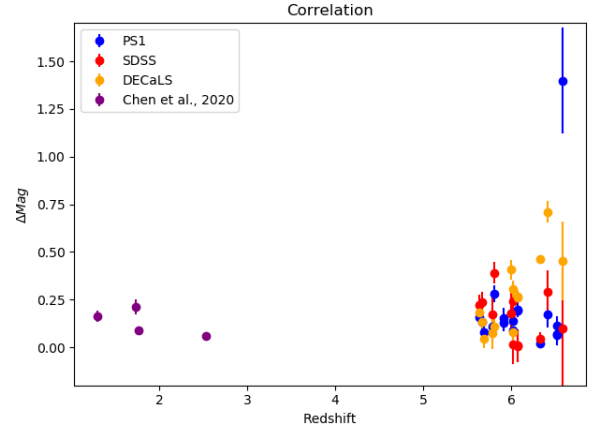
The dependence of flux variability on AGN properties can be analyzed in order to find any trend that link their features. Some of these correlations were placed in a more general context in fig.4.1, including information found from four lower redshift ( $1 < z < 2$ ) quasars from Chen et al., 2020. In fig.4.1 variability is compared with BH mass (fig.4.1a), redshift (fig.4.1b), luminosity (4.1c) and rest frame time interval between observations (fig.4.1d). Similar behavior to lower redshift studies could be find, for example, comparing fig.4.1 with fig.1.4.

Various trends were observed between optical variability amplitude and other proprieties of AGN, such as black hole mass, time interval and luminosity:

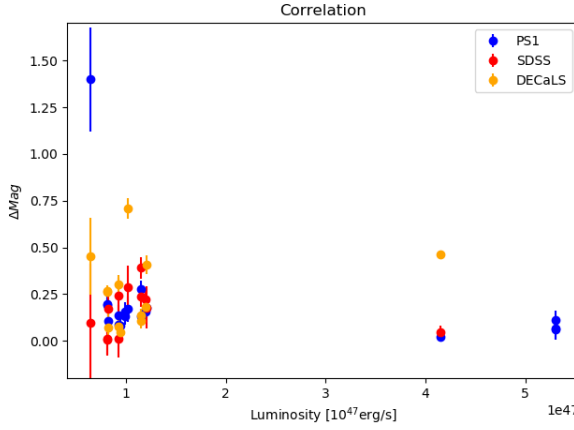
- variability versus BH mass seems to have not any trend. An explanation could be that large masses limit the variability, as the emitting system is larger. Furthermore, Wilhite et al., 2008 suggest that black hole mass is more evident at longer



(a) Variability vs BH mass



(b) Variability vs redshifts



(c) Variability vs UV luminosity

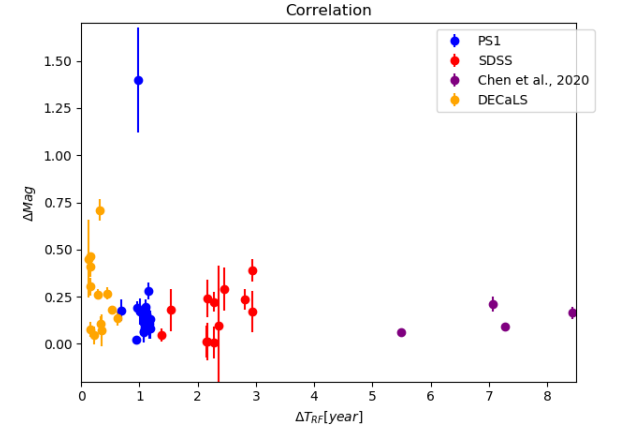
(d) Variability vs  $\Delta t_{Rest-frame}$ 

Figure 4.1: Dependence between flux variability and (4.1a) BH mass, (4.1b) redshift, luminosity (4.1c) and (4.1d) rest frame time interval between observations, extended with data from Chan et., 2020 when available.

time-lags, one reason why the relation is still contradictory could be that the time interval where it is most expected has not yet been properly sampled;

- there is no convincing detection of a correlation between amplitude and redshift. In analogy with similarities between high redshift quasars and lower ones, these effect of redshift could be linked to the lack of evolution of these object proprieties;
- variability indicates a slight anti-correlation with luminosity. The negative trend with luminosity confirm what was already established (Wilhite et al, 2008; Bauer et al., 2009; Macleod et al., 2010);
- variability versus time lag shows a positive correlation. This correlation with time interval proves that stochastic process are cause of changing in AGN fluxes.

These results are in line with low redshift studies (Hook et al., 1994; Garcia et al., 1999; Vanden Berk et al., 2004; Wilhite et al., 2008; Bauer et al., 2009; Kelly et al., 2009; MacLeod et al., 2010; Zuo et al., 2012).

Further investigation are needed in a multiwavelength approach and wider range of timescales for a better understanding of the physical mechanisms related to AGN.

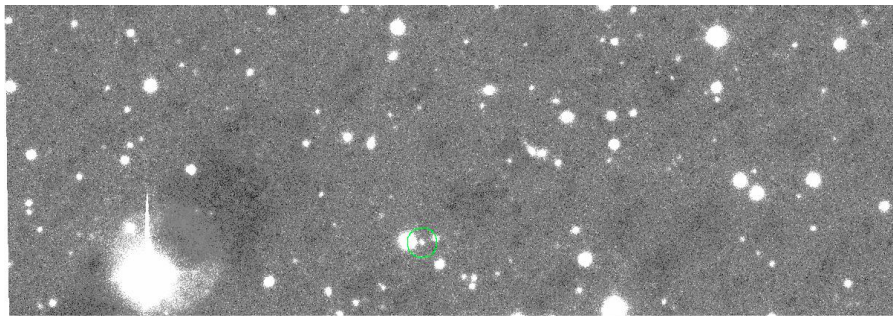
It was proposed, using the 152 cm telescope in Loiano, to continue for several year a long campaign of monitoring of these sources in order to sample the (rest-frame monthly) variability of the quasars at the dawn of cosmic time. A coming facilities to study variability proprieties are Large Synoptic Survey Telescope(LSST/Vera Rubin; Ivezić et al., 2019) and 4MOST. What future deserves to AGN studies is an increasingly larger and deeper sky surveys at all wavelengths, together with the launch of space telescopes and the advent of larger ground-based telescopes. On the theoretical side, increasingly sophisticated and complex simulations will infer new information about AGN.

Variability studies may result as useful probes for such kind of researches.

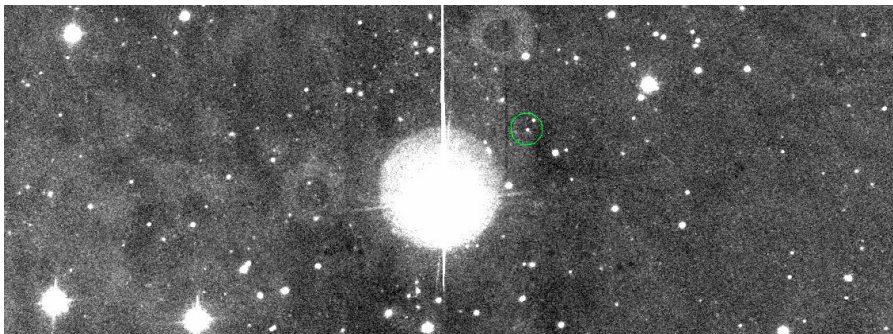
# Appendix A

## Scientific images

I provide all scientific images produced after data reduction.

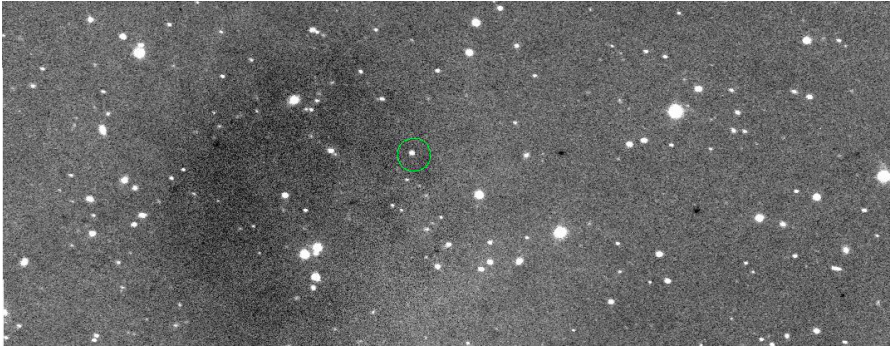


(a) J1335-0328

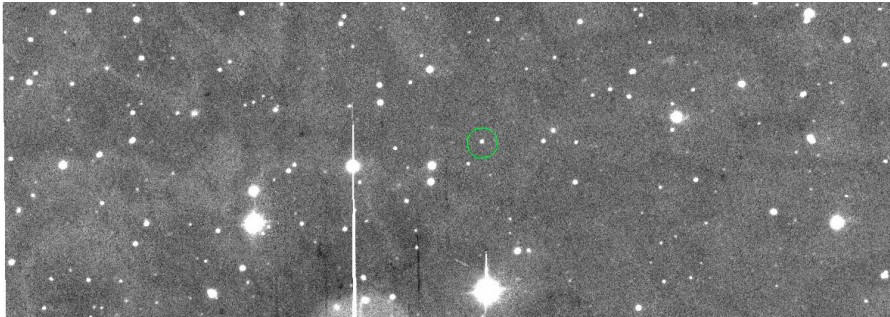


(b) J2310+1855

Figure A.1: Images of the sample quasars: J1335-0328 (left), J2310+1855 (right)



(a) J0100+2802



(b) J0439+1634

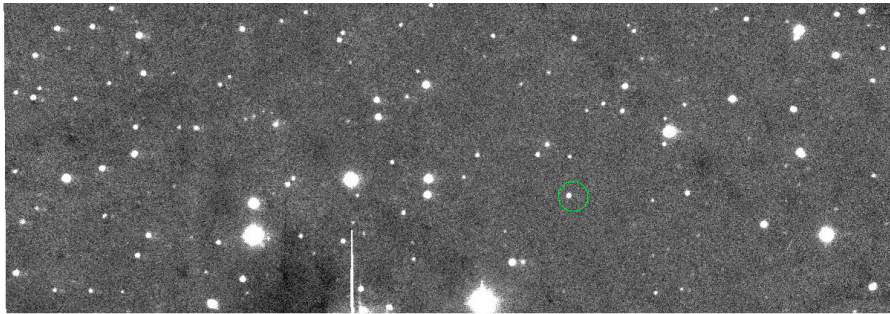
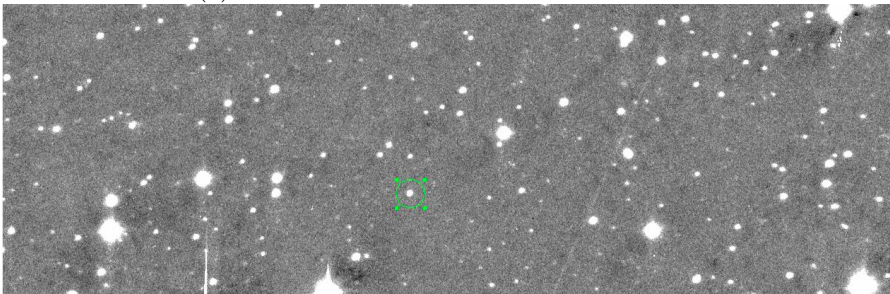
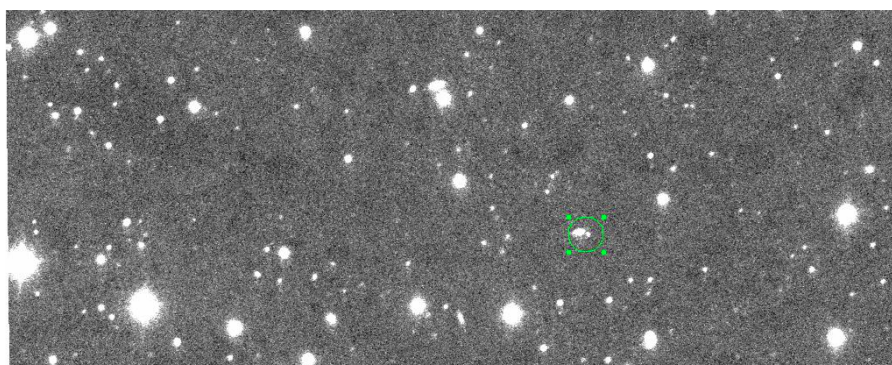
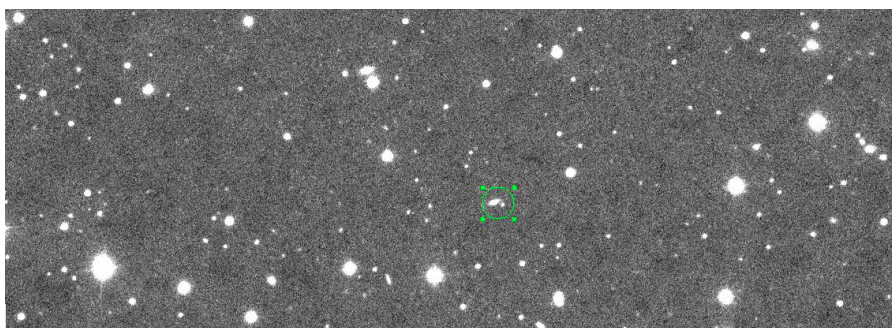
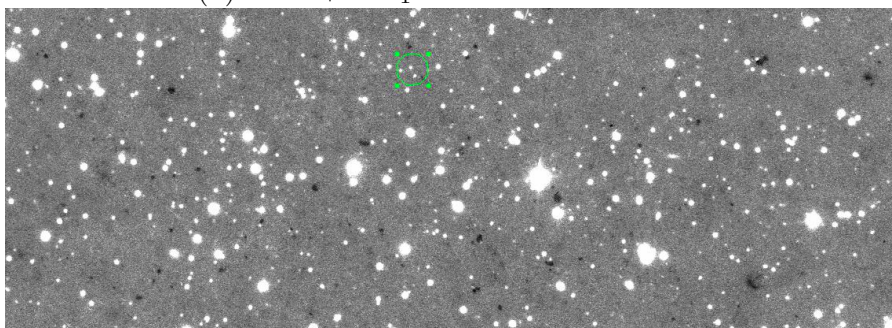
(c) J0439+1634<sub>1</sub>(d) J0439+1634<sub>2</sub>

Figure A.2: Images of the sample quasars: J0100+2802 (top left), J0439+1634 (top right, bottom left, bottom right)



(a) J0818+1722

(b) J0818+1722<sub>1</sub>

(c) P108+08

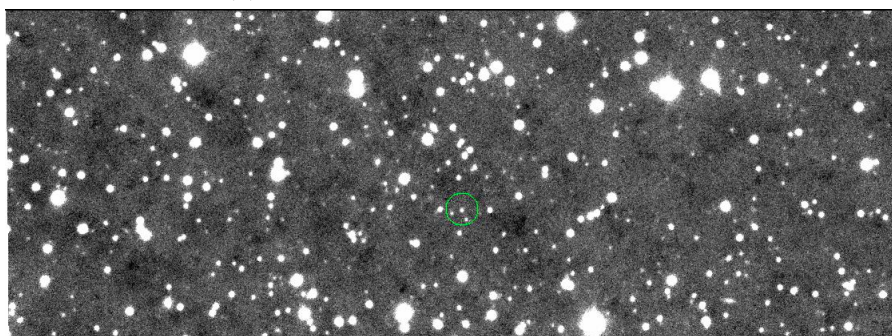
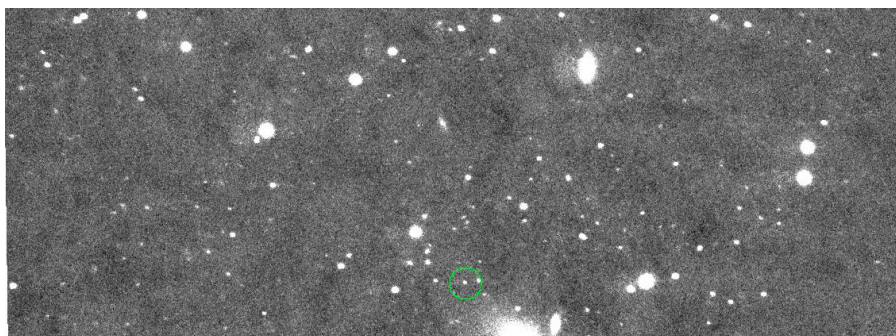
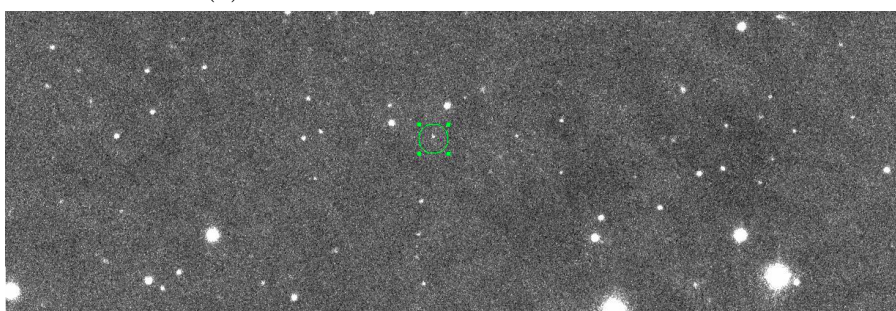
(d) P108+08<sub>1</sub>

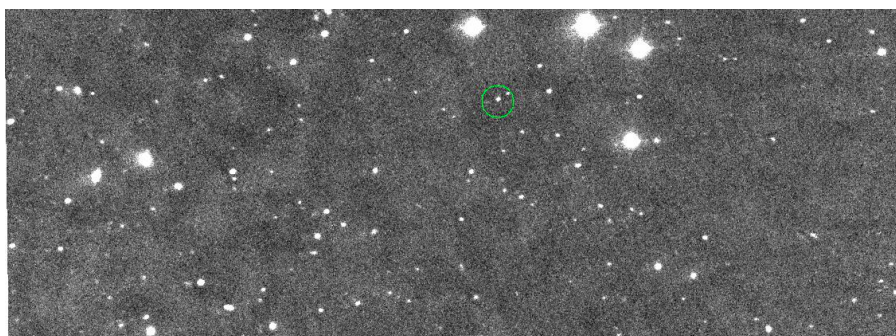
Figure A.3: Images of the sample quasars: J0818+1722 (top), P108+08 (bottom)



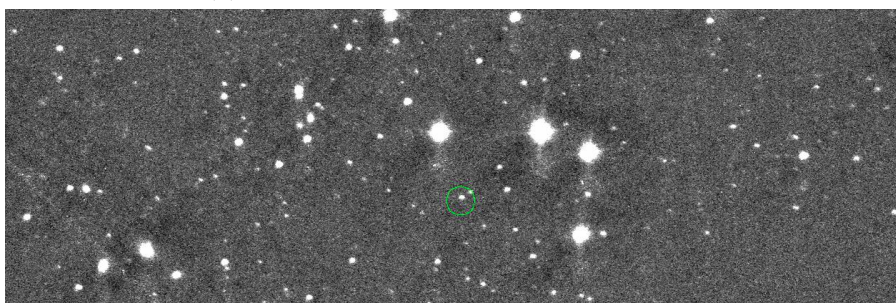
(a) J1148+5251



(b) J1044-0125

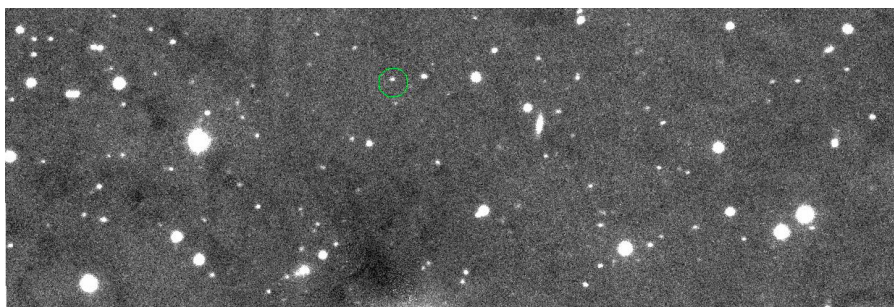


(c) J1137+3549

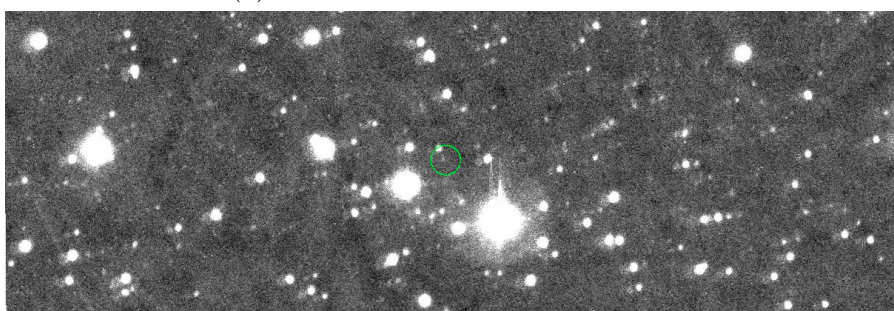


(d) J1137+3549

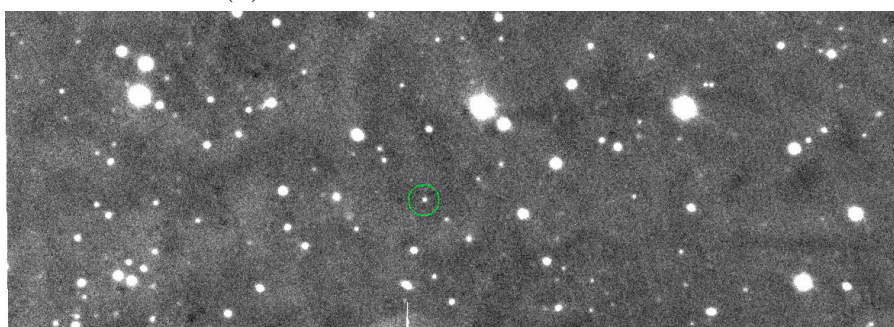
Figure A.4: Images of the sample quasars: J1148+5251 (top left), J1044-0125 (top right), J1137+3549 (bottom panels)



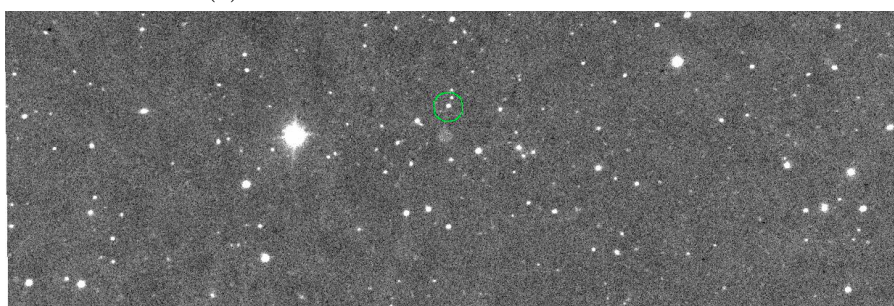
(a) P071-02



(b) P323+12



(c) J0836+0054



(d) J1016+2541

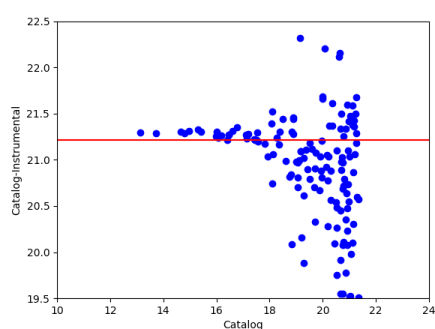
Figure A.5: Images of the sample quasars: P071-02 (top left), P323+12 (top right), J0836+0054 (bottom left), J1016+2541 (bottom right)



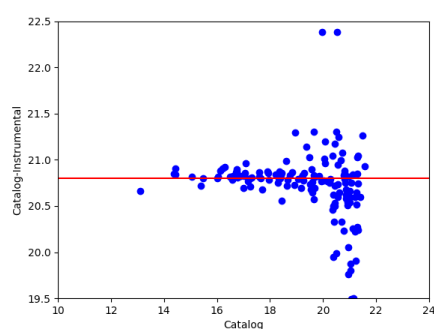
# Appendix B

## Zero point

In order to compare magnitudes from different observations we need to calibrate them, that means to put the magnitudes in a given photometric system. In astronomy, the Zero Point in a photometric system is defined as the magnitude of an object that produces 1 count per second on the detector. The zero point is used to calibrate a system to the standard magnitude system, as the flux detected from astronomical objects will vary from detector to detector. As it was said before in section 3.4, once obtained the instrumental magnitude of the field stars from qphot, I subtracted my data from the corresponding values reported in the PS1 database. Then, I computed the median value of these differences and the obtained value is the zero point correction needed to calibrate my sample magnitude. The scatter of points from the median value in fig.B.1-B.2-B.3 is due to outliers.

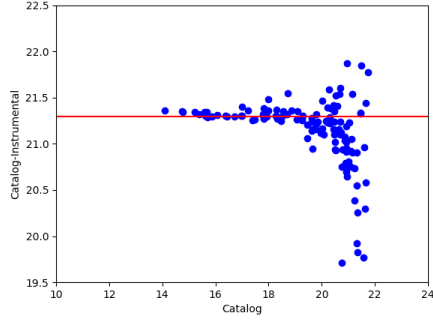


(a) J1335-0328

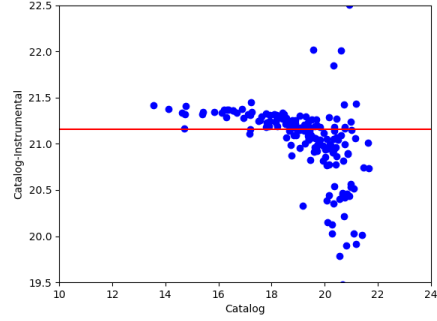


(b) J2310+1855

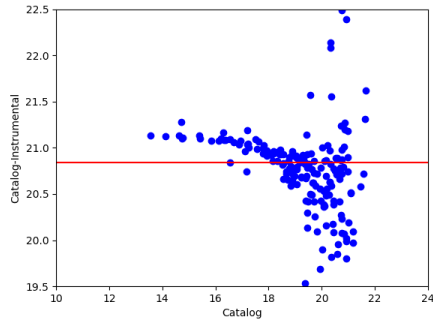
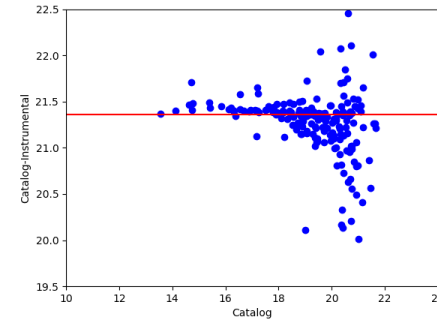
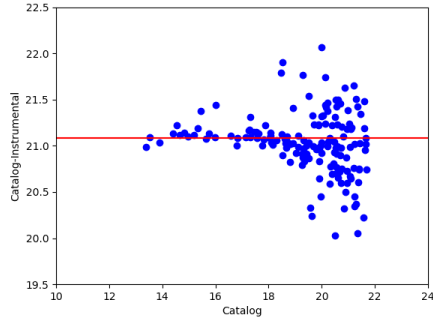
Figure B.1: Zero points of the sample quasars: J1335-0328 (left), 2310+1855 (right)



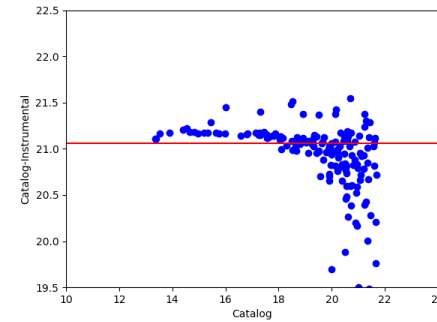
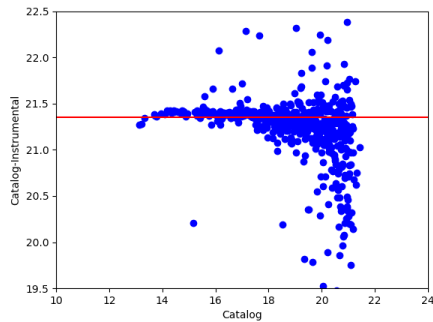
(a) J0100+2802



(b) J0439+1634

(c) J0439+1634<sub>1</sub>(d) J0439+1634<sub>2</sub>

(e) J0818+1722

(f) J0818+1722<sub>1</sub>

(g) P108+08

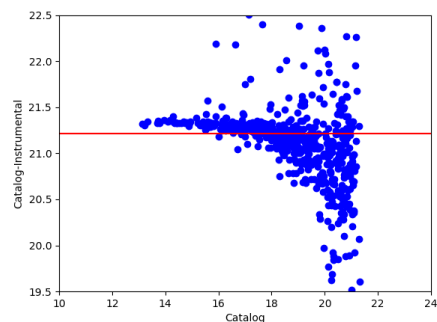
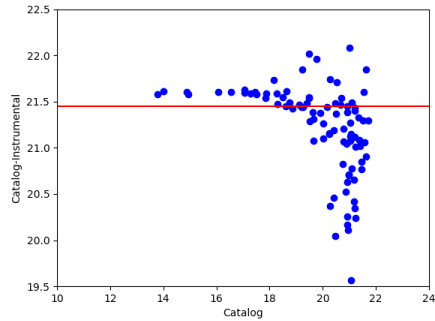
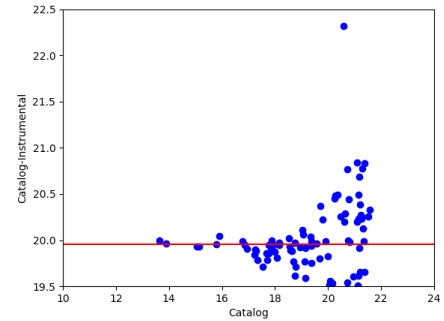
(h) P108+08<sub>1</sub>

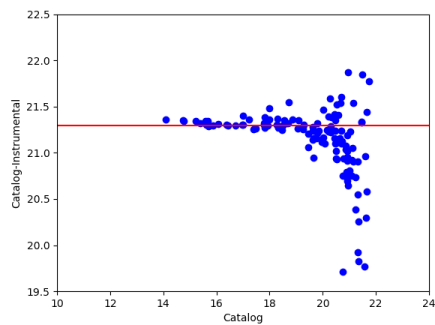
Figure B.2: Zero points of the sample quasars: J0100+2802 (top left), J0439+1634 (top right and second row), J0818+1722 (third row), P108+08 (bottom)



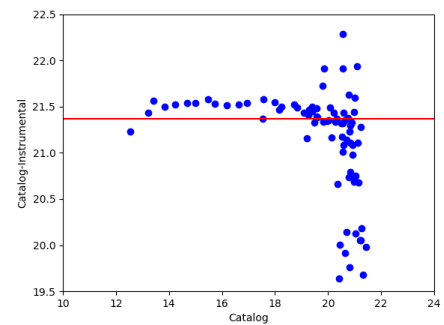
(a) J1148+5251



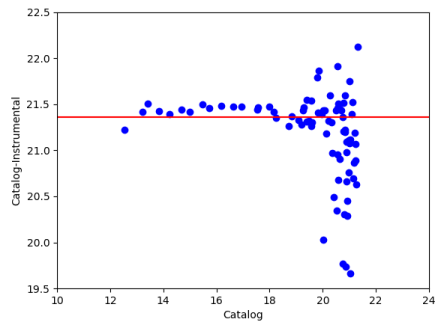
(b) J1044-0125



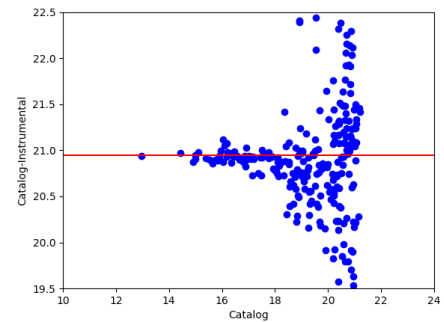
(c) P071-02



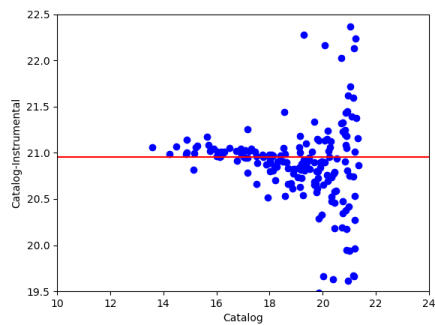
(d) J1137+3549



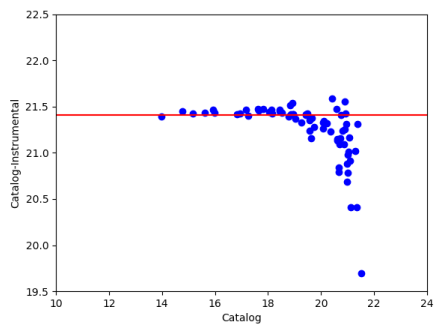
(e) J1137+3549



(f) P323+12



(g) J0836+0054



(h) J1016+2541

Figure B.3: Zero points of the sample quasars: J1148+5251 (top left), J1044-0125 (top right), P071-02 (second row left), J1137+3549 (second row right, third row left), P323+12 (third row right), J0836+0054 (bottom left), J1016+2541 (bottom right)



# Bibliography

(n.d.).

Banados, E. (2015), The discovery and characterization of the most distant quasars, PhD thesis.

Banados E., B. P. Venemans, R. Decarli, E. P. Farina, C. Mazzucchelli, F. Walter, X. Fan, D. Stern, E. Schlafly, K.C. Chambers, H-W. Rix, L. Jiang, I. McGreer, R. Simcoe, F. Wang, J. Yang, E. Morganson, G. De Rosa, J. Greiner, M. Baloković, W. S. Burgett, T. Cooper, P. W. Draper, H. Flewelling, K. W. Hodapp, H. D. Jun, N. Kaiser, R. P. Kudritzki, E. A. Magnier, N. Metcalfe, D. Miller, J.-T. Schindler, J. L. Tonry, R. J. Wainscoat, C. Waters, Q. Yang (2016), ‘THE PAN-STARRS1 DISTANT  $z > 5.6$  QUASAR SURVEY: MORE THAN 100 QUASARS WITHIN THE FIRST GYR OF THE UNIVERSE’, *apj supplement* .

Banados Eduardo, Venemans Bram, Walter Fabian, Kurk Jaron, Overzier Roderik and Ouchi Masami (2013), ‘THE GALAXY ENVIRONMENT OF A QSO AT  $Z \sim 5.7$ ’, *apj* .

Begelman Mitchell C. , Volonteri Marta (2016), ‘Hyperaccreting black holes in galactic nuclei’, *mnras* .

Bhoomika, C. S. Stalin, S. Sahayanathan, Suvendu Rakshit, Amit Kumar Mandal (2018), ‘Temporal correlation between the optical and  $\gamma$ -ray flux variations in the blazar 3C 454.3’, *mnras* .

Chambers, K. C.; Magnier, E. A.; Metcalfe, N.; Flewelling, H. A.; Huber, M. E.; Waters, C. Z.; Denneau, L.; Draper, P. W.; Farrow, D.; Finkbeiner, D. P.; Holmberg, C.; Koppenhoefer, J.; Price, P. A.; Rest, A.; Saglia, R. P.; Schlafly, E. F.; Smartt, S. J.; Sweeney, W.; Wainscoat, R. J.; Burgett, W. S. Chastel, S.; Grav, T.; Heasley, J. N.; Hodapp, K. W.; Jedicke, R.; Kaiser, N.; Kudritzki, R. -P.; Luppino, G. A.; Lupton, R. H.; Monet, D. G.; Morgan, J. S.; Onaka, P. M.; Shiao, B.; Stubbs, C. W.; Tonry, J. L.; White, R.; Bañados, E.; Bell, E. F.; Bender, R.; Bernard, E. J.; Boegner, M.; Boffi, F.; Botticella, M. T.; Calamida, A.; Casertano, S.; Chen, W. -P.; Chen, X.; Cole, S.;

- Deacon, N.; Frenk, C.; Fitzsimmons, A.; Gezari, S.; Gibbs, V.; Goessl, C.; Goggia, T.; Gourgue, R.; Goldman, B.; Grant, P.; Grebel, E. K.; Hambly, N. C.; Hasinger, G.; Heavens, A. F.; Heckman, T. M.; Henderson, R.; Henning, T.; Holman, M.; Hopp, U.; Ip, W. -H.; Isani, S.; Jackson, M.; Keyes, C. D.; Koekemoer, A. M.; Kotak, R.; Le, D.; Liska, D.; Long, K. S.; Lucey, J. R.; Liu, M.; Martin, N. F.; Masci, G.; McLean, B.; Mindel, E.; Misra, P.; Morganson, E.; Murphy, D. N. A.; Obaika, A.; Narayan, G.; Nieto-Santisteban, M. A.; Norberg, P.; Peacock, J. A.; Pier, E. A.; Postman, M.; Primak, N.; Rae, C.; Rai, A.; Riess, A.; Riffeser, A.; Rix, H. W.; Röser, S.; Russel, R.; Rutz, L.; Schilbach, E.; Schultz, A. S. B.; Scolnic, D.; Strolger, L.; Szalay, A.; Seitz, S.; Small, E.; Smith, K. W.; Soderblom, D. R.; Taylor, P.; Thomson, R.; Taylor, A. N.; Thakar, A. R.; Thiel, J.; Thilker, D.; Unger, D.; Urata, Y.; Valenti, J.; Wagner, J.; Walder, T.; Walter, F.; Watters, S. P.; Werner, S.; Wood-Vasey, W. M.; Wyse, R. (2016), ‘The Pan-STARRS1 Surveys’.
- Chen Yu-Ching, Xin Liu, Wei-Ting Liao, A. Miguel Holgado, Hengxiao Guo, Robert A. Gruendl, Eric Morganson, Yue Shen, Kaiwen Zhang, Tim M. C. Abbott, Michel Agüena, Sahar Allam, Santiago Avila, Emmanuel Bertin, Sunayana Bhargava, David Brooks, David L. Burke, Aurelio Carnero Rosell, Daniela Carollo, Matias Carrasco Kind, Jorge Carretero, Matteo Costanzi, Luiz N. da Costa, Tamara M. Davis, Juan De Vicente, Shantanu Desai, H. Thomas Diehl, Peter Doel, Spencer Everett, Brenna Flaugher, Douglas Friedel, Joshua Frieman, Juan Garcia-Bellido, Enrique Gaztanaga, Karl Glazebrook, Daniel Gruen, Gaston Gutierrez, Samuel R. Hinton, Devon L. Hollowood, David J. James, Alex G. Kim, Kyler Kuehn, Nikolay Kuropatkin, Geraint F. Lewis, Christopher Lidman, Marcos Lima, Marcio A. G. Maia, Marisa March, Jennifer L. Marshall, Felipe Menanteau, Ramon Miquel, Antonella Palmese, Francisco Paz-Chinchón, Andrés A. Plazas, Eusebio Sanchez, Michael Schubnell, Santiago Serano, Ignacio Sevilla-Noarbe, Mathew Smith, Eric Suchyta, Molly E. C. Swanson, Gregory Tarle, Brad E. Tucker, Tamas Norbert Varga, and Alistair R. Walker (2020), ‘Candidate Periodically Variable Quasars from the Dark Energy Survey and the Sloan Digital Sky Survey’, *mnr* (1-21).
- Cid Fernandes R., Sodr e L. Jr., Vieira Da Silva L. Jr. (2000), ‘Quasar variability in the framework of poissonian models’, *apj* **554**, 123–141.
- Cimatti Andrea, Zamorani Giovanni, Marano Bruno (1993), ‘Optical variability of faint quasars’, *mnr* **263**, 236–246.
- Costa Tiago, Rosdahl Joakim & Kimm Taysun (2019), ‘The hidden satellites of massive galaxies and quasars at high-redshift’, *mnr* (1-7).
- De Vries W. H., Becker R. H., White R. L. (2003), ‘Long-term variability of sloan digital sky survey quasars’, *apj* **126**, 1217–1226.

- Decarli R., Walter F., Venemans B.P., Bañados E., Bertoldi F., Carilli C., Fan X., Farina E.P., Mazzucchelli C., Riechers D., Rix H.-W., Strauss M.A., Wang R., Yang Y. (n.d.), ‘Rapidly star-forming galaxies adjacent to quasars at redshifts exceeding 6’.
- Dubois Yohan, Gavazzi Raphaël, Peirani Sébastien and Silk Joseph (2013), ‘AGN-driven quenching of star formation: morphological and dynamical implications for early-type galaxies’, *mnras* .
- Fan, X. (2006), ‘Evolution of high-redshift quasars’, *Mem. S.A.It.* **77**(635).
- Fan X., Wang F., Yang J., Keeton C.R., Yue M., Zabludoff, Bian F., Bonaglia M, Georgiev I.Y, Hennawi J. F., Venemans B., Walter F., Ran Wang, Wu X. (2019), ‘The Discovery of a Gravitationally Lensed Quasar at  $z = 6.51$ ’.
- Fan Xiaohui , Michael A. Strauss , Donald P. Schneider , Robert H. Becker , , Richard L. White , Zoltan Haiman , Michael Gregg , Laura Pentericci , Eva K. Grebel , Vijay K. Narayanan , Yeong-Shang Loh , Gordon T. Richards , James E. Gunn , Robert H. Lupton , Gillian R. Knapp , Zeljko Ivezic , W. N. Brandt , Matthew Collinge , Lei Hao , Daniel Harbeck , Francisco Prada , , Joop Schaye , Iskra Strateva , Nadia Zakamska , Scott Anderson . Jon Brinkmann , Neta A. Bahcall Don Q. Lamb , Sadanori Okamura , Alex Szalay , Donald G. York (2003), ‘A Survey of  $z > 5.7$  Quasars in the Sloan Digital Sky Survey II: Discovery of Three Additional Quasars at  $z > 6$ ’, *apj* .
- Fan Xiaohui , Michael A. Strauss, Gordon T. Richards, Joseph F. Hennawi, Robert H. Becker, Richard L. White, Aleksandar M. Diamond-Stanic, Jennifer L. Donley, Linhua Jiang, J. Serena Kim, Marianne Vestergaard, Jason E. Young, James E. Gunn, Robert H. Lupton, Gillian R. Knapp, Donald P. Schneider, W. N. Brandt, Neta A. Bahcall, J.C. Barentine, J. Brinkmann, Howard J. Brewington, Masataka Fukugita, Michael Harvanek, S.J. Kleinman, Jurek Krzesinski, Dan Long, Eric H. Neilsen, Jr. Atsuko Nitta, Stephanie A. Snedden and Wolfgang Voges (2005), ‘A Survey of  $z > 5.7$  Quasars in the Sloan Digital Sky Survey IV: Discovery of Seven Additional Quasars’, *apj* .
- Fan Xiaohui , Michael A. Strauss, Robert H. Becker, Richard L. White, James E. Gunn, Gillian R. Knapp, Gordon T. Richards, Donald P. Schneider, J. Brinkmann and Masataka Fukugita (2006), ‘Constraining the Evolution of the Ionizing Background and the Epoch of Reionization with  $z \sim 6$  Quasars II: A Sample of 19 Quasars’.
- Fan Xiaohui , Richard L. White , Marc Davis , Robert H. Becker , , Michael A. Strauss , Zoltan Haiman , Donald P. Schneider , Michael D. Gregg , , James E. Gunn , Gillian R. Knapp , Robert H. Lupton , John E. Anderson, Jr. , Scott F. Anderson , James Annis , Neta A. Bahcall , William N. Boroski , Robert J. Brunner , Bing Chen , Andrew J. Connolly , Istvan Csabai , Mamoru Doi , Masataka Fukugita , , G. S. Hennessy , Robert B. Hindsley , Takashi Ichikawa , Željko Ivezić , Avery Meiksin , Timothy A.

- McKay , Jeffrey A. Munn , Heidi J. Newberg , Robert Nichol , Sadanori Okamura , Jeffrey R. Pier , Maki Sekiguchi , Kazuhiro Shimasaku , Alexander S. Szalay , Gyula P. Szokoly , Aniruddha R. Thakar , Michael S. Vogeley , Donald G. York (2000), ‘The Discovery of a Luminous  $z = 5.80$  Quasar from the Sloan Digital Sky Survey’.
- Fan Xiaohui, C.L. Carilli, B. Keating (2006), ‘Observational constraints on Cosmic Reionization’.
- Fan Xiaohui, Joseph F. Hennawi, Gordon T. Richards, Michael A. Strauss, Donald P. Schneider, Jennifer L. Donley, Jason E. Young, James Annis, Huan Lin, Hubert Lampeitl, Robert H. Lupton, James E. Gunn, Gillan R. Knapp, W. N. Brandt, Scott Anderson, Neta A. Bahcall, Jon Brinkmann, Robert J. Brunner, Masataka Fukugita, Alexander S. Szalay, Gyula P. Szokoly, Donald G. York (2004), ‘A Survey of  $z > 5.7$  Quasars in the Sloan Digital Sky Survey III: Discovery of Five Additional Quasars’, *apj*.
- Fan Xiaohui, Vijay K. Narayanan, Robert H. Lupton, Michael A. Strauss, Gillian R. Knapp, Robert H. Becker, Richard L. White, Laura Pentericci, S. K. Leggett, Zoltán Haiman, James E. Gunn, Zeljko Ivezic, Donald P. Schneider, Scott F. Anderson, J. Brinkmann, Neta A. Bahcall, Andrew J. Connolly, Istvan Csabai, Mamoru Doi, Masataka Fukugita, Tom Geballe, Eva K. Grebel, Daniel Harbeck, Gregory Hennessy, Don Q. Lamb, Gajus Miknaitis, Jeffrey A. Munn, Robert Nichol, Sadanori Okamura, Jeffrey R. Pier, Francisco Prada, Gordon T. Richards, Alex Szalay, Donald G. York (2001), ‘A Survey of  $z > 5.8$  Quasars in the Sloan Digital Sky Survey I: Discovery of Three New Quasars and the Spatial Density of Luminous Quasars at  $z \sim 6$ ’, *apj*.
- Fan, Xiaohui; Wang, Feige; Yang, Jinyi; Keeton, Charles R.; Yue, Minghao; Zabludoff, Ann; Bian, Fuyan; Bonaglia, Marco; Georgiev, Iskren Y.; Hennawi, Joseph F.; Li, Jiangtao; McGreer, Ian D.; Naidu, Rohan; Pacucci, Fabio; Rabien, Sebastian; Thompson, David; Venemans, Bram; Walter, Fabian; Wang, Ran; Wu, Xue-Bing (2019), ‘The Discovery of a Gravitationally Lensed Quasar at  $z = 6.51$ ’, *apjl* **870**(2), 6.
- Fukugita, M.; Ichikawa, T.; Gunn, J. E.; Doi, M.; Shimasaku, K.; Schneider, D. P. (1996), ‘The Sloan Digital Sky Survey Photometric System ’, *apj* **111**, 1748.
- Gunn, J. E.; Carr, M.; Rockosi, C.; Sekiguchi, M.; Berry, K.; Elms, B.; de Haas, E.; Ivezić, Ž.; Knapp, G.; Lupton, R.; Pauls, G.; Simcoe, R.; Hirsch, R.; Sanford, D.; Wang, S.; York, D.; Harris, F.; Annis, J.; Bartozek, L.; Boroski, W. Bakken, J.; Haldeman, M.; Kent, S.; Holm, S.; Holmgren, D.; Petravick, D.; Prosapio, A.; Rechenmacher, R.; Doi, M.; Fukugita, M.; Shimasaku, K.; Okada, N.; Hull, C.; Siegmund, W.; Mannery, E.; Blouke, M.; Heidtman, D.; Schneider, D.; Lucinio, R.; Brinkman, J. (n.d.).

- Guo Hengxiao, Jiacheng Peng, Kaiwen Zhang, Colin J. Burke, Xin Liu, Mouyuan Sun, Shu Wang, Minzhi Kong, Zhenfeng Sheng, Tinggui Wang, Zhicheng He, and Minfeng Gu (n.d.).
- Hawkins, M. R. S. (2007), ‘Timescale of variation and the size of the accretion disc in active galactic nuclei’, *A&A* **462**, 581–589.
- Ho, L. C. (2008), ‘Nuclear Activity in Nearby Galaxies’.
- Hopkins Philip F., Hernquist Lars , Cox Thomas J. & Eres Dusan K. (2007), ‘A cosmological framework for the co-evolution of quasars, supermassive black holes and elliptical galaxies: I. galaxy mergers & quasar activity’, *apj* .
- Jiang Linhua , Ian D. McGreer, Xiaohui Fan, Michael A. Strauss, Eduardo Bañados, Robert H. Becker, Fuyan Bian, Kara Farnsworth, Yue Shen, Feige Wang, Ran Wang, Shu Wang, Richard L. White, Jin Wu, Xue-Bing Wu, Jinyi Yang and Qian Yang (2016), ‘The final SDSS high-redshift quasar sample of 52 quasars at  $z > 5.7$ ’.
- Kawaguchi T., Mineshige S., Umemura M., Turner Edwin L. (1998), ‘Optical variability in active galactic nuclei: starbursts or disk instabilities?’.
- Kelly Brandon C., Bechtold Jill, Siemiginowska Aneta (2009), ‘Are the variations in quasar optical flux driven by thermal fluctuations?’.
- Kimura Y., Toru Yamada, Mitsuro Kokubo, Naoki Yasuda, Tomoki Morokuma, Tohru Nagao, Yoshiki Matsuoka (2020), ‘Properties of AGN Multiband Optical Variability in the HSC SSP Transient Survey’, *apj* .
- Kinemuchi K., Patrick B. Hall, Ian McGreer, C. S. Kochanek, Catherine J. Grier, Jonathan Trump, Yue Shen, W. N. Brandt, W. M. Wood-Vasey, Xiaohui Fan, Bradley M. Peterson, Donald P. Schneider, Juan V. Hernández Santisteban, Keith Horne, Yuguang Chen, Sarah Eftekharzadeh, Yucheng Guo, Siyao Jia, Feng Li, Zefeng Li, Jundan Nie, Kara A. Ponder, Jesse Rogerson, Tianmen Zhang, Hu Zou, Linhua Jiang, Luis C. Ho, Jean-Paul Kneib, Patrick Petitjean, Nathalie Palanque-Delabrouille, and Christophe Yeche. (2020), ‘The Sloan Digital Sky Survey Reverberation Mapping Project: Photometric g and i Light Curves’.
- Kozłowski Szymon (2016), ‘Virial black hole mass estimates for 280000 agns from the sdss broad-band photometry and single epoch spectra’.
- Lang Dustin, David W. Hogg, Keir Mierle, Michael Blanton, Sam Roweis (2009), ‘Astrometry.net: Blind astrometric calibration of arbitrary astronomical image’.
- Laurenti M., Vagnetti F., Middei R. and Paolillo M. (2020), ‘Individual optical variability of Active Galactic Nuclei from the MEXSAS2 sample’, *mnras* **1-13**.

- Li Zefeng , Ian D. McGreer, Xue-Bing Wu<sup>1</sup>, Xiaohui Fan and Qian Yang (2018), ‘The Ensemble Photometric Variability of Over 105 Quasars in the Dark Energy Camera Legacy Survey and the Sloan Digital Sky Survey’, *apj* **861**(1).
- Luo Y., Yue Shen, Qian Yang (2019), ‘Characterization of Optical Light Curves of Extreme Variability Quasars Over a  $\approx 16$ -yr Baseline’, *mnras* (1-14).
- MacLeod C. L., K. Brooks, Ž. Ivezić, C. S. Kochanek, R. Gibson, A. Meisner, S. Kozłowski, B. Sesar (2011), ‘QUASAR SELECTION BASED ON PHOTOMETRIC VARIABILITY’, *apj* **728**(26), 17.
- MacLeod C. L., Ž. Ivezić, C. S. Kochanek, S. Kozłowski, B. Kelly, E. Bullock, A. Kimball, B. Sesar, D. Westman, K. Brooks, R. Gibson, A. C. Becker, and W. H. de Vries (2010), ‘Modeling the Time Variability of SDSS Stripe 82 Quasars as a Damped Random Walk’.
- MacLeod Chelsea L., Željko Ivezić, Branimir Sesar, Wim de Vries, Christopher S. Kochanek, Brandon C. Kelly, Andrew C. Becker, Robert H. Lupton, Patrick B. Hall, Gordon T. Richards, Scott F. Anderson, and Donald P. Schneider (2012), ‘A DESCRIPTION OF QUASAR VARIABILITY MEASURED USING REPEATED SDSS AND POSS IMAGING’, *apj* **753**(106), 21.
- Madau Piero, Francesco Haardt, and Massimo Dotti (2014), ‘A SUPER-CRITICAL GROWTH OF MASSIVE BLACK HOLES FROM STELLAR-MASS SEEDS’, *Astronomy Astrophysics Review manuscript* .
- Mazzucchelli C. , E. Bañados , R. Decarli, E. P. Farina, B. P. Venemans, F. Walter, and R. Overzier (2017), ‘NO OVERDENSITY OF LYMAN-ALPHA EMITTING GALAXIES AROUND A QUASAR AT  $z \sim 5.7$ ’, *apj* **834**(83), 13.
- Mazzucchelli C., Bañados E., Venemans B. P. , Decarli R. Farina E. P., Walter F., Eilers A.-C., Rix H.-W., Simcoe R., Stern D., Fan X., Schlafly E., De Rosa G., Hennawi J., Chambers K. C., Greiner J., Burgett W., Draper P.W., Kaiser N., Kudritzki R.-P., Magnier E., Metcalfe N., Waters C., Wainscoat R. J. (2017), ‘PHYSICAL PROPERTIES OF 15 QUASARS AT  $Z > 6.5$ ’.
- Mazzucchelli Chiara (2018), The Physical Properties and Cosmic Environments of Quasars in the First Gyr of the Universe, PhD thesis.
- Meiksin, A. (2005), ‘Colour corrections for high redshift objects due to intergalactic attenuation’.
- Montesinos-Armijo M. A. and de Freitas Pacheco J. A. (2011), ‘The growth of super-massive black holes fed by accretion disks’, *Astronomy&Astrophysics* **526**(A146).

- Morganson E., W. S. Burgett, K. C. Chambers, P. J. Green, N. Kaiser, E. A. Magnier, P. J. Marshall, J. S. Morgan, P. A. Price, H.-W. Rix, E. F. Schlafly, J. L. Tonry, and F. Walter (2014), ‘MEASURING QUASAR VARIABILITY WITH Pan-STARRS1 AND SDSS’, *apj* **784**(92), 16.
- Morganson Eric, De Rosa Gisella, Walter Fabian, Chambers Ken, Mcgreer Ian, Fan Xiaohui, Burgett William, Flewelling Heather, Hodapp Klaus, Kaiser Nick, Magnier Eugene, Price Paul, Rix Hans-Walter, Sweeney Bill, Waters Christopher (2011), ‘THE FIRST HIGH REDSHIFT QUASAR FROM PAN-STARRS’, *NONLEARNED J.* .
- Nanni, R. (2019), UNDERSTANDING THE FORMATION OF THE FIRST BLACK HOLES: DEEP OBSERVATIONS OF THE MOST DISTANT QUASARS, PhD thesis.
- Nanni Riccardo, C. Vignali, R. Gilli, A. Moretti, and W. N. Brandt (2017), ‘The X-ray properties of  $z \approx 6$  luminous quasars’, *Astronomy & Astrophysics manuscript* .
- Nanni Riccardo, R. Gilli, C. Vignali, M. Mignoli, A. Comastri, E. Vanzella, G. Zamorani, F. Calura, G. Lanzuisi, M. Brusa P. Tozzi , K. Iwasawa, M. Cappi, F. Vito, B. Balmaverde , T. Costa , G. Risaliti, M. Paolillo, I. Prandoni, E. Liuzzo, P. Rosati, M. Chiaberge,, G. B. Caminha, E. Sani, N. Cappelluti, and C. Norman (2018), ‘The 500 ks Chandra observation of the  $z = 6.31$  QSO SDSS J1030+0524’, *Astronomy & Astrophysics manuscript* .
- Padovani, P, Alexander D. M., Assef R., De Marco J, Giommi P, Hickox R. C., Richards G. T., Smolcic V., Hatziminaoglou E., Mainieri V, Salvato M. (2017), ‘Active Galactic Nuclei: what’s in a name?’, *Astronomy Astrophysics Review manuscript* .
- Pezzulli Edwige ,Volonteri Marta, Schneider Raffaella, Valiante Rosa (2017), ‘The sustainable growth of the first black holes’, *MNRAS* *000* p. 1–7.
- Ruan J.J. , Scott F. Anderson, Jason Dexter, Eric Agol (2018), ‘EVIDENCE FOR LARGE TEMPERATURE FLUCTUATIONS IN QUASAR ACCRETION DISKS FROM SPECTRAL VARIABILITY’.
- Ruan J.J., Scott F. Anderson, Sabrina L. Cales, Michael Eracleous, Paul J. Green, Eric Morganson, Jessie C. Runnoe, Yue Shen, Tessa D. Wilkinson, Michael R. Blanton, Tom Dwelly, Antonis Georgakakis, Jenny E. Greene, Stephanie M. LaMassa, Andrea Merloni, and Donald P. Schneider (2016), ‘TOWARD AN UNDERSTANDING OF CHANGING-LOOK QUASARS: AN ARCHIVAL SPECTROSCOPIC SEARCH IN SDSS’, *apj* **826**(188), 15.
- Rumbaugh N., Yue Shen, Eric Morganson, Xin Liu, M. Banerji, R. G. McMahon, F. B. Abdalla, A. Benoit-Lévy, E. Bertin, D. Brooks, E. Buckley-Geer, D. Capozzi, A. Carnero Rosell, M. Carrasco Kind, J. Carretero, C. E. Cunha, C. B. D’Andrea, L. N.

- da Costa, D. L. DePoy, S. Desai, P. Doel, J. Frieman, J. García-Bellido, D. Gruen, R. A. Gruendl, J. Gschwend, G. Gutierrez, K. Honscheid, D. J. James, K. Kuehn, S. Kuhlmann, N. Kuropatkin, M. Lima, M. A. G. Maia, J. L. Marshall, P. Martini, F. Menanteau, A. A. Plazas, K. Reil, A. Roodman, E. Sanchez, V. Scarpine, R. Schindler, M. Schubnell, E. Sheldon, M. Smith, M. Soares-Santos, F. Sobreira, E. Suchyta, M. E. C. Swanson, A. R. Walker, and W. Wester (2010), ‘Extreme Variability Quasars from the Sloan Digital Sky Survey and the Dark Energy Survey’, *apj* **854**(160), 14.
- Schmidt Kasper B., Philip J. Marshall, Hans-Walter Rix, Sebastian Jester, Joseph F. Hennawi and Gregory Dobler (2010), ‘SELECTING QUASARS BY THEIR INTRINSIC VARIABILITY’, *apj* **714**, 1194–1208.
- Scolnic D., S. Casertano, A. G. Riess, A. Rest, E. Schlafly, R. J. Foley, D. Finkbeiner, C. Tang, W. S. Burgett, K. C. Chambers, P. W. Draper, H. Flewelling, K. W. Hodapp, M. E. Huber, N. Kaiser, R. P. Kudritzki, E. A. Magnier, N. Metcalfe, C. W. Stubbs (2015), ‘Supercal: Cross-Calibration of Multiple Photometric Systems to Improve Cosmological Measurements with Type Ia Supernovae’.
- Sesana, A. (2011), ‘A practical guide to the massive black hole cosmic history’, *Astronomy Astrophysics Review manuscript*.
- Sesar Branimir, Zeljko Ivezic, Robert H. Lupton, Mario Juric, James E. Gunn, Gillian R. Knapp, Nathan De Lee, J. Allyn Smith, Gajus Miknaitis, Huan Lin, Douglas Tucker, Mamoru Doi, Masayuki Tanaka, Masataka Fukugita, Jon Holtzman, Steve Kent, Brian Yanny, David Schlegel, Douglas Finkbeiner, Nikhil Padmanabhan, Constance M. Rockosi, Nicholas Bond, Brian Lee, Chris Stoughton, Sebastian Jester, Hugh Harris, Paul Harding, Jon Brinkmann, Donald P. Schneider, Donald York, Michael W. Richmond, and Daniel Vanden Berk (2007), ‘Exploring the variable sky with the Sloan Digital Sky Survey’, *apj* **134**.
- Shen Yue, Gordon T. Richards, Michael A. Strauss, Patrick B. Hall, Donald P. Schneider, Stephanie Snedden, Dmitry Bizyaev, Howard Brewington, Viktor Malanushenko, Elena Malanushenko, Dan Oravetz, Kaike Pan, and Audrey Simmons (2011), ‘A catalog of quasar properties from Sloan Digital Sky Survey data release 7’, *apj supplement series* **194**(45), 21.
- Sheng Zhenfeng , Tinggui Wang, Ning Jiang, Chenwei Yang, Lin Yan, Liming Dou and Bo Peng (2017), ‘Mid-infrared Variability of Changing-look AGNs’, *apj* **846**, 7.
- Stubbs Christopher W., Peter Doherty, Claire Cramer, Gautham Narayan, Yorke J. Brown, Keith R. Lykke, John T. Woodward, and John L. Tonry (2010), ‘PRECISE THROUGHPUT DETERMINATION OF THE PanSTARRS TELESCOPE AND

- THE GIGAPIXEL IMAGER USING A CALIBRATED SILICON PHOTODIODE AND A TUNABLE LASER: INITIAL RESULTS', *apj* **191**(2).
- Tonry, J. L.; Stubbs, C. W.; Lykke, K. R.; Doherty, P.; Shivvers, I. S.; Burgett, W. S.; Chambers, K. C.; Hodapp, K. W.; Kaiser, N.; Kudritzki, R. -P.; Magnier, E. A.; Morgan, J. S.; Price, P. A.; Wainscoat, R. J. (2012), 'The Pan-STARRS1 Photometric System'.
- Trèvese Dario and Vagnetti Fausto (2002), 'Quasar Spectral Slope Variability in the Optical Band', *apj*.
- Ulrich Marianne Helene, Maraschi Laura, Urry C. Megan (1997), 'VARIABILITY OF ACTIVE GALACTIC NUCLEI', *ARAA* **35**, 445–502.
- Urry, C. M. & Padovani, P. (1995), 'Unified Schemes for Radio-Loud Active Galactic Nuclei', *pasp* (107), 803.
- Vanden Berk Daniel E., Brian C. Wilhite, Richard G. Kron, Scott F. Anderson, Robert J. Brunner, Patrick B. Hall, Željko Ivezić, Gordon T. Richards, Donald P. Schneider, Donald G. York, Jonathan V. Brinkmann, Don Q. Lamb, Robert C. Nichol, David J. Schlegel (2003), 'The Ensemble Photometric Variability of  $\approx 25000$  Quasars in the Sloan Digital Sky Survey'.
- Venemans B. P. , E. Bañados, R. Decarli, E. P. Farina, F. Walter, K. C. Chambers, X. Fan, H-W. Rix, E. Schlafly, R. G. McMahon, R. Simcoe, D. Stern, W. S. Burgett, P. W. Draper, H. Flewelling, K. W. Hodapp, N. Kaiser, E. A. Magnier, N. Metcalfe, J. S. Morgan, P. A. Price, J. L. Tonry, C. Waters, Y. AlSayyad, M. Banerji, S. S. Chen, E. A. González-Solares, J. Greiner, C. Mazzucchelli, I. McGreer, D. R. Miller, S. Reed, P. W. Sullivan (n.d.), 'The identification of z-dropouts in Pan-STARRS1: three quasars at  $6.5 < z < 6.7$ ', *apj*.
- Volonteri, M. (2017), 'The Formation and Evolution of Massive Black Holes'.
- Volonteri Marta & Rees Martin J. (2006), 'QUASARS AT Z=6: THE SURVIVAL OF THE FITTEST'.
- Volonteri Marta, Haardt Francesco and Madau Piero (2003), 'THE ASSEMBLY AND MERGING HISTORY OF SUPERMASSIVE BLACK HOLES IN HIERARCHICAL MODELS OF GALAXY FORMATION', *apj* **582**, 559–573.
- Volonteri Marta, Silk Joseph & Guillaume Dubus (2018), 'THE CASE FOR SUPERCRITICAL ACCRETION ONTO MASSIVE BLACK HOLES AT HIGH RED-SHIFT'.

- Wang Feige, Xiaohui Fan, Jinyi Yang, Chiara Mazzucchelli, Xue-Bing Wu, Jiang-Tao Li, Eduardo Bañados, Emanuele Paolo Farina, Riccardo Nanni, Yanli Ai, Fuyan Bian, Frederick B. Davies, Roberto Decarli, Joseph F. Hennawi, Jan-Torge Schindler, Bram Venemans and Fabian Walter (2020), ‘Revealing the Accretion Physics of Supermassive Black Holes at Redshift  $z \sim 7$  with Chandra and Infrared Observations’.
- Willhite Brian C., Robert J. Brunner, Catherine J. Grier, Donald P. Schneider and Daniel E. Vanden Berk (2008), ‘On the variability of quasars: a link between the Eddington ratio and optical variability?’, *mnras* **383**, 1232–1240.
- Xiaohui Fan, Michael A. Strauss, Donald P. Schneider, James E. Gunn, Robert H. Lupton, Brian Yanny, Scott F. Anderson, John E. Anderson, Jr., James Annis, Neta A. Bahcall, J. A. Bakken, Steven Bastian, Eileen Berman, William N. Boroski, Charlie Briegel, John W. Briggs, J. Brinkmann, Michael A. Carr, Patrick L. Colestock, A. J. Connolly, J. H. Crocker, István Csabai, Paul C. Czarapata, John Eric Davis, Mamoru Doi, Brian R. Elms, Michael L. Evans, Glenn R. Federwitz, Joshua A. Frieman, Masataka Fukugita, Vijay K. Gurbani, Frederick H. Harris, Timothy M. Heckman, G. S. Hennessy, Robert B. Hindsley, Donald J. Holmgren, Charles Hull, Shin-Ichi Ichikawa, Takashi Ichikawa, Željko Ivezić, Stephen Kent, G. R. Knapp, Richard G. Kron, D.Q. Lamb, R. French Leger, Siriluk Limmongkol, Carl Lindenmeyer, Daniel C. Long, Jon Loveday, Bryan MacKinnon, Edward J. Mannery, P. M. Mantsch, Bruce Margon, Timothy A. McKay, Jeffrey A. Munn, Thomas Nash, Heidi Jo Newberg, R. C. Nichol, Tom Nicinski, Sadanori Okamura, Jeremiah P. Ostriker, Russell Owen, A. George Pauls, John Peoples, Donald Petravick, Jeffrey R. Pier, Ruth Pordes, Angela Prosapio, Ron Rechenmacher, Gordon T. Richards, Michael W. Richmond, Claudio H. Rivetta, Constance M. Rockosi, Dale Sandford, Gary Sergey, Maki Sekiguchi, Kazuhiro Shimasaku, Walter A. Siegmund, J. Allyn Smith, Chris Stoughton, Alexander S. Szalay, Gyula P. Szokoly, Douglas L. Tucker, Michael S. Vogeley, Patrick Waddell, Shu-i Wang, David H. Weinberg, Naoki Yasuda and Donald G. York (1999), ‘High-redshift quasars found in Sloan Digital Sky Survey commissioning data’, *apj*.
- Xiaohui Fan, Michael A. Strauss, James E. Gunn, Robert H. Lupton, C. L. Carilli, M. P. Rupen, Gary D. Schmidt, Leonidas A. Moustakas, Marc Davis, James Annis, Neta A. Bahcall, J. Brinkmann, Robert J. Brunner, István Csabai, Mamoru Doi Masataka Fukugita, Timothy M. Heckman, G. S. Hennessy, Robert B. Hindsley, Željko Ivezić, G. R. Knapp, D. Q. Lamb, Jeffrey A. Munn, A. George Pauls, Jeffrey R. Pier, Constance M. Rockosi, Donald P. Schneider, Alexander S. Szalay, Douglas L. Tucker, Donald G. York (1999), ‘The Discovery of a High-redshift Quasar without Emission Lines from Sloan Digital Sky Survey Commissioning Data’.
- Xin Chengcheng, Maria Charisi, Zoltán Haiman, David Schiminovich (2019), ‘Correlation between Optical and UV Variability of Quasars’, *mnras* (1–11).

- Yang Jinyi, Feige Wang, Xiaohui Fan, Minghao Yue, Xue-Bing Wu, Jiang-Tao Li, Fuyan Bian, Linhua Jiang, Eduardo Bañados and Yuri Beletsky (2018), ‘Exploring Reionization-Era Quasars IV: Discovery of Six New  $z \sim 6.5$  Quasars with DES, VHS and unWISE Photometry’.
- Yang Q., Xue-Bing Wu, Xiaohui Fan, Linhua Jiang, Ian McGreer, Jinyi Shangguan, Bingquan Wang, Ravi Joshi, Richard Green, Feige Wang, Xiaotong Feng, Yuming Fu, Jinyi Yang, and Yuanqi Liu, Su Yao (2018), ‘Discovery of 21 New Changing-look AGNs in the Northern Sky’, *apj* **862**(109), 19.



# Ringraziamenti

Era la seconda metà di febbraio quando mi trovavo a Loiano a svolgere le osservazioni. Nel frattempo, a Codogno veniva dichiarato il primo caso di Covid-19 in Italia. Sappiamo tutti come è andata dopo. Ringrazio questa pandemia mondiale per tutti gli ostacoli imprevisti.

A tutti gli altri:

*Conosco la metà di voi solo a metà e nutro per meno della metà di voi metà dell'affetto che meritate.*

*Per aspera ad astra.*